

ABSTRACT

Title of thesis: INVERSE SPECTRAL METHODS IN ACOUSTIC NORMAL MODE VELOCIMETRY OF HIGH REYNOLDS NUMBER SPHERICAL COUETTE FLOWS.

Anthony Mautino, Master of Science, 2016

Thesis directed by: Professor Vedran Lekic
Department of Geology

Experimental geophysical fluid dynamics often examines regimes of fluid flow infeasible for computer simulations. Velocimetry of zonal flows present in these regimes brings many challenges when the fluid is opaque and vigorously rotating; spherical Couette flows with molten metals are one such example. The fine structure of the acoustic spectrum can be related to the fluid's velocity field, and inverse spectral methods can be used to predict and, with sufficient acoustic data, mathematically reconstruct the velocity field. The methods are to some extent inherited from helioseismology. This work develops a Finite Element Method suitable to matching the geometries of experimental setups, as well as modelling the acoustics based on that geometry and zonal flows therein. As an application, this work uses the 60-cm setup Dynamo 3.5 at the University of Maryland Nonlinear Dynamics Laboratory. Additionally, results obtained using a small acoustic data set from recent experiments in air are provided.

INVERSE SPECTRAL METHODS IN ACOUSTIC NORMAL MODE
VELOCIMETRY OF HIGH REYNOLDS NUMBER SPHERICAL COUETTE
FLOWS

by

Anthony Robert Mautino

Thesis submitted to the Faculty of the Graduate School of the
University of Maryland, College Park in partial fulfillment
of the requirements for the degree of
Master of Science
2016

Advisory Committee:
Professor Vedran Lekic, Chair/Advisor
Professor Daniel Lathrop, Co-Advisor
Professor William McDonough

© Copyright by
Anthony Robert Mautino
2016

Acknowledgments

First and foremost, with regard to this thesis, I would thank my advisor Ved Lekic. Ved was always available, usually on a daily basis, to work with me. He was of considerable guidance and help in both the research that went into this work as well as the drafting of this thesis. I thank Ved greatly for both my research assistantships as well as arranging my teaching assistantships.

I would also like to thank the rest of my committee. Dan Lathrop has served as a co-advisor throughout this thesis and offered much input. Bill McDonough has always made himself available for discussing science both related and unrelated to this endeavor, as well as encouraging me to have a more positive outlook in science.

I thank everyone else on the faculty who took time to discuss science and teach me things while I was here, especially Phil Candela. I thank all the fellow students who gave me engaging discussions, especially my fellow lab member Chao Gao.

I thank Todd Karwoski for all the IT support, and Michelle Montero for all her assistance with the formalities of being a graduate student.

And of course, I thank my Mother for all her support.

Table of Contents

List of Tables	v
List of Figures	vii
List of Abbreviations	x
1 Background	1
1.1 Laboratory Analogs of Flows in the Earth’s Core	1
1.1.1 Laboratory Simulations vs. Computer Simulations	1
1.1.2 Spherical Couette Flows	4
1.2 Parameters for Spherical Couette Flows	5
1.2.1 Reynolds Number	5
1.2.2 Ekman Number	8
1.2.3 Rossby Number	9
1.2.4 ω Effect	10
1.3 Velocimetry of Fluid Flows	11
1.3.1 Challenges of Traditional Techniques of Velocimetry	11
1.3.2 Acoustic Normal Mode Inverse Spectral Methods	12
1.4 60-cm Setup	18
1.4.1 Laboratory Configuration	18
1.4.2 Modeling the Geometry	22
2 Previous Work in the Field	24
2.1 Analysis and Discussion	24
2.2 Contrast with this Work	40
3 Mathematical Formulation	43
3.1 Acoustic Pressure Perturbation in Stationary Homogeneous Media	43
3.2 Exploiting Axisymmetric Geometry for Computational Efficiency	44
3.3 Variational Form of the Acoustic Helmholtz PDE in Pressure	45
3.4 Discussion of Variational Scalar Formulation	45
3.5 Modal Nomenclature	46
4 Numerical Formulation	51
4.1 Finite Element Formulation	51
4.2 Solving for the Stationary Modes and Stationary Frequencies	53
4.3 Discussion of FEM Predictions for Stationary Modes	57
4.4 Solution for a Spherical Annulus	57
4.4.1 Modes of the Spherical Annulus	57
4.4.2 Computing the Solution to the Radial Wave Equation	58
4.5 Comparing Theory and FEM for Spherical Annulus Solution	60

5	Linear Theory of Acoustic Splitting for Rotating Flows with Shear	63
5.1	Wave Equation inside a Vortex	63
5.2	Uniform Rotation	67
5.3	Soundspeed Uniformity	69
6	Relating Fluid Rotation to Acoustics	71
6.1	Flow Characteristics	71
6.2	Parametrization Style for the Flow	71
6.3	The Forward Operator	73
6.4	Boundary Conditions of the Fluid Flow	74
7	Techniques of Inversion	75
7.1	Constrained Optimization	75
7.2	Minimizing Spread Functions	79
7.2.1	Basic Principle	79
7.2.2	Dirichlet Spread Function Minimization	81
7.2.3	Backus and Gilbert Spread Function Minimization	81
7.3	Adaptive Parametrizations	83
7.3.1	Adaptive Interpolation	83
7.3.2	Non-coefficient Model Parameters	85
8	Applications to Ambient Noise Data	87
8.1	Data Processing	87
8.1.1	Array Configuration	87
8.2	Parametrization	101
8.2.1	Approach to Parametrizing Fluid Rotation	101
8.2.2	Cylindrically Radial Cubic B-Splines and Neumann Modes	103
8.2.3	Choice of Reference Frame	105
8.3	Processed Data	105
8.4	Inversions for Rotation	109
8.4.1	Constrained Optimization Inversions	109
8.4.2	Consistency with Alternate Basis Functions	125
8.5	Alternate Methods of Inversions	129
8.5.1	Minimization of Spread Functions	129
8.5.2	Interpolating on a Fixed Grid	132
8.6	Mean Flow Approximation Issues	133
8.7	Alternate Basis Discussion	134
9	Concluding Discussion	136
9.1	Conclusions	136
9.1.1	Application of the Finite Element Methods	136
9.1.2	Bulk Fluid Rotation Recovery	136
9.2	Looking Forward	137
9.2.1	Liquid Sodium Experiments	137
9.2.2	Poloidal Flow	137
9.3	Recommendations for Future Improvements	138
9.3.1	Inversion Formulation	138
9.3.2	Poloidal Flow	139
9.3.3	Modeling Geometry	139
9.3.4	Meshing Geometry	140
9.3.5	Test Functions and Shape Functions	140
9.3.6	Inclusion of Magnetic Data in Constraints	141
9.3.7	Adaptive Interpolation	141
	Bibliography	142

List of Tables

4.1	FEM calculated frequencies at $c=344$ m/s for the 60-cm setup. As can be seen, the multiplets are split due to the shaft's presence. Values have been rounded to the nearest natural number. The data the methods are applied to is as high as 2.1kHz; the reason for the range presented.	56
4.2	Normal Mode Frequencies computed by FEM in column 3 agrees quite well with the theoretical semi-numerical result in column 2, as seen in the relative errors in column 4. The differences between frequencies of the elements in the multiplets are quite small as well; column 5. The NA values are reflecting that only $m_s = 0$ is possible when $l = 0$. Note: the estimated relative errors are based on the unrounded values.	61
5.1	A comparison of my FEM predictions with observed frequencies in the stationary medium by targeted chirp, and errors are a small fraction of 1%. The error is likely even slightly lower, since the soundspeed was calibrated using the lowest frequency, rather than the highest, or some least squares fit to all. The measured acoustic data in the column for observed frequency were performed by Matthew Adams.	67
5.2	Comparison of the same mode set from the table 5.1 , at various rotation rates where the inner and outer boundaries are spinning together, spun up to achieve uniform rotation of the fluid. The Δ values are the absolute shift of the modes from the center frequency in Hz. The denominators on the observation Δ values are the rate of medium's rotation in Hz. The leftmost column represents the expected shift from center frequency due to 1 Hz uniform fluid rotation. The percent errors do not take any account of the observational uncertainties or modeling uncertainties. The missing data in the first row is because measurement could not be reliably made due to that portion of the spectrum at the high rotation rate of the experiment being very noisy. Under the presumption that there should be no splitting at 0 Hz then, the linearity implies that the ratio of the splitting to rotation rate should remain invariant during experiments and equal to the finite element prediction. Note: This table does not give signs to the shifts, since signs were not measured for the data, only the magnitude of the splitting was measured. Acoustic data measurements made by Matthew Adams.	68
8.1	Mode wavenumbers and stationary frequency prediction at $c=344$ m/s. These are the modes used to perform the inversions. Additionally, the frequency shift from center frequency due to uniform rotation with the outer shell at 6Hz has been provided, rounded to 1 decimal place, since it does not appear in the presented splitting data, it has been subtracted off. The negative sign indicated that $- m_s $ has a higher frequency than $+ m_s $. Values rounded to nearest tenth of a Hz. The splitting is thus approximately twice these listed values. The first column provides the index used in plots of data fits in this chapter, for reference. They are always presented in this order herein.	89

8.2	Frequency shift from center frequency in Hz. Top row is F_i in Hz, and each row is a mode pair given by the first column. Measurements are in Hz. Outer Sphere is rotating at 6 Hz and the inner sphere rotation in Hz is given at the top of each column. Each row is for one particular mode. The data has had the correction due to being in a rotating frame removed from it. For instance, the first row shows (0,1,1) has relatively small shifts, but its shift due to the Coriolis effect of being in a rotating frame is almost 4 Hz. The value stated is the residual after that amount was subtracted off. Refer to table 8.1 for the approximate Coriolis correction of the rotating frame that has been removed.	106
8.3	Errors (Hz) relative to the mean that are used for performing inversions. Table layout presented in the same form as table 8.2. Values are rounded off to nearest tenth in the table.	107
8.4	Fraction of measurement that the error radius represents, as a percent. Often the uncertainty is small relative to the absolute shift that includes the shift induced by the rotating frame, but much larger relative to the residual shift. Table layout same as in table 8.2.	108

List of Figures

1.1	Schematic of the 60-cm setup and configuration in the lab. Diameter of the outer sphere is approximately 60 cm and of the inner sphere is a approximately 20 cm. Diagram courtesy of Matthew Adams.	20
1.2	Interior of the 60cm Setup taken apart showing electronics mounted inside, before assembly. The setup tries to minimize the invasiveness of the electronics. The axis of rotation, embodied by the physical axle, is vertical during operation. Photographs courtesy of Matthew Adams.	21
1.3	Meridional cross section of the geometry, showing the proportions used to model the cross section. The z-axis is the axis of rotation where the axle and shaft are.	23
2.1	Reproduction of a figure from Triana et al. [2014], showing anemometer profile and level of consistency with inversion profiles, as well as posterior uncertainty estimates. s is cylindrical radius, r_o is the outer sphere radius.	30
2.2	Reproduction of a figure from Triana et al. [2014], averaging kernels for several locations used in the inversion. The white cross hairs are showing the location in the domain, which has been broken into thousands of small tiles as basis functions, and the colors are showing the averaging kernel for it. Note the high non-local diffusion, especially for the bottom left sub-figure. The reconstructed rotation rate at the point marked, will be a weighted average of the rotation rates at other locations in the domain, and the weights are given by the coloring of the domain.	33
3.1	Meridional cross section of pressure modes (1,0,0) and (2,0,0). The color represents the relative amplitude. The nodal curves in white.	47
3.2	Meridional cross section of pressure modes (0,1,0) and (0,2,0). The color represents the relative amplitude. The nodal curves in white.	49
3.3	Meridional cross section of pressure mode (1,3,2). The color represents the relative amplitude. The nodal curves in white. Since $m=2$ is known from how the PDE is solved, the nodal curves can be counted. See that $n=1$, and $l - m_s = 1$, and so $l = 3$. No inconsistencies or ambiguities result from adopting this naming convention in the altered geometry within the frequency range and small wavenumbers used in this study.	50
8.1	Comparison of acoustic spectrum with different frequency resolutions. The black curve has been created with a frequency resolution of 0.3 Hz whereas the red curve has a frequency resolution of 0.05 Hz. Note: magnitudes are linear, not in decibels. The clusters of peaks could be due to poloidal flow, noise envelopes, mechanical noise, changing mean flow state during time integration, or some combination thereof.	91

8.2	Power spectra plot of acoustic frequency(horizontal axis) vs. inner core rotation rate (vertical axis) near the modes (0,1,1) and (0,1,-1). Color is relative amplitude in log scale. The spectra is computed by taking the difference at two microphones at equal latitude spaced apart by 180 degrees in terms of azimuth. This shows drift as the temperature increases inducing center frequency shift, and shows that the dominant effect on splitting is the outer spinning at 6 Hz rather than the greater splitting that occurs due to additional rotation of the inner core. There could also be some effect of poloidal flow. In this regime centrifugal force is not expected to have any significant effects.	95
8.3	Similar figure and axes as in figure 8.2. Power spectra plot of power spectral density vs. inner core rotation rate near the mode(0,1,0). This shows drift as the temperature increases inducing center frequency shift. Color is relative amplitude in log scale. The spectra is computed by taking the sum of two microphones at equal latitude spaced apart by 180 degrees in terms of azimuth.	96
8.4	Power spectra plot of frequency vs. inner core rotation rate near the mode (2,3,1). Intensity of the plot is power spectral density, relative amplitude in log-scale. Note splitting changes with rotation rate, and also the drift of the center frequency. . . .	97
8.5	Power spectra plot (difference between microphones) of power spectral density vs. inner core rotation rate near the modes (0,2,1) and (0,2,-1). This shows drift as the temperature increases inducing center frequency shift, and shows that the dominant effect on splitting is the outer spinning at 6 Hz rather than the greater splitting that occurs due to additional rotation of the inner core. The lower plot is a power spectral density estimate placed on a linear scale, for inner core rotation rate of -40 Hz. It is a relative amplitude, not calibrated to any particular loudness level. . . .	99
8.6	RMS misfit of the ratio of the discrepancy between predicted frequencies from inversions and the measured values of frequencies to the error weights. The rotation rate of the outer sphere was 6 Hz, and the inner sphere's rotation rates were -4,-6,...,-40 Hz and shown in the horizontal axis. For the purposes of assessing overfitting vs. underfitting the data, the vertical axis values should be scaled by a factor of between 2 and 4 for converting to uncertainty on the mean. Any choice of a particular value for scaling would be somewhat arbitrary.	109
8.7	Histogram with Gaussian fit for an ensemble of 5000 inversions for $Ro=-4.67$, for the angular momentum quantity described in figure 8.8. The distribution was sufficiently Gaussian and similar in standard deviation and mean for smaller ensembles that it allowed for sufficient accuracy in the weighting of the data when performing fits.	111
8.8	The azimuthal angular momentum as a percent of the uniform rotation case at 6Hz, depicted by triangles. The variation with respect to sampling the data within the uncertainty interval around presented as error bars, and the curve depicting a purely quadratic relationship with Rossby number after offsetting by 100% at uniform rotation, i.e. $Ro=0$. The coefficient in the quadratic term is ≈ -0.62	112
8.9	The fit of $\%V_6$ is a second order polynomial in Ro with an intercept of 100% at $Ro=0$	114
8.10	The fit of $\%\Omega_6$ is linear but does not go through the 100% at $Ro=0$	115
8.11	Inferred ω_{effect} , described in chapter 1, as a function of Ro	116
8.12	Estimating the location of high shear. The horizontal axis represents the location of the vertical line separating the two piecewise constant basis functions, as inferred by minimizing the misfit to the acoustic data; described in text. Though a line is also possible to fit the data nearly as well, the square root function looked like a better fit and also goes through zero, which is consistent with solid body rotation of the fluid. The vertical axis has been non-dimensionalized by dividing by the radius of the outer sphere.	118
8.13	Data misfit for the shear zone parametrization by a sigmoid, using similar layout as figure 8.6. This corresponds to the data plotted in figure 8.13.	118

8.14	Reconstructed inversions at each rotation rate. The rotation rate of the inner sphere has been placed on top of each profile, but all other labelling has been omitted to reduce clutter. The outer sphere is spinning at 6 Hz.	120
8.15	Reconstructed flow profile for $Ro=-4.67$, i.e. $F_i = -22$ Hz and $F_o = 6$ Hz. There appears to be a jet forming on the equator of the inner sphere.	121
8.16	Data prediction from reconstructed flow profile for $Ro = -4.67$, i.e. $F_i = -22$ Hz and $F_o = 6$ Hz. The data is plotted in red with the error weights used in the inversion.	122
8.17	Relative variability profile for $Ro=-4.67$, i.e. $F_i = -22$ Hz and $F_o = 6$ Hz. The units of Hz is consistent with the mean flow error radius. This is only variation across an ensemble though, not necessarily reflective of the uncertainties related to how well the basis can match the flow in very localized regions.	123
8.18	Reconstructed flow profile for $Ro=-4.33$, i.e. $F_i = -20$ Hz and $F_o = 6$ Hz. Any jet is less pronounced in this inversion than in the one for $F_i = -22$ Hz.	124
8.19	Reconstructed Profiles using only 4 cubic splines, as discussed in text. Recovered profiles look similar to how the profiles in figure 8.14 would look if they were averaged vertically and homogenized in the z variable based on that average. Figure similar labelling convention as figure 8.14.	127
8.20	Data misfit analysis for basis consisting of 4 cubic splines, discussed in text. Figure similar to figure 8.6.	128
8.21	Result of minimizing Dirichlet spread function for 2D cubic spline basis. It has many realistic features, but also has some overshoot in the sense that it super-rotates the outer shell in a way that does not seem plausible.	130

List of Abbreviations

R	spherical radius variable
R_o	spherical radius of outer shell
R_i	spherical radius of inner core
r	cylindrical radius from axis of rotation
z	vertical signed distance from the equatorial plane
ϕ	azimuthal angle
θ	polar angle, usually colatitude
ρ_o	density
c	speed of sound
P	fluid pressure
p	acoustic pressure perturbation
ψ	pressure perturbation at zero azimuth
v	fluid velocity field
u	acoustic material displacement perturbation
ω	acoustic angular frequency
f	acoustic frequency in Hz
$\delta\omega$	perturbation in angular frequency
Ω	fluid angular velocity
Ω	fluid rotation rate in Hz
Ω_i	inner sphere angular velocity
Ω_o	outer sphere angular velocity
F_i	inner sphere rotation rate in Hz
F_o	outer sphere rotation rate in Hz
k	radial wavenumber
n	overtone number
l	polar degree
m_s	azimuthal order
Re	Reynolds' Number
Rm	Magnetic Reynolds' Number
Ro	Rossby Number
E_k	Ekman Number
ω	omega effect
C	forward operator
d	data vector
m	model vector
R_m	model resolution matrix
\mathcal{F}	Fourier transform operator
BFM	Barrier Function Method
FEM	Finite Element Method
FDM	Finite Difference Method
FWHM	Full Width at Half Max
MHD	Magnetohydrodynamics
NSE	Navier-Stokes Equations
OLA	Optimally Localized Averages
PDE	Partial Differential Equation
RMS	Root Mean Square
SCF	Spherical Couette Flow

Chapter 1: Background

1.1 Laboratory Analogs of Flows in the Earth's Core

1.1.1 Laboratory Simulations vs. Computer Simulations

Experimental Fluid Dynamics provides simulations inaccessible or unmanageable on the computers currently available; synthesizing flows with high Reynolds numbers and high magnetic Reynolds numbers appropriate to test theories of the Earth's core is not feasible [Lathrop and Forest, 2011]. For instance, numerical simulations of flows in the Earth's core use unrealistically high viscosity for the actual regimes they are modeling in order to maintain numerical stability [Dormy et al., 2000]. Early numerical models such as the canonical Glatzmaier and Roberts [1995] model were able to recover the Earth's dominant magnetic axial dipole, similar power spectra we observe on Earth, and other observed phenomena [Glatzmaier et al., 2004] while simulating flows lacking the turbulence thought to be present in the Earth's outer core. As the numerical models improved with computing power and more of parameter space was explored computationally, parameter values closer to that of Earth were used. The magnetic fields they produced in the simulations were not more "Earth-like", but were actually less "Earth-like" [Christensen et al., 2010]; lowering the viscosity relative to the Earth's modeled rotation rate and size more closely to the Earth's theorized ratios, made the magnetic fields overly dominated by the axial dipole not dipole dominated at all.

The ratio of kinematic viscosity to Coriolis forces is termed the Ekman number E_k , and is discussed herein. It is thought to be possibly as low as $E_k = 10^{-15}$ for the Earth's outer core, yet computer simulations typically employ values at least 8 orders of magnitude larger, and the "Earth-like" behavior occurring at 10 orders of magnitude higher near $E_k = 10^{-4}$ [Christensen

et al., 2010]. Though the kinematic viscosity in the outer core is one parameter that is not known very accurately, or at least not widely agreed upon [Secco, 1995], most estimates yield an Ekman number much smaller by many orders of magnitude than is used in numerical simulations that produce Earth-like magnetic fields.

Numerical modeling on the computer is considered to be many orders of magnitude away from the Earth in terms of several other key parameters: Reynolds number Re and Magnetic Reynolds number Rm . The Reynolds number is a measure of the ratio of inertial forces to viscous forces, and the magnetic Reynolds is a measure of the ratio of induction to magnetic diffusivity. In the numerical simulations, added viscosity and magnetic diffusivity in the form of a lower Reynolds and magnetic Reynolds number can suppress characteristic features that would be present in real flows, and also obscure whether features observed in numerical simulations would persist in the presence of turbulence and lower viscosity; properties associated with authentic representatives of the regimes being studied. Similar problems exist for the magnetic simplifications made as well, but the issues with numerical simulations are not purely due to computing constraints.

Christensen et al. [2010] point out that even though computing power available places bounds and constraints on the parameters and parameter combinations employed in Magneto-hydrodynamic (MHD) simulations of the core, these parameters can be varied within the computationally feasible region of parameter space. Yet, many published numerical simulations and models do not justify the exact values used in their simulations. It is not clear from the mathematics that the phenomena produced by such models are expected to persist within a reasonable neighborhood in parameter space of the parameter values chosen. Certainly, parameters that can be explored are limited by computational limitations, but their precise selection might be made to reproduce Earth-like behavior.

Another approach to simulating hypothetical models of core dynamics is using laboratory analogs. Laboratory models that perform actual experiments with real fluids. Experimental fluid dynamic models of planetary dynamos, though imperfect analogs as well, approximate core dynamics more closely than computers can by exploring a much vaster region of parameter space.

Laboratory experiments such as those carried at University of Maryland’s liquid sodium experiments, far surpass computer simulations in matching many of the characteristic parameters needed to test theories of the Earth’s core [Lathrop and Forest, 2011].

It remains an unsolved problem how the Earth’s magnetic field is sustained. Laboratory MHD experiments seek to replicate key features of a planetary dynamo, a self generating and sustaining magnetic field induced by the flowing electrically conductive fluid as in the Earth’s outer core; an output of magnetic energy sustained by the kinetic energy of fluid flow. For instance, Parker [1955] described a model whereby a feedback process in the Earth’s core could produce a persistent magnetic field in the presence of differential rotation. It is thought that chemical convection in the outer core causes buoyant material to rise radially from the Earth’s center, and is deflected azimuthally by the Coriolis effect induced by the Earth’s rotation, then in turn swirled in helical patterns as the process evolves. It is also thought that to a lesser extent the convection is driven by torque-induced precession as well as tidal forces and thermal convection. At high Rm the magnetic field lines are frozen in to the fluid, and are carried with the rotating flow.

For magnetohydrodynamic experiments related to core studies, it is especially important then to be able to infer the azimuthal flow so as to quantify the toroidal magnetic field induced from the twisting of poloidal magnetic field lines crossing through the core, the so called ω effect. The entrainment of frozen-in poloidal magnetic field lines by a flow can induce deformation of magnetic field lines by deflecting them in the toroidal direction as the field lines are sheared and carried by the vortex’s differential rotation. The α effect—the other component of the feedback loop—being the reconversion of toroidal field lines back into poloidal field lines; from the helical winding as it is carried with the convecting flows. Inferring the toroidal component of the internal magnetic field from sensors on the boundary is difficult magnetically, but can be inferred from the azimuthal fluid velocity field if it can be measured.

Large-scale features of the flow, such as average rotation rate in the mean zonal flow, extent of shear zones, super-rotation, and large-scale profiles of specific angular momentum in the azimuthal component of the mean flow, correlate with magnetic phenomena. The ability to char-

acterize the fluid dynamics within the system would offer a means to analyze what aspects of the fluid dynamics enhance magnetic field gain. Such an ability thereby allows a more directed search of parameter space when studying planetary dynamos. MHD rotational flows are also relevant to the study of the stars and our sun. Producing these types of flows in the lab by convection with the same means the Earth's core and stars do would be difficult, and more importantly, would evolve quite slowly.

Spherical Couette Flows (SCF) offer another means by which similar flows can be established and evolved in the lab, on realistic time scales. SCF are driven by two rotating concentric spherical boundaries encapsulating the fluid medium, and offer a means through which relevant flows can be realized in conductive fluids such as molten metals. Sodium is a commonly used metal since it is highly conductive electrically, and sodium melts at approximately 98 degrees Celsius; it is also quite cheap. Plasma-based experiments are also possible and offer a larger value of magnetic Reynolds number; liquid sodium offers a better analogue to planetary dynamos whereas plasmas may better approximate stellar dynamos. Even laboratory analogs do not match stellar dynamos very well though, with either fluid. See [Lathrop and Forest \[2011\]](#) for a full discussion thereon.

1.1.2 Spherical Couette Flows

The differential rotation in SCF is produced quite different from how a convection-driven systems. Therefore not all inherent phenomena necessarily have an analog in convection-driven differential rotation. Imaging fluid flow for SCF experiments is important to geophysical theories of the core for an additional reason: it is highly relevant to know when the observed phenomena stem from effects particular to SCF and not necessarily convection-driven dynamos or other MHD rotating flows. Being able to assess the velocity field can help determine if the flows being generated are dissimilar to those that can be generated by convection-driven dynamos, and add to the discussion on the importance of the concomitant magnetic observations during those flows. Here I focus on the hydrodynamic aspects of SCF.

The mathematical formulation and physical expression for SCF is not scale invariant; there

are effective constraints placed on the fluid medium by its composition and state variables. The geometry and velocity alone are insufficient to fully describe the dynamics; the amount of viscosity relative to the velocity and length scales also has considerable affect on the flow, as previously described.

1.2 Parameters for Spherical Couette Flows

1.2.1 Reynolds Number

One way of quantifying the ratio of viscous forces to inertial forces induced by the relative fluid rotation is the Reynolds number. High Reynolds number flows have weak viscous forces relative to inertial forces. More functionally, the Reynolds number Re serves as a proxy for the relative dominance of two terms in the incompressible Navier-Stokes Equations (NSE) description of flow in Eulerian form:

$$2\partial_t \mathbf{v} + (\mathbf{v} \cdot \nabla) \mathbf{v} = -\frac{1}{\rho_0} \nabla P + \nu \Delta \mathbf{v} \tag{1.1}$$

$$\nabla \cdot \mathbf{v} = 0$$

where \mathbf{v} is the velocity field, P is the pressure, ρ_0 is the density, and ν is the dynamic viscosity. For simplicity of exposition, the force of gravity has been neglected here, as well as other body forces due to being on the Earth, and also the forcing at the boundary induced by the moving surface. Also, this work does not use the fully coupled magnetic equations described, such as described by [Taylor \[1963\]](#), nor provide a rigorous examination of what creates the particular functional forms of the flows. Instead, the investigation focuses on reconstructing flows and associated properties mathematically from acoustics observations, drawing on the physics of the flow only when necessary to reduce non-uniqueness of results. The focus on High Reynolds number flows is not a restriction of the acoustic method employed in this work. The methods contained herein work equally well or better on laminar flows, but they are perhaps more useful for geophysical laboratory studies related to the core that are difficult to simulate on computers.

The Reynolds number is defined so as to quantify the ratio of $(\mathbf{v} \cdot \nabla) \mathbf{v}$ to the quantity

$\nu\Delta\mathbf{v}$ in a single parameter, as the ratio of the square of the characteristic velocity associated with the flow over the characteristic length scale to the dynamic viscosity ν . When the Reynolds number is very high, and the system is exhibiting a relatively steady mean flow, the viscous term and the time differential of velocity term become less significant, and the term $(\mathbf{v} \cdot \nabla)\mathbf{v}$ becomes predominantly balanced by the pressure gradient term $-\frac{1}{\rho_0}\nabla P$. In a rotating reference frame, the balance is divided between the advection relative to the reference frame and the Coriolis force; when the dominant term is the Coriolis force, the flow is said to be geostrophic. The equation is non-dimensionalized by choosing units so as to scale the characteristic length scale L and speed V of the flow using $\bar{\mathbf{x}} = \frac{\mathbf{x}}{L}$ for the spatial variables and $\bar{\mathbf{v}} = \frac{\mathbf{v}}{V}$ for the velocity scaling, and similarly, setting $\bar{t} = \frac{V}{L}t$ and $\bar{P} = \frac{1}{\rho_0 V^2}P$. Upon substitution yields

$$\partial_t \bar{\mathbf{v}} + (\bar{\mathbf{v}} \cdot \nabla_{\bar{\mathbf{x}}})\bar{\mathbf{v}} = -\nabla_{\bar{\mathbf{x}}}P + \frac{\nu}{VL}\Delta_{\bar{\mathbf{x}}}\bar{\mathbf{v}} \quad (1.2)$$

which can be rewritten as

$$\partial_t \bar{\mathbf{v}} + (\bar{\mathbf{v}} \cdot \nabla_{\bar{\mathbf{x}}})\bar{\mathbf{v}} = -\nabla_{\bar{\mathbf{x}}}P + \frac{1}{Re}\Delta_{\bar{\mathbf{x}}}\bar{\mathbf{v}} \quad (1.3)$$

Then, presuming the turbulence is not sufficiently unstable that $\Delta_{\bar{\mathbf{x}}}\bar{\mathbf{v}}$ balances the down-weighting due to Re^{-1} , the last term $\frac{1}{Re}\Delta_{\bar{\mathbf{x}}}\bar{\mathbf{v}}$ is relatively weak if the Reynolds number is sufficiently large. Computationally, Re^{-1} reduces the diffusion of small length scale variation in the velocity field, and so on a computer $\frac{1}{Re}$ being very small, leads to numerical instabilities.

In numerical schemes for NSE at high Reynolds number, small-scale features over short spatial wavelengths are created that become unstable computationally. As short wavelength features begin to emerge in the velocity field, high curvatures are created in those locations. Additional viscosity is added numerically so as to complete a feedback loop whereby as those emerging curvatures are created, the spatial variation in those locations is damped out in the velocity field evolution. Mathematically, small-scale variations increase the Laplacian where those curvatures exist, and those regions are diffused spatially by the added viscosity. Thus additional viscosity pre-

vents unstable growth of the small-scale features. However, the added viscosity has many negative consequences as well.

Added numerical viscosity removes the effects on the simulated flow that arise from the dynamics occurring at shorter length scales that would be present in the actual physical system being emulated. It also increases the amount of diffusion at larger length scales in the simulation, smoothing the velocity field even for the mean flow; though certain modern methods try to somewhat alleviate that problem by using spectral methods and controlling the diffusion at different length scales more directly. Most importantly, because NSE are highly nonlinear, the suppression of these small-scale features by added viscosity causes poor approximation even of the mean flow and larger spatial wavelength averages in solutions. Added viscosity to time evolutions of spatially dependent variables has the effect of low pass filtering the evolving variable spatially at each time step. For most linear partial differential equations such as the elastic wave equation, constantly low pass filtering the spatial variations of the evolving variable only reduces accuracy at length scales being filtered appreciably. That is because the linear differential operators involved admit a spectral decomposition whereby each spatial wavelength can be evolved separately: a normal mode decomposition. However, for a nonlinear system such as NSE, evolution of different length scales cannot be so easily decoupled. The constant low pass filtering of the velocity field during the simulation means that the simulation will not be accurate even at the length scales not directly filtered appreciably from time step to time step. Similar issues also arise from adding unrealistic magnetic diffusivity, and also the interaction between the fully coupled magnetic and hydrodynamic equations. These are highly relevant flaws in numerical simulations of geophysical and astrophysical dynamos. It is critical in such simulations to accurately capture the manner in which energy is exchanged between components of the system at different length scales.

Laboratory experiments seek to sidestep the unrealistic effects of the artificial damping out of turbulence and damping out of small-scale features of the velocity field. The length scales over which turbulence are active is far smaller than the domain discretization or spatial resolutions employed by most computer models; a problem less pronounced by using analogous physical fluid

dynamics that can be generated in the laboratory. Even if sufficient computer memory to store a model of sufficient resolution to evolve at the length scales of turbulence is available, and sufficient computational resources to overcome the corresponding small time step required are present, there is still the matter of efficiency. Laboratory data can be collected from very long duration simulations in real time, as opposed to computer simulations that may take weeks or months or even years to produce seconds or minutes of simulation for the same regime as the laboratory experiment. Computer simulations have one distinct advantage over laboratory experiments though: direct access to the physical variables throughout the entire domain at each time step. Taking advantage of the benefits of laboratory experiments then, requires developing methods to infer those variables in the manner needed.

Creating flows in the laboratory more analogous to those theorized for core-like flows and magnetic behavior, requires the use of electrically conducting liquids or plasmas and devices less amenable to traditional means of inferring the advecting fluid’s velocity field. The kinematics, temperatures, and vessel designs involved with doing such experiments on practical time scales make velocimetry more difficult, as does using liquid metal or using any other opaque fluid. This work presents alternative means of inferring velocity remotely from the boundary of the vessel, focusing on zonal flows in a core like geometry. For a discussion of modeling the Earth’s core with liquid sodium flows, refer to [Adams et al. \[2015\]](#). This work does not address in any detail the direct relationship to the Earth, its geometry or location in parameter space in regard to various quantities, or the strength of the analogy between SCF and the Earth’s core.

1.2.2 Ekman Number

For SCF, when observing in a rotating frame, the characteristic velocity scale used in the Reynolds number is relative to that frame, and another term helps characterize the flow. Noting the analogy between V_{lab} and the quantity $\Omega_o L$, the Ekman number for SCF is defined by

$$E_k = \frac{\nu}{2\Omega_o L^2} \tag{1.4}$$

where Ω_o is the rotation rate of the outer sphere, and l is the outer radius R_o . The Ekman number can be interpreted as the ratio of viscous forces to Coriolis forces. The derivation for it parallels the derivation for Reynolds number, after substituting the Coriolis force into the left hand side of the momentum equation in NSE. For sodium experiments, the Ekman number can be less than 10^{-7} ; for air during the experiments this work produces inversions from is approximately $\cdot 10^{-6}$. For the Earth's outer core, the Ekman Number is thought to be even as low as 10^{-14} or less, or several orders of magnitude higher depending on the value of kinematic viscosity used, one of the least understood parameters for the outer core; see [Secco, 1995, Olson, 2011, see].

1.2.3 Rossby Number

Another useful parameter for SCF is the Rossby number, which is defined slightly differently in SCF than in Atmospheric sciences. The Rossby number in SCF is given by

$$Ro = \frac{\Omega_i - \Omega_o}{\Omega_o} \quad (1.5)$$

where Ω_i is the angular velocity of the inner sphere in the SCF. It can be interpreted as the ratio of the inertial forces to Coriolis forces, the length scale having been obscured due to algebraic simplification in the expression. The net angular velocity appearing in the numerator is very important for numericists. It should be noted though, that only a very small portion of the fluid cavity will follow the inner sphere rotation rate. Even outside that boundary layer, the fluid tapers off quite quickly in most regimes, and the Rossby number might not adequately characterize the bulk fluid flow. To within an order of magnitude accuracy, though, it may be said that

$$Re = \frac{Ro}{E_k} \quad (1.6)$$

The relation follows by noting the numerator of the Rossby number expression is the angular velocity of the fluid relative to the rotating frame, and can be used to express the velocity scale in the Reynolds number, and then after cancellation of the length scale factors the relationship

follows trivially.

Often it is convenient to work with inverse Rossby number Ro^{-1} . This is because when the outer sphere is stationary and only the inner is rotating, Ro would be infinite. In the limit that Ro^{-1} goes to positive or negative infinity the flow becomes geostrophic in the canonical idealized sense and the Taylor-Proudman theorem applies throughout the cavity. As inverse Rossby tends to 0, the Coriolis effects on the flow become negligible and the rotation induced by the inner sphere dominates as if the outer sphere were having no effect, except perhaps in a thin viscous boundary layer. The regimes analyzed in this study do not quite approximate either endmember though.

1.2.4 ω Effect

Shear in SCF of MHD experiments is thought to enhance magnetic field gain by converting poloidal magnetic field components into toroidal magnetic field components. Consider an azimuthal velocity field given by $\Omega(r, z)$. For simple axial dipole dominated magnetic fields, the forcing term involving the poloidal field in the induction equation for the toroidal component is described approximately by

$$\partial_t T = -(r\partial_r\Omega)(\partial_z P) + \frac{1}{R}(\Delta - \frac{1}{R^2})T = 0 \quad (1.7)$$

where Δ is the Laplace operator, and T is the toroidal component and P is the poloidal component in the Helmholtz decomposition of the field; the simplicity coming from the fact that the magnetic field has zero divergence. In this form it can be seen that shear in the rotating fluid by way of $r\partial_r\Omega$ allows the poloidal component to serve as a forcing term to the toroidal component of the magnetic field. This is why the zonal flow velocimetry is important to testing many hypotheses related to magnetic field gain in MHD experiments. To that end,

$$\omega_{\text{effect}}(r) := r\partial_r\Omega(r) \quad (1.8)$$

1.3 Velocimetry of Fluid Flows

1.3.1 Challenges of Traditional Techniques of Velocimetry

In situ observations of experimental and natural fluid flows present many difficulties; they are disruptive to the flow, acquisition can be difficult or economically prohibitive, and the coverage of the domain is often either limited or greatly asynchronous.

With such direct measurements, flow diversion and turbulent wakes around the instrument of observation can disrupt the flow, as well as initiate dynamics in the flow that persist. This is especially true at scales of experimental fluid dynamics. The invasive nature of simultaneous direct sampling of the fluid domain with a dense sensor array is discouraging. The alternative of sampling fewer portions of the domain introduces then issues of aliasing and sampling bias. More remote, simultaneous, and less disruptive means of interrogation of the fluid are preferable. Remote observation of fluid flow can be accomplished by several means.

Traditional methods of fluid velocimetry that are less obstructive mainly include optical techniques such as Particle Image Velocimetry (PIV), Laser Doppler Velocimetry (LDV), and also ultrasonic techniques such as Ultrasonic Doppler Velocimetry (UDV). PIV measures the displacement between visible particles in the fluid over time to infer the velocity field. LDV and UDV utilize the Doppler shift the moving particles induce in waves reflected off those particles, optical waves in the case of LDV and acoustic waves in the case of UDV. Each of the traditional methods has advantages, but also many disadvantages; in many cases they do not even work.

PIV and LDV methods require that the material not be opaque in the part of the light spectrum the instrument sees in. Flowing liquid metal is an opaque material, and is especially difficult to probe using optical techniques, making both PIV and LDV impractical. PIV is arguably only negligibly disruptive to the flow, but it is certainly invasive. Reliable performance with PIV requires particles inside the domain matched in density, resistant to corrosion, in the case of liquid metal resistant to melting, and distributed in a manner conducive to the needed coverage. It is extremely difficult to match the particles density to that of the fluid, especially when the fluid

does not have static state variables, and ultimately over relatively large time scales the particles either sink, rise, or obey transits in the moving fluid that do not sample the medium uniformly. Constantly replacing the particles or resetting them is cumbersome and economically discouraging in terms of labor and time consumption, and even potentially dangerous.

UDV has been shown to work in liquid metal [Takeda, 1991], and does not require additional particles placed in the medium; [Takeda, 1991] suggests air bubbles as sufficient to explain the reflections of the sound waves. In liquid sodium, the fluid used in many magnetic related experiments, oxides floating in the medium are thought to serve as the objects that reflect the sound waves from which velocity is inferred [Nataf et al., 2008]. In liquid sodium filled SCF, UDV has been shown to be difficult [Sisan et al., 2004], partially motivating this study. UDV relies on very high frequency acoustic waves. That means that UDV requires a wetting of the surface between the instrument and the fluid. Ultrasonic waves can be disrupted by layers of gas forming between the fluid and the container boundary where the acoustic source is, a layer thicker than the wavelengths of the ultrasonic sound; without wetting, the waves will tend to reverberate inside the gas layer more so than transmit through the sodium and back. Also, it is thought that the tracer oxides may not distribute evenly due to centrifugal and gravitational effects; presumably the oxides have a slightly different density that would potentially bias them more toward one part of the cavity than another.

In order to sample larger portions of the domain, UDV LDV and PIV require either large amounts of instrumentation or instrumentation that can have its target direction modified continuously. Such modification is challenging for large vigorously rotating setups with mounted instrumentation. Methods that sample substantial portions of the domain and whose sensors do not favor a particular directionality or sampling line are preferable.

1.3.2 Acoustic Normal Mode Inverse Spectral Methods

Acoustic normal mode inverse spectral methods offer a means of mathematically reconstructing fluid flow remotely, requiring only observation at a few locations along the boundary of

the medium. They are capable of imaging the entire medium on relatively short time scales. By virtue of their indirect sampling of the whole medium, they thus also avoid the problems associated with spot measurements or sampling bias towards a narrow beam as in UDV. The longer wavelength nature of low frequency normal modes also allows them to couple to the fluid medium even in the presence of a gas layer between the container wall and the fluid. This work focuses on one such method, the adaptation of normal mode seismology, an inverse spectral method, to fluid velocimetry.

Acoustic inverse spectral methods use the transformation to the spectrum of the acoustic free oscillations to invert for the fluid velocity, analogously to how normal modes of the Earth are used in seismology to infer properties of the bulk Earth. Normal mode seismology uses sensor arrays on the Earth’s surface or in the shallow subsurface to infer bulk properties of the deep Earth such as density and soundpseed, the excitation sources primarily being large earthquakes. This form of remote sensing known as helioseismology was adapted by the heliophysics community to study the interior of the sun [Thompson et al., 2003]. Helioseismology uses the analog of sound waves in the sun’s interior, acoustic waves whose primary restoring force is pressure—to image the rotation of the sun’s interior. SCF in the regime where azimuthal flow dominates has an analogous geometry and flow to the interior rotation of the sun. Both seismic tomography of the Earth and oceanic tomography often employ acoustic normal mode based inverse theory, but also supplement their knowledge with other data such as travel times of body waves propagating from a source to a receiver, to reveal smaller scale features. Like helioseismology, this work only uses normal mode spectra.

Pressure perturbations from a speaker or source device induce propagation of small amplitude compression waves in specific frequency bands. If the source is sinusoidal and delivers enough energy at or near the frequencies of modes of free oscillation for the cavity, then resonance occurs and the amplitude of sound swells at that frequency. That is, when the small acoustic source device such as a speaker drives a piece of the medium at or near one of the natural frequencies of vibration of the sounding cavity, large amplitudes of vibration at that natural frequency occur

inside. The distribution of power across the acoustic spectrum has localized peaks at the resonance frequencies. The location of those peaks can be modeled as function of the velocity field, and both a predictive model for the acoustic spectra based on a flow as well as inversion schemes can be created therewith. Many aspects of the flow and state variables can shift the frequencies, but in particular it is the splitting between modes with nonzero azimuthal wavenumbers $+|m_s|$ and $-|m_s|$ that is the most informative and least ambiguous effect of the azimuthal flow. This will be addressed in detail throughout this work.

The acoustic modes of vibration associated with these spectral peaks can be excited in several manners. Combing through a broad frequency range is possible with a chirp source function such as the function $\sin(\lambda t \cdot \omega_i t)$, which for sufficiently small lambda delivers an instantaneous sinusoidal source with frequency $\omega(t) = \lambda t \omega_i$, with ω_i being the initial frequency the chirp starts at, and λ being the chirp rate. In cases when the flow generates its own sound or when other sources of ambient noise are present, active sources may not be necessary; though I would argue preferable. Such ambient noise produces less accurate and relatively noisy spectra, since amplitude envelopes are created across different frequency bands possibly due to time varying excitation or time varying attenuation. Also, the signal to noise ratio is not as high. For instance, for a simple sinusoidal amplitude envelope in the time domain, the effect on spectra amounts to convolving with two delta spikes about the origin in the frequency domain.

Suppose a simple example such as

$$\gamma(t) = \sin(\pi t) \sin(2\pi f t) \tag{1.9}$$

then

$$\mathcal{F}\gamma(t) = \mathcal{F}\sin(\pi t) * \mathcal{F}\sin(2\pi f t) \tag{1.10}$$

where F denotes the Fourier Transform. Then once looking at $|\mathcal{F}\gamma|^2$, the convolution has taken the approximately Dirac impulse that would occur due to a resonance at frequency f and places two Dirac impulses 1 Hz apart centered on f. Since not every band has the same envelope nor are the

bands easily disentangled. This effect cannot be removed so easily. Shortening the time window to see more short term behavior accrues defocusing as a result of reciprocal spreading in the frequency domain; i.e. there is an implicit time window function and reduced frequency resolution on top of any defocusing for purely physical reasons.

In this work, both chirp based data and ambient noise data are used. Chirp-based data, targeted to excite modes by chirping through a band around the resonance, are used to assess relevant aspects of the theory and match between the numerical modeling and the laboratory setup data. Ambient noise based data sets with larger numbers of computed splittings are used to perform inversions on data.

Small acoustic pressure perturbations to the medium have negligible affect on fluid flow. Sound waves manifest as compression perturbations in the medium and are approximated as having no affect on the flows in this work for that reason.

The central physical phenomenon of interest in this work is the velocity distribution of the fluid inside the acoustically resonant cavity; specifically, the mean flow, the time averaged azimuthal velocity profiles, presumed to be predominantly azimuthal and axisymmetric in SCF. As such, often it is more convenient to work with angular velocity, and rotation rates will be spoken off in place of velocities.

Meridional flows and other inherent features are presumed sufficiently less vigorous in these flows of interest, and are not included in the modeling of the flow explicitly. Though meridional flows and other types of poloidal velocity contributions are not explicitly incorporated into the physical model of the flow for purposes of inversion, discussion of their effects in certain regimes and relation to how they modify the accuracy of the inversions is considered. In cylindrical coordinates with z aligned with the axis of rotation, for a flow component in the r,z directions, to first order the splittings of the modes are not affected. Higher order effects are possible if the flow is vigorous enough to appreciably distort the mode shapes, and are discussed in later sections of this work. Here, I will briefly discuss the dominant effect on acoustic splittings, the fine structure of the acoustic spectrum caused by azimuthal flows.

A standing acoustic wave inside the rotating flow within the cavity is transformed by Coriolis forces and advected due to the transit of the fluid on which it is superimposed. It also is affected to a lesser degree by centrifugal forces and body forces, as well as slight anomalies in wave speed in the medium; these are shown to be sufficiently small that they can be neglected. Modes that have an azimuthal wave number that is non-zero, have a spinning pressure pattern. When the fluid is at rest, the frequency observed at the boundary comes from an invariant pressure pattern spinning, the relative amplitudes crossing the sensor with the time evolution. It is important to stress that it is not the material that spins, but, rather the relative amplitude pattern of the modes that does.

Cylindrically radial motions and lateral motions of the fluid caused by the acoustic wave are transformed by the Coriolis force, causing the mode to be offset slightly; the eigenvector is perturbed and also gets a small imaginary component, but the frequencies remain real. Advection affects splitting due to mode's spin being relative to the fluid, to first order. Whether the spin is retrograde or prograde affects whether the spinning mode will spin faster or slower once the fluid starts moving. If the sensor/microphone is at rest, and the fluid motion advects the spinning mode by spinning the fluid in the same orientation as the mode, the mode spins faster in terms of the frequency observed at the sensor/microphone since it is spinning relative to the fluid medium. If the spin of the mode is opposite the fluid motion, the fluid motion slows down the spin, and lowers the frequency. As such, the frequencies observed in the lab frame are not the same frequencies observed in the rotating frame, except nominally for the spherically symmetric modes whose pressure pattern does not spin.

Since there can exist acoustic standing waves with markedly different modal shapes in the cavity, their frequency shifts and spectral alterations can differ from one another depending on the distribution of the fluid velocity; in other words, they have different sensitivities to flow. With appropriate observations of specific acoustic mode frequencies, and constraints from the theoretical physics governing the flow, the fluid velocity field can be reconstructed by inversion. Resolution and accuracy of that reconstruction depends largely on the number, complimentary spectral sensitivity of the employed modes, and quality and accuracy of the measured spectra. The reconstruction is

of the mean flow, where the time integration is on a time scale related to the time window of the data acquisition and spectral estimations. Within that time window, flow is modeled as having an invariant mean profile with superimposed transient and possibly turbulent components that do not fluctuate so vigorously as to significantly warp or displace the spectra from one that would be produced by the mean flow in their absence.

It is the intent of this study to develop methods and software applicable to future laboratory experiments, capable of handling irregular geometries associated with actual setups, and to produce inversions demonstrating the capabilities and limitations with current data. SCF setups in labs require shafts to spin the inner core, provide stability, hold the inner core in place. This work abandons the approximation of a spherical annulus/shell, and performs a Finite Element Method to more accurately incorporate those structures, so as not to distort the flow nor incur undue error in the forward problem. The formulation would work equally as well for a Taylor Couette flow, a flow induced by two concentric rotating cylindrical surfaces, or any other azimuthal flow with symmetry about the axis of rotation. Coupling magnetic equations to NSE formulation of the fluid flow is not necessary since air is not electrically conducting to any relevant degree.

Posterior error analyses for inversions often state their uncertainties in terms of the model parameter uncertainty or covariance. In these types of reconstructions though, what is potentially of the greatest significance is not the amount that the model parameter values would change as a result of uncertainties in the data. The greatest significance is how accurately the true mean flow can be reconstructed by the form of parametrization used. In the absence of the shaft and related asymmetric missing pieces and sensor apparatus, the sensitivity kernels (discussed in chapter 5) are even about $z = 0$ for an axisymmetric azimuthal flow. This means that an odd component to a flow would produce no splitting contribution. Since any axisymmetric azimuthal flow can be written as the sum of a component even about $z = 0$ and a component odd about $z = 0$, and the component that is odd can be scaled arbitrarily without affecting the acoustics to first order, it is effectively invisible to the spectra. For this reason, and the fact that the flow is not expected have its mean azimuthal flow deviate from axisymmetry or evenness about $z = 0$ substantially, this work confines

itself to studying the even component of the flow. Slight asymmetries exist in the experimental setup that do possibly lift that ambiguity, but are small enough that the effects would be conflated with the noise and uncertainties inherent in the data. A feature that occurs superimposed on top of the flow in only one of the top or bottom hemispheres, will be averaged equally into both the top and bottom hemispheres. That must be taken into account when interpreting features in inversions.

Splitting between the modes with azimuthal wavenumbers $+|m_s|$ and $-|m_s|$ are linear in the azimuthal rotation of the fluid, for the regimes examined herein. The splittings can thus be expressed as a composite effect of the splittings induced by a collection of basis functions whereby the weighting each basis flow's induced splitting is weighted in the overall splitting by the same weighting of the basis function in the synthesis expansion of the flow. A set of splittings can be predicted from any flow, and an inverse problem can be formulated for the coefficients of the basis flows based on measured acoustic spectra.

This work primarily concerns itself with large-scale properties of the mean flow. It focuses on developing methods that can be applied when only a limited number of spectral measurements are available, constrained to using only a few sensors that are perhaps not ideally located for more sophisticated array processing techniques. Testing of methods on data is confined to air, since sodium data is not currently available.

1.4 60-cm Setup

1.4.1 Laboratory Configuration

This work uses as a case study data collected from a 60 cm diameter titanium vessel filled with air, the inner core radius approximately 1/3 the outer, the outer spinning at 6 Hz and the inner core spinning in the range of -4 to -40 Hz. The vessel is described in detail in [Adams, 2016].

The 60-cm setup, Dynamo 3.5 at the University of Maryland Nonlinear Dynamics Laboratory, is a SCF setup. It has a diameter to the inner boundary of the outer shell of 60 centimeters. The dimensions used in the modeling are $R_o = 0.3048$ and $R_i = 0.1000$. The outer enclosure is

made of titanium, whereas the inner core is copper. The inner sphere is spun by an axle that rotates with it during the experiments, and the axle is enclosed inside a shaft for support, though the shaft is welded to the outer shell and spins with the outer sphere. Small pieces of the shaft covering the axle were removed where it meets the inner sphere. In strictest terms, these additional components violate the idealization inherent in SCF. The inner sphere must not only be spun, but must also be held in place. One difference between the 60-cm setup and other experimental SCF setups, is the shaft is much larger and it spins with the outer sphere rather than with the inner sphere. The axle spins with the inner sphere, though barely exposed. As can be seen in figure 1.2, the electronics placed on the boundary for microphones are quite small, especially when the fluid near the outer shell in those regions is not deviating from the rotation rate of the outer.

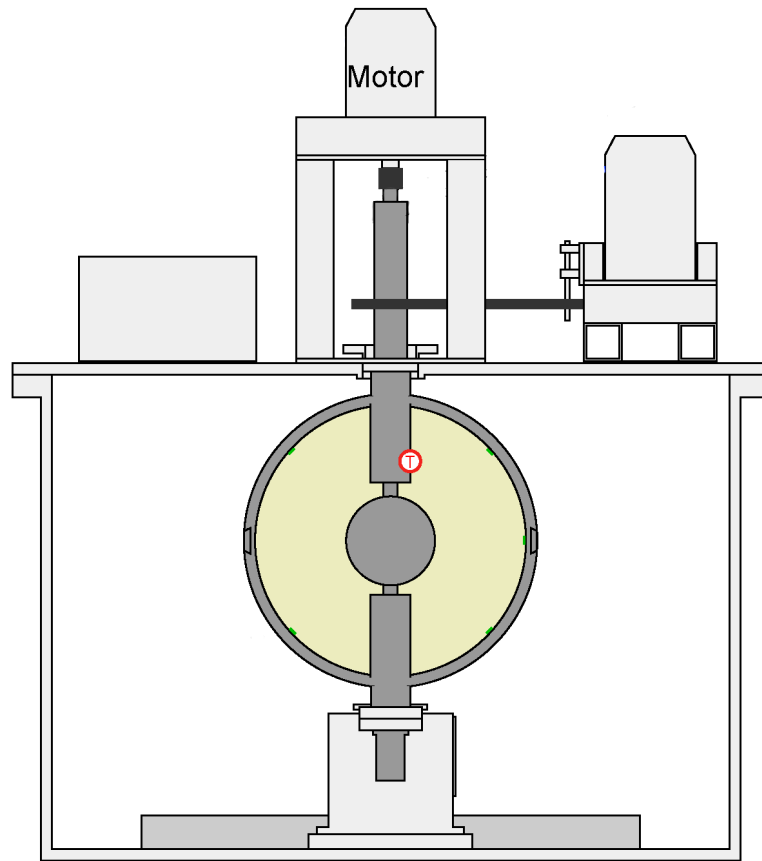


Figure 1.1: Schematic of the 60-cm setup and configuration in the lab. Diameter of the outer sphere is approximately 60 cm and of the inner sphere is a approximately 20 cm. Diagram courtesy of Matthew Adams.



Figure 1.2: Interior of the 60cm Setup taken apart showing electronics mounted inside, before assembly. The setup tries to minimize the invasiveness of the electronics. The axis of rotation, embodied by the physical axle, is vertical during operation. Photographs courtesy of Matthew Adams.

The housing encasing the structure, as seen in figure 1.1, is related to safety measures for the sodium experiments. The red “T” indicates the placement of the thermometer in the cavity. The device was originally used for liquid sodium experiments. The acoustic recordings collected for this work were performed by Matthew Adams, who also built many of the devices used to retrofit the device with the acoustic equipment for sound production and recording. For a full discussion of the setup, refer to Adams [2016].

1.4.2 Modeling the Geometry

The geometry is modeled as being an axisymmetric volume of revolution of the cross section depicted in figure 1.3. The shaft is approximately 44% the radius of the inner sphere, and has approximately 75% as large a surface area within the cavity’s interior. The axle is approximately 25% the radius of the inner sphere. The sphericity of the spheres is exceptional, and the shells on the boundary of the fluid only deviates from being spherical by one part in one thousand, insofar as the curvatures at welded joints and other aspects are ignored along the shaft [Lathrop, personal communication].

Meridional Cross Section

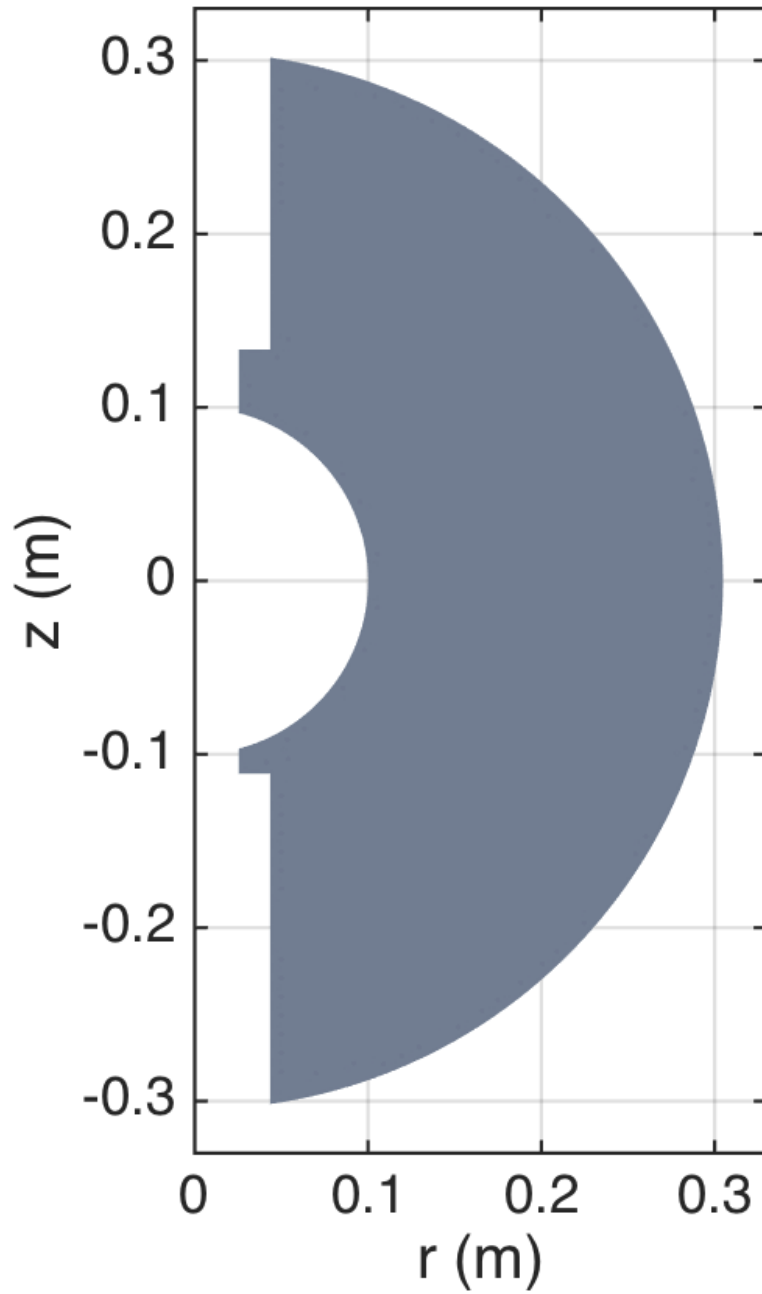


Figure 1.3: Meridional cross section of the geometry, showing the proportions used to model the cross section. The z -axis is the axis of rotation where the axle and shaft are.

Chapter 2: Previous Work in the Field

2.1 Analysis and Discussion

[Triana et al. \[2014\]](#) presented a study of spherical Couette flow using air in a small vessel whose outer shell’s radius was approximately 15cm, the inner core radius approximately one third of that, and the inner rotating and speeds up to 36 Hz; the outer sphere stationary. Since the outer shell was stationary, anemometer readings could be taken easily. Flow profiles taken by the anemometer showed that the flows were quite similar at the two elevations measured, which can be interpreted to suggest significant vertical invariance of the flow. [Triana et al. \[2014\]](#) also attempted an inversion of acoustic mode frequencies for the flows. The inversions utilized damping to regularize the inverse problem, since for the flow parametrization used, it was under-determined. While many aspects of the inversion procedure were straightforward, the nuance of applying it to laboratory SCF merits some discussion.

In particular, methods employed in the self described “proof of concept” study carried out in [Triana et al. \[2014\]](#) could not yield an unambiguous choice of regularization parameters, which were ultimately chosen based on the anemometer data [[Triana, Personal Communication](#)]. In this section I will discuss that work, which is to the best of this Authors knowledge, the only other published work in experimental SCF using helioseismic methods. To do so, I will first recast the inversion method formulation in a different form, so as to foster a theoretical analysis rather than a computational approach.

Consider the traditional weighted least squares problem, cast in an optimization form with objective function Φ . Let C be the forward operator, d be the observed data vector with uncer-

tainties modeled by σ , and m the model vector of fitting parameters over which to minimize

$$\Phi(m) = \frac{1}{2} \|W_d(Cm - d)\|^2, \quad (2.1)$$

where $\Phi(m)$ is called the data misfit in this context and W_d is a weighting of the data by some form of inverse data standard deviation matrix, or confidence measure based the data uncertainties. In the case of uncorrelated errors, a diagonal matrix with reciprocals of the uncertainties of each entry in the data vector d is most typical, which was what was used in [Triana et al. \[2014\]](#). W_d is analogous to an inverse data covariance matrix for data uncertainties that are standard deviations of a sampling of a random process. To prevent unphysical solutions and lift the ambiguity of the answer owing to the under-determined nature of the problem, regularization was used.

Regularization by damping is a method that seeks to minimize the Φ in the presence of a penalty function $\|D(m)\|^2$ as follows:

$$\Phi(m) = \frac{1}{2} \|W_d(Cm - d)\|^2 + \epsilon \|D(m)\|^2, \quad (2.2)$$

where ϵ controls the trade-off between data misfit and regularization, and D is typically some linear function of the flow such as a differential operator like the Laplacian or second derivative with respect to some spatial coordinate(s). The trade-off arises from the relative minimization of the two terms in the expression for the objective function Φ ; the first term is often called the data misfit. As can be seen from [Eq. 2.2](#) the choice of ϵ is only scale invariant with respect to the flow magnitude when W_d is not a function of the scale of the flow; i.e. when the uncertainties do not change as the magnitude of the flow or flow pattern changes, possibly due to changing the rate of the inner sphere. Though it cannot be judged from the composite uncertainties presented in [Triana et al. \[2014\]](#), examination of the actual data collected in the study shows that the uncertainties are not invariant as a function of the flow. It is implicitly understood that if the number of data observations changes, that ϵ must be scaled accordingly as well, else the trade-off does not have the same proportional weighting. More importantly, how ϵ is chosen is critical. To motivate that

discussion, first I will address other features of the formulation.

It can be seen that the damping in Eq. 2.2 is not done point-wise or in any localized sense; it is expressed as a norm, an integral over the volume of the cavity in the case of [Triana et al. \[2014\]](#). As a result, different choices of ϵ will not only cause trade-off with data misfit, but also cause the degree of regularity in the domain to trade-off from one region to another. That behavior is beneficial for a large data set, since localizing in a region at the expense of increasing penalty function term trade-offs with the localized increased curvature's ability to decrease the data misfit. With small data sets that do not have good coverage across the whole domain, this behavior results in ambiguity due to many possible ways of localizing high curvatures that fit the data. Ambiguity is created when solutions produce similar values of the objective function even with the included penalty term. Many methods attempt to lift the subjectivity of regularization parameters that lift the nonuniqueness, such as optimally localized averages and minimization of functionals defined on the resolution matrix of the inversion. [Triana et al. \[2014\]](#) did not use such functional minimization explicitly, but suggested optimally localized averages as a form of improvement. I will address both the method used in [Triana et al. \[2014\]](#), and also why there are similar difficulties encountered with that suggested improvement as well.

In the case of the Tikhonov regularization, [Triana et al. \[2014\]](#) chose to damp curvatures in the spherically radial direction and the polar angle direction. Various metrics were used as motivation for the choice. First, it is important to be aware of certain aspects of inverse spectral methods, to put those metrics in context.

Inverse spectral methods are quite dissimilar from fitting surfaces or curves to control points or direct measurements of the profile being reconstructed. In the case of these types of acoustic methods, how well the inversion is able to predict the acoustics data is quite different from how well it is able to predict the flow. If measurements of the flow at points inside the cavity are used, then enforcing smoothness on the solution amounts to preventing oscillation in the reconstructed profile; the inversion is thus interpolating between data points measured inside the flow while allowing tolerance to the fit at measured data points when it reduces the curvature of the solution

overall, based on some metric to judge the trade-off between the two ideals of fitting the data enforcing smoothness. When the data measured is indirect, as in acoustic spectral methods, and not measurements of the variable that is being reconstructed, problems can occur.

In theory, with sufficient data, the quantities directly measured and the properties reconstructed by inversion are in a strong correspondence and this subtle issue is of little concern. Helioseismology typically uses several hundred measured modes to obtain results considered accurate in the outer convective zone, and arguably in the upper most portion of the radiative interior, losing resolution closer to the poles. In the experimental 30cm setup, those analogous regions of the cavity the method is best suited for were nearly at rest, and all interesting features were primarily localized within the tangent cylinder. Furthermore, fewer than 30 modes were used. Therefore, the problem tackled by [Triana et al. \[2014\]](#) is not an easy inversion to perform, regardless of the method or approach.

Many disciplines use a prior model of the quantity being inverted for, using damping of curvature via covariant differentiation relative the background model; extreme damping then just reproduces the background prior model. In this case, solutions trade-off between endmembers. One endmember, corresponding to no damping, perfectly reproduces the data at the expense of being unphysical or fitting the noise. Another endmember, corresponding to maximum damping, perfectly reproduces the background prior model by damping out all deviation therefrom. Damping in several variables can be formulated as a single variable of damping, with a relative weighting between the components of the damping operator being another tuning parameter.

[Triana et al. \[2014\]](#) used a Tikhonov regularization method that damped the second derivatives of the spatial coordinates 1) the spherical radius R , and 2) the polar angle θ . Damping in the spherically radial R and polar angle second derivatives, means that latter endmember is a flow linear in R and linear along each polar latitudinal curve. The first linearity in R is very unrealistic at the high Reynolds number in the flows inside the 30 cm setup during the experiments. The second linearity in polar angle is somewhat bizarre in that context, though the constraint of the evenness of the solution about $z=0$ imposed in the study modifies that constraint to tend toward

being invariant along polar angles θ as the damping tends to infinity; again, that means the solution is spherically symmetric though, which is quite unrealistic unless the viscosity was many order of magnitude higher. Such a regularization scheme is not a problem when there is a plethora of data, in which circumstance the damping need only enforce continuity or some small amount of regularity in the reconstruction. However, it does pose problems when using so few observed modes.

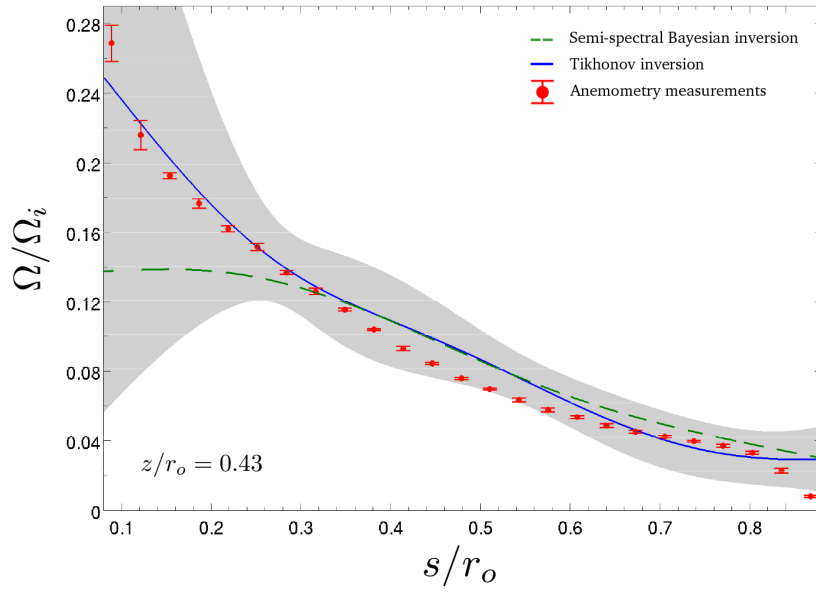
High shear zones, which are present in MHD studies, present another problem in that context. Regions of high shear in the flow will be defocused when damping is based on curvatures because high shear zones have sharp curvatures; it is unavoidable in the absence of choosing a biased parametrization or biased damping strategy. With a small data set, there is not enough resolving power that a smoothed and reduced shear in the solution would significantly degrade data misfit. Furthermore, the extent to which the shear zone is smoothed out also trades off with smoothness in the rest of the domain. If a particular mode is much more sensitive to a region than the rest, the solution will tend to produce a flow that poorly fits that mode's splitting, and then correct the issue by placing larger flow in the region(s) it is relatively uniquely sensitive. The expense to the misfit of the other mode spectra is negligible in such a case. Regularization can only prevent such behavior when it smooths the solution sufficiently that it cannot oscillate over length scales as large as the smallest region of reduced complimentary sensitivity in the modes used.

So, with small amounts of observed modes and non-ideal resolving capabilities, there is no way to preserve shear unless additional biasing assumptions are made. Since the penalty function in Eq. 2.2 is an integral in this context, it will then trade-off with curvature in other regions of the domain. With limited data, that is difficult to overcome and reconstruct the shear correctly. The variables chosen, the spherical radius and polar angle variables, also penalize a geostrophic flow or one that is somewhat vertically invariant more so than a spherically symmetric flow linear in the radial and/or polar variable. For spherical Couette flows well beyond the laminar regime, a strong component that is vertically invariant is expected, especially outside the tangent cylinder and away

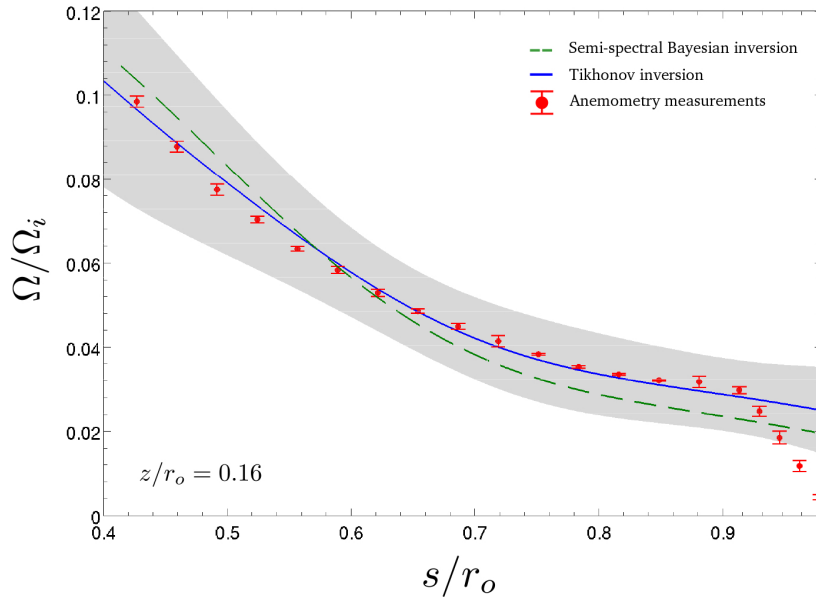
from any jet instabilities after the velocity field is time averaged. The anemometer data in [Triana et al. \[2014\]](#), even though it only sampled limited locations, also supports that contention.

It would be perhaps better to use the cylindrical coordinates r and z for curvature damping when the flow has a strong vertically invariant component, applying light r curvature damping, and heavy z curvature damping. Either way, it raises the issue of whether a feature is being created or reconstructed. For example, z curvature damping may create cylindrical symmetry in the reconstruction when it is less pronounced in the actual flow, whereas in the case of spherical parameters used in R , θ curvature damping may erode the cylindrical symmetry in the inversion despite cylindrical symmetry being dominant in the actual flow. With only several dozen splittings for an inversion, one should not expect to obtain similar inversions using both methods without additional information or severe loss of resolution, because with scant data and gaps in coverage, the damping must do more than enforce continuity. The damping must constrain the solution by supplementing the data to a considerable degree. The ultimate difficulty with constraining the solution by damping in the context of very limited data, is the choice of damping parameters is largely subjective even when more advanced means are used to select them.

Ultimately, damping parameters for the Tikhonov regularization in [Triana et al. \[2014\]](#) were chosen so as to minimize the misfit of the inversions with the anemometer profiles of the flow [[Trianna, Personal communication](#)], and the motivating analysis did not yield an unambiguous justification for the damping parameters. As a result, the inversion fit the profiles well even inside the tangent cylinder where the mode set chosen had relatively little sensitivity. [Figure 2.1](#) shows the result for two inversions, the Tikhonov and semi-spectral Bayesian approaches; it also shows what the anemometer data inferred as the rotation profile.



(a) Scaled angular velocity at $z/r_o = 0.43$



(b) Scaled angular velocity at $z/r_o = 0.16$

Figure 2.1: Reproduction of a figure from [Triana et al. \[2014\]](#), showing anemometer profile and level of consistency with inversion profiles, as well as posterior uncertainty estimates. s is cylindrical radius, r_o is the outer sphere radius.

If the inversion had been done as if the profile was unknown, and still recovered these profiles, that would suggest robustness of the choice of inversion parameters and perhaps an over estimation of the levels of uncertainty inherent in the shaded region in figure 2.1 expressing the posterior error bounds. However, since damping parameters were chosen minimizing RMS error along these profiles, it is actually somewhat expected that this result is obtained. In fact, it is actually somewhat surprising it doesn't fit the anemometer data better. I will address why it doesn't fit better shortly. The motivation for modal based acoustic velocimetry in MHD experiments though, is to be able to infer velocity without a tool such as anemometers or UDV; as such means are often not available. Even if an experiment can supplement its acoustic observations with traditional UDV in a manner analogous to the anemometer recordings, other issues arise, and are discussed below.

As can be seen from figure 2.1, even from that choice of damping parameters the posterior error distribution shows a large distribution of velocity profiles consistent with the data under the stated uncertainties, though the covariance cannot be gauged from the plot. The bounds of the distribution is so large that it does not fit inside the plot they presented. One possible reason for this, is that minimizing the root mean square error along the anemometer profile with respect to cylindrical radius r placed equal weighting at each cylindrical radius r despite different r values being associated with different volume of fluid, and the modes used being much more sensitive to flow outside and away from the tangent cylinder. An inversion performed this way should fit the data better where the modes have more resolving power, and the data will be better predicted by the reconstructed flow. Personal investigation with this mode set found that reconstruction outside the tangent cylinder was somewhat robust to changes in damping parameters, but inside the tangent cylinder could produce very large changes in the profiles relative to very small changes in the damping parameter. If the flow is not approximately vertically invariant then, even if UDV measurements were used in an analogous manner as the anemometer data there is no guarantee it will accurately reconstruct the flow anywhere besides along the UDV profile. On the other hand, if the flow is presumed to be relatively vertically invariant, and one has a UDV profile

along a cylindrical radius, then the importance of an acoustic inversion is greatly diminished. The reconstructed profiles in figure 2.1 are thus at best a test of consistency.

The work also showed other criteria like averaging kernels and error magnification. Averaging kernels are rows of the resolution matrix, though as a function of space rather than arranged as a vector stack's dual. They quantify the diffusion from basis function to basis function as a result of the inversion operator mapping from the model space to itself. More specifically they quantify the diffusion into a basis element from the others by giving the relative weighting of flow in the region of space contributing the reconstructed flow. The reconstructed model parameter is a weighted average of the flow, which if expressible in the parametrization associated to the model parameters, amounts to a weighted average of the model parameters describing the flow. When the model parameters are the values of flow at grid points or a fine tiling of the domain, then

$$\bar{m}_{r_o z_o} \approx \int_{rz} \mathcal{K}_o(r, z) m_{rz} \quad (2.3)$$

where $\bar{m}_{r_o z_o}$ is the recovered estimate for the model parameter $m_{r_o z_o}$, and the integral is carried out over the entire cross section after the volume integral has been reduced by axisymmetry of the parametrized flow to an area integral.

Averaging kernels are most useful when to some extent the averaging kernel is a slightly defocused form of a Dirac delta distribution, so that the inversion only blurs flows slightly and in a localized manner. That is, the value of flow produced by an inversion at a point or element can be interpreted as the average in the neighborhood around it, usually some type of distribution for a weighting function localized around the point or element. In such a case, the inversion can be understood as the flow that would result from blurring the true flow by a low pass filtering operation. The averaging kernels were quite delocalized and irregular in Triana et al. [2014], as can be seen by a reproduction of a figure from that study in figure 2.2. And in motivating the choice of damping parameters, chose one particular small region that was less irregular looking, ; it did not take into account the rest of the domain in the analysis. Averaging kernels are more useful when the coverage of the domain is more uniform, yielding a measure of defocus that damping

induces. Using one location that is less defocused is perhaps, at best, useful for studying that region in the cavity; though it is not actually sufficient even for studying one region in the cavity either, since that region will not be affected by the inversion’s diffusion into that grid point or tile the region is nominally associated with, but also by diffusion to and from the points contained in that region, possibly from very nonlocal sources. See figure 2.2 and note the features.

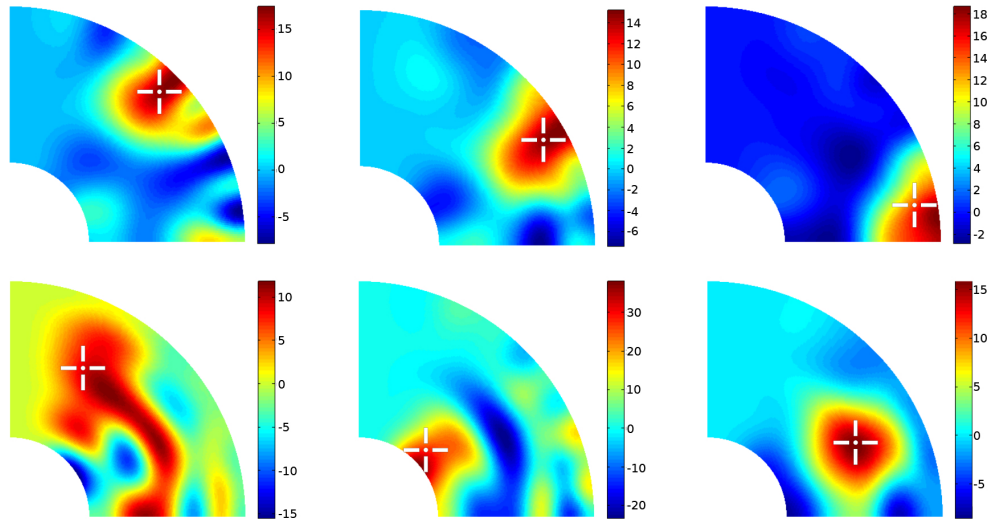


Figure 2.2: Reproduction of a figure from [Triana et al. \[2014\]](#), averaging kernels for several locations used in the inversion. The white cross hairs are showing the location in the domain, which has been broken into thousands of small tiles as basis functions, and the colors are showing the averaging kernel for it. Note the high non-local diffusion, especially for the bottom left sub-figure. The reconstructed rotation rate at the point marked, will be a weighted average of the rotation rates at other locations in the domain, and the weights are given by the coloring of the domain.

The bottom left averaging kernel in figure 2.2 is quite problematic in terms of resolution and exaggerates the difficulty with even defining a width for the distribution associated with the point at the white cross hairs. These observations suggest that using a set of basis functions that are a fine tiling of the domain, such as in Triana et al. [2014] that used many thousands of basis functions tiling the (R, θ) plane in the quadrant it parametrized, is overly ambitious in terms of resolving power. Indeed, the damping has the effect of removing any small-scale features. Assuming the flow is even about $z=0$, and having n data points, one should not expect to be able to have a solution that has more resolution than n controls points in the upper half of a meridional cross section could produce an interpolant for.

The situation is somewhat worse actually. The coverage of the spectrum that a mode set used to perform inversions with has, is altogether different from the coverage of the domain that it can resolve well. Many modes have similar sensitivities. It must be stressed that having n modes spread out in terms of the acoustic spectrum, whose splitting has been measured, is not analogous to having a uniform grid of n control points that in situ measurements of the domain yielded. It is perhaps best understood in terms of the analogy of fitting a curve to a set of data points. Similar sensitivities to flow are analogous to data points being very close to each other, such that they do not so much add spatial information, but, rather, simply reduce the uncertainty at the spatial location that they mutually inform about. Even using a basis that has fewer functions in it than the number of data point, traditional weighted least squares inversion cannot always be performed by an explicit inverse, or at least inverting matrices so ill-conditioned that direct inversion is highly inadvisable, and still requires some form of regularization or truncated singular value decomposition to invert for the model parameters. Many methods try to foster forms of objectivity for choice of damping parameters.

Methods such as minimizing the Dirichlet spread function or the traditional Backus and Gilbert approach of optimally localized averages are popular choices for regularization. They actually try to choose the damping parameters so as to minimize the diffusion/blurring caused by inversion in an ill-posed inverse problem. Though these were not used in Triana et al. [2014], since

they were recommended as an improvement, and are commonly used in both deep earth seismic tomography as well as helioseismology, they warrant comment. Averaging Kernels as depicted in figure 2.2 would normally dissuade one from exploring that option, however the depicted averaging kernels were for parameters chosen to fit the anemometer rather than what had the best optimally localized averages. If a resolution and damping parameter combination is chosen to allow a fit along the anemometers, and that flow is not well resolvable with the data and mode choice, it is to be expected that the averaging kernels would look bizarre. For that reason and other matters to be discussed, the approach seemed like a possibly viable option, especially if the expectation of resolution were decreased and a less fine basis were used.

The Backus and Gilbert approach essentially tries to localize diffusion to each region of the cavity during inversion, using a basis that tiles the domain with small localized functions such as a Cartesian or spherical grid. The Dirichlet approach tries a similar method, but only penalizes the diffusion itself, and does not weight differently diffusion between distant regions and diffusion between neighboring regions. As such, the Dirichlet approach tends to preserve smaller scale features better, but as a result also produces artifacts, such as overshoot. Both methods have noble goals. Unfortunately, though they proceed by optimizing each respective property just described, with small amounts of data and domain coverage there is a wide chasm between doing something optimally and doing something well. Also, they are not without a certain amount of subjectivity.

There is little merit in preventing defocus in many regions in the cavity. For instance, the region that the averaging kernel selected in [Triana et al. \[2014\]](#) as motivation for its inversion, is not one where you would expect localized variations in flow. Even if that averaging kernel had ended up lifting the ambiguity of the choice in damping parameters, it would have done so at the expense of the regions in the cavity where there are possibly localized variations in flow. Such a region was examined in that study, and not used due to how nonlocalized the diffusion was.

If the inversion is carried out on a 2D slice and assumes axisymmetry, then to weight each volume element of the cavity equally requires weighting the damping functions by the cylindrical

radius; the integrals are done on a 2D slice and the true domain is the volume of revolution obtained from it: $dV = 2\pi r dA$. As a result, the trade-off in defocus optimization by volume fraction is biased toward regions of the cavity where there will be less variation; there is no reason to prevent blurring of something that is already relatively homogenized. Choosing a weighting function then that is optimal is difficult if features present in the inversions are to be deemed recovered features rather than enforced features. Some approaches to Backus and Gilbert also impose additional constraint equations that try to enforce conservation of the reconstructed variable. That is, if a basis function is diffused by the resolution matrix, that diffusion should be conservative in some manner. The difficulty with SCF though, is that the rotation is not a conserved quantity. It is tempting perhaps to try and enforce some type of conservation of angular momentum, but as the number of choices increases in the inversion, the solution the Backus and Gilbert approach provides becomes less objective. Many other disciplines have the benefit of heuristically adapting the tunable parameters, and such methods flourish.

[Triana et al. \[2014\]](#) also tried to show consistency with the error magnification operator. An error magnification operator essentially gauges a similar idea for the data as the averaging kernels do for the model parameters. It gauges whether the inversion process inflates errors. An inversion operator that overfits the data given the data uncertainties, will have an error magnification less than 1, and an inversion that does not predict the flow within data uncertainties will have an error magnification greater than 1; on average. Error magnification operators though, are more complex when the errors are not invariant from data measurement to data measurement.

[Triana et al. \[2014\]](#) simplified the analysis by assumed uniform errors and defended the choice by asserting that the errors were all roughly equal, which was not the case nor was that assumption that actually needed to be approximately true in order to make the mathematical manipulation made. To factor out the error magnification operator from a weighted sum, the work claimed that the errors in each splitting were all roughly equal; in which case an operator that varied with each component of the sum could be moved outside the sum. They actually ranged between 2 and 35 and were on the order of 10% often. The factorization actually requires not

the errors to be all roughly equal, but for the square of the errors to be roughly equal, i.e. 4 to be roughly 1225, which is clearly not the case in that context. The assumption may not be so severe in its effect though, since [Triana et al. \[2014\]](#) used composite data from different rotation rates normalizing by the inner sphere. As such, its error weights that stemmed from standard deviations are actually conflating the standard deviation with some form of standard error of the mean possibly. If the inversion is for the mean state of flow composited, the uncertainty is much smaller than what was used; treating them as standard deviations implicitly asserts that the same thing was being sampled unbiased and the difference was due to random errors. It is not clear to this author what the benefit is of using composite data from different rotation rates. It should be noted though, that average error magnification is perhaps not a good metric, especially when there is modeling uncertainty due to neglecting the shaft/axle. Many modes are often quite easy to fit very well, in terms of their splittings measured, by a plethora of qualitatively different solutions whose differences only contribute negligibly to the overall misfit, whereas some modes are quite hard to fit simultaneously, and produce larger errors. Error magnification being 1 on average is not only somewhat arbitrary, but does not assess the distribution of misfits.

Similar issues relate to the "semi-spectral" method employed in [Triana et al. \[2014\]](#) as well. In the "semi-spectral" method employed in [Triana et al. \[2014\]](#), the damping parameters chosen were justified as noting the parameters chosen "obtain a model that provides a good fit to the measured mode splittings"; but in that type of inversion, there should be an increase the goodness of fit as the tunable regularization parameters are decreased. Fitting the data adequately is insufficient justification. Changing the damping parameters even slightly in a method such as this with few modes, can produce very large differences in the recovered profiles, especially inside or near the tangent cylinder. There are no unambiguous criteria for how to choose these parameters presented. Subjective inversion parameter choices are not ideal, especially when the test case is one for which the profile is reasonably well known as in this case, or anemometer profiles exist. The most obvious question, is if the parameters in the inversion were chosen subjectively, the anemometer profile was used to select the damping parameters, then why doesn't it fit much

better along the anemometer profiles? There seems to be some possible causes.

The splittings presented graphically in [Triana et al. \[2014\]](#) as a function of rotation rate of the inner sphere, upon my examination were not representative of the rest of the splitting data. There are significant deviations from linearity that cannot be readily explained by a less precise or changing motor rotation rate variability, which is visible in the acoustic spectrum. Even excluding the lower rotation rate data, the higher rotation rate splittings do not yield a $(\Omega_i, \delta f)$ curve that approximately goes through the origin, even with creative approaches to data weighting based on the listed uncertainties. That is to be expected if the flow is changing qualitatively. Splitting from the $m=0$ mode is to be expected due to the shaft temperature drift or poloidal flow. An extrapolated inferred splitting of the $+|m_s|$ from the $-|m_s|$ mode at zero rotation rate, the quantity contained in the data set examined, for m nonzero, is not as easily interpretable, though it would have been easy to verify directly. [Triana et al. \[2014\]](#) explains this by noting the shell is not perfectly spherical, but slightly prolate. With fluid at rest, though it is quite obvious that $+|m_s|$ should not split from $-|m_s|$ due to asphericities that are axisymmetric about the shaft since they satisfy the same exact PDE, it is perhaps not as obvious that asphericities that are not axisymmetric cannot do it either. Just as in the perfectly spherical case, it is expected that the $+|m_s|$ and $-|m_s|$ pair should be time reversals of each other. Though it cannot be said that they spin in opposite directions exactly due to the non-ideal geometry, they should still evolve as mirror images with respect to each other with respect to the time axis, and hence have the same observed frequency. The only thing that seems a plausible explanation for them being split at rest would be a body force placed on the system, such as the Earth's Coriolis force. Gravity and centrifugal effects are too weak in this regime to produce the splitting. Perhaps some other factor involving the mechanical device that spun the shaft is not included in the model?

The simplest explanation, assuming splitting was not measured between mismatched modes, is that the flow is changing, and despite being linear about some state, is not linear about the fluid being at rest. The only other possibility is that the splitting was measured between modes with different values of $|m_s|$, which would be offset at zero by the distance between rest frequencies;

that seems unlikely given the description of the method used. Though perturbation theory can be made to work by linearizing about another state than the fluid at rest, the kernels used for inversion were those about the fluid at rest. It is not likely that poloidal flow components caused the shift, but even if they had, the linearity about the higher rotation rate would still not resolve the issue and poloidal related kernels would need used. Asphericities may have diverted flow into the (r,z) directions, but that would only affect center frequencies appreciably, not splitting unless the poloidal flow was so vigorous as to distort the mode shape; that seems unlikely.

The forward problem of perturbation theory does not require linearity in the inner sphere rotation rate. It only requires the splittings are linear in the mathematical scaling of the flow from some reference state. The method used in [Triana et al. \[2014\]](#) required more than the first order perturbation theory regime, it required the flow be linear with respect to the inner sphere's rotation rate, else the data at different rates could not be composite by normalizing the splittings by the inner sphere rotation rate. The kernels used implied that linearity is the form that mandates that zero splitting occurs at rest, with no affine shift corresponding to an offset at zero rotation rate of the inner sphere. The inversion procedures ignored the shifts and only used the slopes. To be clear, it is not just ignoring the offset due to splitting from the $m_s = 0$ modes as a result of the axle, but also ignoring the offset of the trend in splitting between $+|m_s|$ and $-|m_s|$ at 0 rotation rate of the inner sphere, as discussed below.

Regardless of whether the flow actually scaled with inner rotation rate, it is not clear what is to be gained from using multiple rotation rates to perform an inversion, and the variation in the data suggests different rotation rates would yield a substantially different answer when used individually.

In summary, it is not clear to this author that the data and anemometer do actually support the forward problem being established in [Triana et al. \[2014\]](#); at least not established in a manner that would allow splittings measured at different rotation rates to be composite as they were. Furthermore, since data was not acquired for the low rotation rates on many modes, which means that it is not possible to track their splittings back to the zero rotation rate to ascertain if the

linear relationship between inner rotation rate and splitting was robust. The intercept on many was several Hz. $(n,l,m)=(0,4,1)$ had an intercept of 3.55 Hz with an error estimate of 0.18 Hz, but at most climbed to a splitting of 9.46 Hz. Refer to section 3.5 for a discussion of (n,l,m) . Many had intercepts 1, 2, and 3 Hz as intercepts. $(0,13,5)$ had an intercept of over 8 Hz with an uncertainty of less than 1 Hz. Using composite splitting data then, means the flow goes to rest at 0 Hz rotation, yet there is a body force on the fluid splitting the modes possibly. It is not clear such offsetting affects could be large enough to cause the observed discrepancies.

2.2 Contrast with this Work

The Experimental setup for which most of of the acoustic data used in this thesis uses has a much larger shaft in terms of cylindrical radius, though has much smaller deviations from spherical symmetry otherwise. If the offsets in the linear trends in splitting were somehow due to lack of axisymmetry, they should not be expected for the 60cm setup. Such geometry related concerns support finite element methods over approximations of the geometry as being spherical, as acknowledged and recommended in [Triana et al. \[2014\]](#).

The benefits of FEM are more than matching predicted frequencies of the modes of the stationary medium and preventing distortion to the inversions. They also improve the forward model's linearity. Even very small perturbations to linear systems can require higher order corrections when too many idealizations are used in the modeling. For instance, no matter how accurate the first order correction to the spectrum can be predicted for a rotating sphere of fluid, if the actual geometry is elliptical, then not only would one have to add a correction for ellipticity, but if severe enough, also add a second order correction. The second order correction to the rotational splittings taking into account the coupling between the rotational affects and the affects of ellipticity; the first order correction due to rotation does not make a good linear forward model, since it was not computed in a geometry that well approximates the experimental setup.

The microphone configuration used in [Triana et al. \[2014\]](#) is far superior to the setup in the 60cm setup though. It had 4 microphones equally spaced in the azimuthal direction, which

allowed a much more robust array method to assess the magnitude of the azimuthal wave number $|m_s|$. The measured spectra were also made using a loud chirp, and the audio files are relatively clean, unlike the 60-cm data.

When only the inner sphere is rotating, one can assume a fluid rotation profile that is sign invariant, since rotating the inner sphere in one direction presumably does not produce rotation in the opposite direction of the fluid, at least on larger length scales when time averaged. The Kernels have a single sign across the domain, and hence the splittings should all have uniform sign. That is not necessarily true in a rotating frame where the acoustics are recorded. For flows near uniform rotation for instance, the splittings are more so dominated by Coriolis forces rather than advection, when measured in the rotating frame where the fluid is nearly at rest throughout the bulk of the cavity.

The largest difficulty with the 60cm setup, compared to the 30cm setup in [Triana et al. \[2014\]](#), is that the 60cm data has no empirical validation for the velocity fields inside. The data has no traditional velocimetry measurements to assess the accuracy of inversions are available. That is not altogether different from the situation in deep Earth seismology or Helioseismology, but given the relatively accessible nature of the 60cm setup, it is unfortunate. The difficulties with getting direct measurements of velocity is actually a motivation for this study. The developed methods are in response to that difficulties. That difficulty coupled with the small size of the data sets, has motivated a considerable amount of conservativeness to the approach, forsaking many nuances that could possibly be teased out of the data, in favor of producing the most reliable and robust results. In chapter 8, a modest data set that is available is used, and these types of issues are addressed.

The methods employed in [Triana et al.](#) attempted to utilize the tools of helioseismology and deep earth seismology for laboratory velocimetry, but the methods employed in those field utilize a great number more modes and observations and use prior models of the expected structure to linearize from. These reservations expressed regarding [Triana et al. \[2014\]](#) are meant to reflect the difficulties with acoustic inversions of this sort, and motivate other possibilities that are explored

in this thesis. The most obvious solution might appear to be to fit the cavity with an array capable of automating the identification of hundreds of modes. While that sounds quite feasible for studies in air such as this work and [Triana et al. \[2014\]](#), since the actual goal is to be able to adapt the techniques to pre-existing liquid sodium experiments and similar devices, this work follows the mindset of extracting as much information robustly as possible from minimal data in chapter 8. The development of the tools for calculating the forward operator is amenable to any number of modes and many other methods of inversion.

Chapter 3: Mathematical Formulation

The mathematical formulation reduces the general 3D problem to a 2D problem by exploiting the axisymmetric nature of the domain. This allows greater accuracy at a small fraction of the computational cost of performing this operation in 3D. Accurately computing the modes of the stationary media is important since they can be used to compute the first order effects of rotating flows on the spectra.

3.1 Acoustic Pressure Perturbation in Stationary Homogeneous Media

In terms of material displacement, the acoustic Helmholtz equation for sound waves in a stationary homogeneous fluid has the form

$$\begin{aligned}\omega^2 u &= c^2 \Delta u, & x \in V \\ u \cdot n &= 0, & x \in \partial V\end{aligned}\tag{3.1}$$

where u is the material displacement vector, ω is the angular frequency of acoustic oscillation, c is the speed of sound in the cavity, the domain V with boundary ∂V , and n is the unit normal to the boundary. The boundary condition idealizes the boundary as being perfectly rigid and an infinite mechanical impedance contrast. This work focuses on the cases where that is a realistic approximation, and does not include an impedance term or coupling to the elasticity of the bounding material.

By taking the divergence of the above equations, one finds the formulation in terms of pressure perturbation

$$\begin{aligned}
-\omega^2 p &= c^2 \Delta p, & x \in V \\
\partial_n p &= 0, & x \in \partial V
\end{aligned}
\tag{3.2}$$

where p is the perturbation in pressure relative to the background pressure, and ∂_n is the normal derivative at the boundary wall. A pressure formulation of the Helmholtz equation allows the problem to be expressed as a scalar partial differential equation, thereby reducing computational requirements. Inclusion of a boundary term does not seem warranted for experiments in air, but for other applications the inclusion of a boundary term $\frac{\partial p}{\partial n} = \frac{i\rho\omega}{Z}$ may be warranted, where Z is the reciprocal of the field admittance at the boundary. Treating the housing of the fluid as a coupled elastic structure could be warranted in some situations involving liquid sodium and certain types of containers, but is not addressed herein. With the vanishing Neumann boundary conditions the Laplacian has a discrete spectrum on this type of domain.

3.2 Exploiting Axisymmetric Geometry for Computational Efficiency

The geometry of the cavity is exceptionally axisymmetric, and is so modeled. The axisymmetry of the domain enables a partial separability of the Helmholtz equation—in the azimuthal variable. The 3D Helmholtz equation in pressure for each azimuthal number m is mapped to an equivalent elliptic partial differential equation in 2D axisymmetric geometry. This is done by using cylindrical coordinates, and an auxiliary wave function $\psi(r, z)$ satisfying

$$p(r, \phi, z) = \psi(r, z)e^{im\phi} \tag{3.3}$$

Thus for each azimuthal number m_s , $\frac{\partial}{\partial \phi} = im_s$, using units so that c is uniform and unity, the Helmholtz equation reads

$$\begin{aligned}
-\omega^2 \psi &= \Delta_{rz} \psi - \frac{m^2}{r^2} \psi \\
\partial_n \psi &= 0
\end{aligned}
\tag{3.4}$$

This PDE can be interpreted as the pressure profile at $\phi = 0$. Now the problem has been

transformed from being 3D vector valued on a 3D domain, into being scalar valued on a 2D domain. In this study, only values of $m_s = 0, 1, \dots, 5$ were used. The identification of the azimuthal number m_s for a mode is thus performed apriori, and is part of the formulation.

3.3 Variational Form of the Acoustic Helmholtz PDE in Pressure

The computational benefit acquired by the reduction to a scalar PDE on a 2D domain also results in a form that is not a standard wave equation. I next place it in a more standard elliptic form:

$$\begin{aligned} \nabla_{rz} \cdot (r \nabla_{rz} \psi) - \frac{m^2}{r} \psi &= -\omega^2 r \psi \\ \partial_n \psi &= 0, \end{aligned} \tag{3.5}$$

For an admissible test function ζ defined on the domain V , multiplying both sides by ζ and integrating by parts yields

$$\begin{aligned} - \int_A r \nabla_{rz} \psi \cdot \nabla_{rz} \zeta \, dA - \int_A \frac{m^2}{r} \psi \zeta \, dA &= -\omega^2 \int r \psi \zeta \, dA \\ \int_{\partial A} r \partial_n \psi \cdot \zeta \, dA &= 0, \end{aligned} \tag{3.6}$$

where the first integrals are carried on the area cross section A on which this 2D PDE is defined, the last being carried out on ∂A , the boundary of A . The absent boundary term is due to the vanishing Neumann condition $\partial_n \psi = 0$ along the boundary of the domain.

3.4 Discussion of Variational Scalar Formulation

The reduction of the problem to 2D, as done in the previous section, has enormous benefits that are difficult to overstate. Having solved the problem in 3D in Comsol Multiphysics, I found obvious drawbacks worth mentioning.

In 3D the number of elements needed, even when using higher order basis functions, is much larger. Though it is still manageable, many of the tasks involving changing the boundary geometry over a range of values to assess the kind of uncertainties associated with their tolerances

would have taken much longer. Also, it became a chore finding the correct solver to calculate the eigenvalues accurately since not having the separation of the modes by value of $|m_s|$ often produced a spectrum that was nearly degenerate in the sense that modes with different $|m_s|$ had the same frequency, and in the frequency range of interest. Not only does the 2D formulation prevent that in the frequency ranges used herein, but it also makes the identification of the m_s wavenumber automatic, since it is part of the PDE as formulated. It allows rapid visual identification of the mode from looking at the meridional cross section while knowing $|m_s|$. Working in 2D comes with drawbacks though.

First, the formulation in the previous section requires axisymmetry. In the case of 30-cm setup used in [Triana et al. \[2014\]](#), I was never able to fit the stationary mode frequencies as well as for the 60-cm setup even after adding ellipticity to the shells after physical examination, by assuming axisymmetry. Even without ellipticity correction in the formulation, the errors were never larger than 1% and usually much less. If a mode frequency is at 4kHz though, 1% amounts to an absolute error of 40 Hz. In the midst of a cluttered spectrum of mode frequencies that can make identification difficult. Such absolute errors would be even more problematic for a setup like the 60cm setup where there is no array configuration to determine $|m_s|$ by cross correlation of microphones at different azimuths; they are 90 degrees apart in terms of azimuth in the 60-cm setup.

3.5 Modal Nomenclature

The altered geometry of the cavity is not so severe as to require abandoning the traditional wave numbers n , l , and m to characterize the modes, for the spatial wavelengths of the lobes used in this study at least. Each mode will be identified by a triple (n,l,m) . For very high frequencies there could arise ambiguity with using this notation and the standard interpretation.

Briefly, the overtone number “ n will represent the number of spherical nodal curves, a contour of nodal points for each spherical ray. Examples are depicted in [figure 3.1](#).

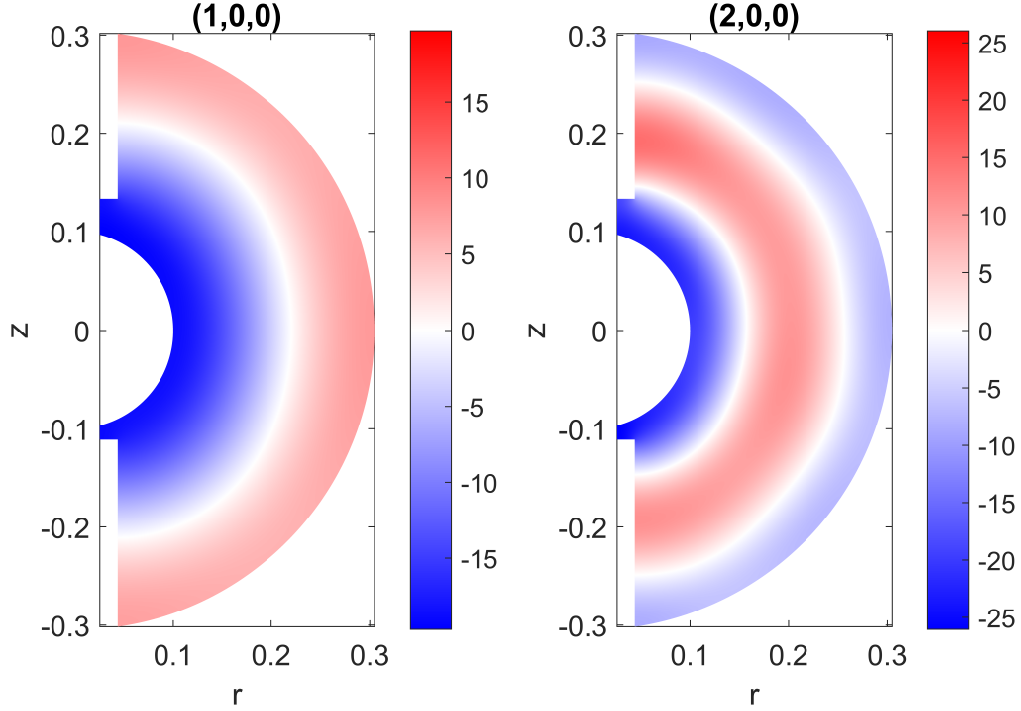


Figure 3.1: Meridional cross section of pressure modes $(1,0,0)$ and $(2,0,0)$. The color represents the relative amplitude. The nodal curves in white.

The degree l and order m_s are analogous to the wavenumbers appearing in spherical harmonics. $|m_s|$ is the number of the surface nodes that are longitudinal. $l - |m|$ then is the number of nodal curves emanating from the inner core to the outer core in the 2D meridional cross section the reduced wave equation is solved on. Throughout, I use the nodal curve counting convention. This is also the motivation for letting n range from 0, since it signifies the number of nodal curves being counted; rather than n starting at 1 as many conventions prefer. Once a lobe of the spherical annulus modes is of similar size as the deviations in the cavity from being a spherical annulus, ambiguities with naming can arise, but since those modes are not used in this study, the matter will be addressed here no further. See figures 3.2 and 3.3 for simple examples of the counting

principle. When identifying modes visually on the meridional cross section, $|m_s|$ is known based on how the PDE is solved, and so the nodal curves can be counted, and n and $l - |m_s|$ can be inferred. Since $|m_s|$ is known, l is then inferred. It should be noted that the naming convention in no way affects the science, only how the modes are named. Only really does the value of m matter, which comes from the PDE and is unambiguous.

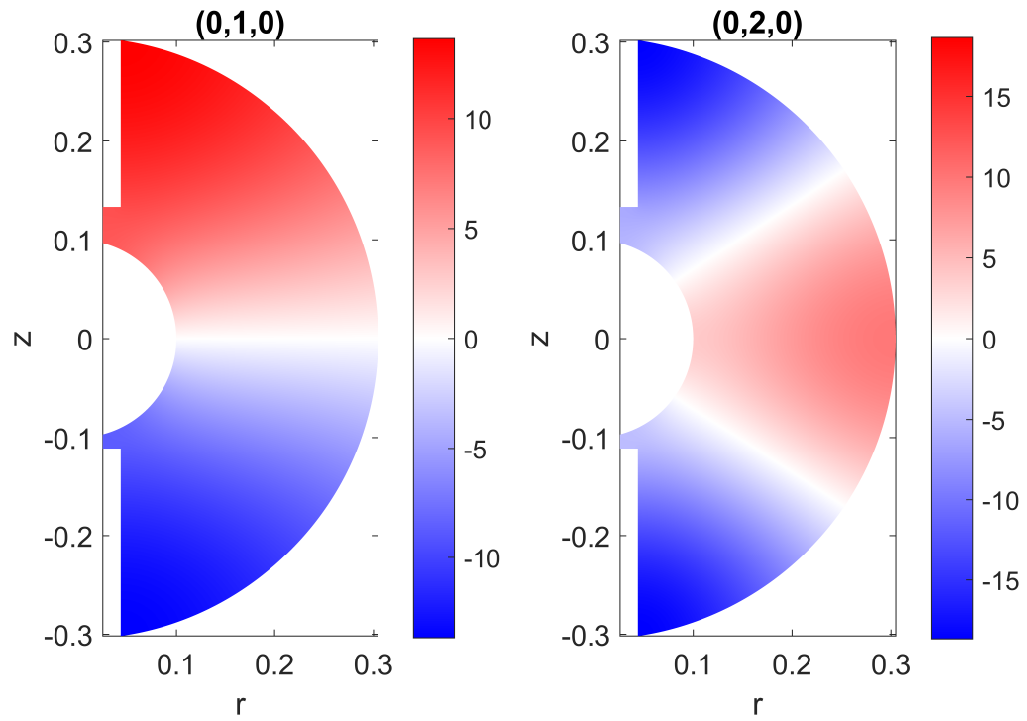


Figure 3.2: Meridional cross section of pressure modes $(0,1,0)$ and $(0,2,0)$. The color represents the relative amplitude. The nodal curves in white.

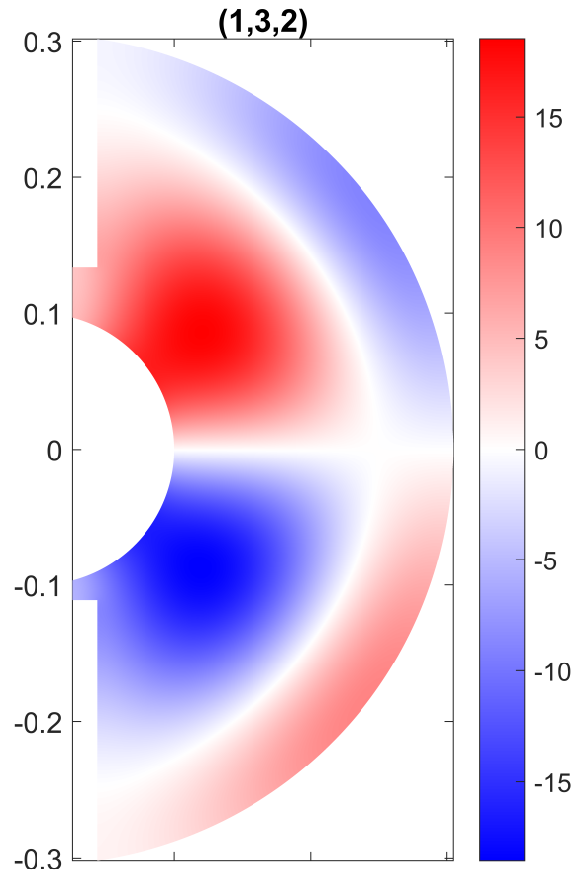


Figure 3.3: Meridional cross section of pressure mode $(1,3,2)$. The color represents the relative amplitude. The nodal curves in white. Since $m=2$ is known from how the PDE is solved, the nodal curves can be counted. See that $n=1$, and $l - |m_s| = 1$, and so $l = 3$. No inconsistencies or ambiguities result from adopting this naming convention in the altered geometry within the frequency range and small wavenumbers used in this study.

Chapter 4: Numerical Formulation

4.1 Finite Element Formulation

The flexibility of the Finite Element Method (FEM) to accommodate irregular geometries, and allow for future refinements to the geometric model of the cavity, make it ideal for simulating acoustic waves in experimental setups. The more precise the modeling of the geometry, the more accurate the center frequencies will be predicted, and the easier it will be to identify modes. This is crucial when the sensor array is limited. More importantly, the presence of altered geometries within or near the tangent cylinder—where arguably the more interesting variations in flow might be observed, the more accurately inversions will infer the flow in those regions by using FEM. The variational formulation does not require uniform soundspeed. However, soundspeed variation is not utilized in this study since not only are the spectra observed consistent with a uniform soundspeed, but also significant soundspeed variations are not expected at the velocities and thermal behaviors present in the experiments.

I use a piecewise triangular mesh sufficiently fine to allow an accurate boundary and convergence in the solutions, consisting of over one hundred thousand triangles. The particular meshing algorithm I employ is based on the methodology set forth in [Persson and Strang \[2004\]](#), with minor modifications. I set a minimal bound on the regularity of the mesh and mandate a triangle quality greater than 0.75 for every triangle, with the triangle quality metric given by

$$\mu(T) = \frac{4A_T\sqrt{3}}{h_1^2 + h_2^2 + h_3^2} \quad (4.1)$$

where h_1 , h_2 and h_3 are the side lengths of the triangle T , and A_T is the triangle area. More than

80% of the triangles have a μ value greater than 0.99 though; the metric equals one when the edge lengths are all equal. I first create a coarser mesh, then refine it twice by way of breaking every triangle into 4 subtriangles via placing new vertices between edge midpoints of the original triangle and connecting them. The large initial mesh size prior to refinement is chosen so as to ensure when the nodes along the boundary of the domain are moved to the boundary specified by the descriptive geometry after subdivision, the regularity of the triangles only changes negligibly. That is, the refinement process also improves the boundary accuracy while not eroding the regularity of the surrounding triangles.

I use isoparametric elements, where the basis functions and test functions are piecewise linear splines; “tent functions”. Each basis function is unity at a single node, and linearly decays to zero at the neighboring nodes, and is zero outside that neighborhood. Given such a discrete basis $\{\psi_j : j = 1, 2, \dots, N\}$ for the solution space, any solution ψ can be approximated in the form

$$\psi = \sum_{j=1}^N a_j \psi_j \quad (4.2)$$

where the coefficients $a_j : j = 1, 2, \dots, N$ are to be determined that best approximate the solution with respect to the basis $\{\psi_j : j = 1, 2, \dots, N\}$.

Deriving from Eq. 3.6, the stiffness matrix elements are given by

$$K_{jk} = - \int_A r \nabla \psi_j \cdot \nabla \psi_k dA - \int_A \frac{m_s^2}{r} \psi_j \psi_k dA \quad (4.3)$$

Similarly, the mass matrix is given by

$$M_{jk} = \int_A r \psi_j \psi_k dA \quad (4.4)$$

The integrals for the matrix elements for the stiffness matrix are assembled in two parts. The first integral is the same regardless of m_s . For that contribution, a centroid rule for estimating the integrand is used, since the gradients on the piecewise linear elements make the integrands piecewise

constant inside each element using an exact Gauss quadrature rule. For the other integral and the mass matrix, the following scheme has been used: the coefficient functions are interpolated to their centroids on each triangle and moved out of the integrals, and the remaining quadratic integrands $\psi_j\psi_k$ are then integrated by an exact Gauss quadrature rule. The presence of the axle in the model alleviates the singularity in the $\frac{m_s^2}{r}$ factor.

4.2 Solving for the Stationary Modes and Stationary Frequencies

The modes and frequencies of the stationary medium are solved for using sparse Arnoldi iteration [Saad, 1980], carried out with ARPACK [Lehoucq et al., 1998] via interface with Matlab. The assembled finite element matrices are symmetric, so the algorithm used is Implicitly Restarted Lanczos Method (IRLM).

Since a different system is solved for each value of m_s , there is greater spacing between the adjacent modes throughout the low frequency band of the spectra used, even greater since the eigenvalues solved for are actually $-\omega^2$; alleviating any numeric issues associated with near degeneracies. The regularity of the mesh, and the low frequency range being used, means that convergence of the eigenvectors and eigenvalues with respect to triangle density also implies convergence of the solutions; there are no significant effects of round-off for the precision needed; the matrix elements having very similar order of magnitude. The larger source of error, though still quite small, comes from idealizations in the geometric modeling.

The actual experimental setups such as the 60-cm setup contain small deviations from the descriptive geometry used to construct the mesh. The joint of the shaft and outer sphere is not a sharp corner, but a fillet. Furthermore, the shaft has missing pieces, which were estimated in the descriptive geometry from mechanical drawings and photographs, but the actual components contain all additional pieces not modeled. The microphones and speakers also take up space, though not sufficiently large to merit incorporating them into the model. These unmodelled aspects will introduce quite small errors. All else held equal, they are quite insignificant to the inversion methods, but even a 0.25% error at a mode frequency of 2kHz amounts to a 5Hz shift in terms of

absolute frequency, which can make it difficult to identify a mode based on its frequency and the limited knowledge of m_s , especially when the sensor locations are suboptimal.

Near degeneracy or small spectral spacings between modes for the same value of m_s may cause higher order effects to become significant. In the data this work has applied its methods to though so far, clusters of such modes are often difficult to measure the splittings of since the available array techniques on the 60-cm setup do not adequately distinguish them. Thus, all the modes used of the same value of m are distantly spaced in the frequency spectrum, and the issue is circumvented by default.

The (n, l, m_s) identification was performed by viewing a meridional cross section produced by the FEM, and then based on counting nodal curves, as explained in the previous section. All modes in this work were checked visually by examining the pressure pattern on the meridional cross section to ensure there were no mistakes in identifying n or l of the associated multiplet from the FEM solutions. Several automation methods were developed, such as using operators on the FEM solution and inferring the (n, l, m_s) from the eigenvalues, as well as cross correlation with the spherical annulus solution. The methods produced different results for high frequencies, since cross correlation with the spherical annulus modes is inconsistent with the nodal curve naming convention in some instances for high l values for example. Cross correlating iteratively with modes as the shaft is grown from the spherical annulus was infallible at coinciding with the nodal curve interpretation of (n, l, m_s) identification; visual identification was simple enough to not risk incurring an error associated with not checking though.

Table 4.1 shows the results of the FEM for the modes up to 2.5 kHz. It uses a soundspeed of $c = 344 \frac{m}{s}$. Stationary frequency accuracy was high enough using only a single mode for calibration of soundspeed that least squares methods were unnecessary. The actual stationary frequencies are not used in inversions for the regimes applied to in this study, since the stationary frequencies are only needed when the speed of rotation is much higher, and the Helmholtz equation's linearity in $-\omega^2$ must be used rather than linearizing the perturbations $\delta\omega^2$ to perturbations in $\delta\omega$; discussed in chapter 5. Even in the case that perturbations in the square of the angular frequency are prudent

to use, the error incurred by approximating the center frequency is quite small for plausible rotation rates for these types of studies.

n	l	m_s	f (Hz)	n	l	m	f (Hz)	n	l	m_s	f (Hz)
0	1	1	346	0	7	5	1605	1	6	2	2167
0	1	0	365	0	7	0	1695	2	3	0	2172
0	2	1	570	1	4	1	1702	0	10	3	2173
0	2	2	593	2	0	0	1728	1	6	1	2179
0	2	0	612	1	4	2	1734	0	10	4	2181
0	3	1	774	1	4	3	1749	0	10	10	2181
0	3	2	807	1	4	4	1750	0	10	9	2181
0	3	3	809	0	8	1	1760	0	10	8	2181
0	3	0	837	0	8	2	1768	0	10	7	2181
1	0	0	932	2	1	0	1790	0	10	6	2181
0	4	1	970	2	1	1	1791	0	10	5	2181
0	4	2	1009	0	8	3	1795	1	6	3	2198
0	4	3	1014	0	8	4	1798	1	6	4	2203
0	4	4	1014	0	8	8	1798	0	6	6	2203
1	1	1	1045	0	8	7	1798	1	6	5	2203
0	4	0	1056	0	8	6	1798	2	4	1	2281
1	1	0	1071	0	8	5	1798	0	10	0	2308
0	5	1	1165	1	4	0	1847	2	4	2	2313
0	5	2	1204	2	2	1	1898	0	11	2	2321
0	5	3	1213	0	8	0	1908	2	4	3	2329
0	5	4	1214	2	2	2	1922	2	4	4	2330
0	5	5	1214	1	5	1	1938	1	6	0	2348
1	2	1	1233	2	2	0	1940	0	11	3	2359
1	2	2	1263	0	9	2	1949	0	11	1	2361
0	5	0	1270	1	5	2	1957	0	11	4	2371
1	2	0	1313	0	9	1	1964	0	11	11	2372
0	6	1	1361	1	5	3	1979	0	11	10	2372
0	6	2	1395	1	5	4	1981	0	11	9	2372
0	6	3	1409	1	5	5	1981	0	11	8	2372
0	6	4	1410	0	9	3	1985	0	11	7	2372
0	6	6	1410	0	9	4	1990	0	11	5	2372
0	6	5	1410	0	9	9	1990	0	11	6	2372
1	3	1	1461	0	9	8	1990	1	7	2	2375
0	6	0	1483	0	9	7	1990	1	7	1	2404
1	3	2	1500	0	9	6	1990	1	7	3	2411
1	3	3	1507	0	9	5	1990	1	7	4	2419
0	7	1	1560	2	3	1	2060	1	7	7	2419
0	7	2	1583	1	5	0	2083	1	7	6	2419
1	3	0	1587	2	3	2	2099	1	7	5	2419
0	7	3	1603	2	3	3	2105	2	4	0	2452
0	7	4	1605	0	9	0	2124	0	12	2	2508
0	7	7	1605	0	10	2	2135	0	11	0	2520
0	7	6	1605	0	10	1	2155	0	12	3	2543

Table 4.1: FEM calculated frequencies at $c=344$ m/s for the 60-cm setup. As can be seen, the multiplets are split due to the shaft's presence. Values have been rounded to the nearest natural number. The data the methods are applied to is as high as 2.1kHz; the reason for the range presented.

4.3 Discussion of FEM Predictions for Stationary Modes

The shaft lifts the degeneracy of the multiplets, as can be seen from the predictions in table 4.2 . Better inter multiplet agreement occurs for very high frequency modes though since they are less sensitive to the shaft often. However, modes are more affected by the presence of the shaft are the ones that carry the most information on the tangent cylinder’s interior zonal flow, so they are of high utility for reconstructing zonal flow inside the tangent cylinder. Helioseismology for instance, has evolved to use G-modes—modes whose restoring force is gravity—for imaging deeper structure. Pressure modes are quite useful for inferring the azimuthal angular velocity in the sun’s convective zone and to some extent the upper radiative zone, yet have weaker resolution for the deeper interior of the sun and near the poles.

4.4 Solution for a Spherical Annulus

In the absence of a shaft, axle, or other components that present themselves in experimental work, the acoustic Helmholtz equation in a rigid spherical annulus is possible to solve via separation of variables in spherical coordinates. Solving this form of the problem provides a comparison of the frequencies without the shaft or axle to those of the actual setup. Additionally, comparison to my FEM algorithm with altered parameters provides another quality assurance for the numerics.

4.4.1 Modes of the Spherical Annulus

To avoid confusion, in this section the variable r will stand for the spherical radial variable, and U will be used for the radial wavefunction variable. Consider a solution of the form

$$\mathcal{P}(r, \theta, \phi) = U(r) \Theta(\theta) \Phi(\phi) \tag{4.5}$$

where \mathcal{P} is pressure, and has been notated in this way so as to avoid confusion with the Legendre polynomial symbol. The functions Θ and Φ are invariant with respect to the size of the inner

sphere, and they are given by

$$\begin{aligned}\Theta(\theta) &= P_l^{m_s}(\cos \theta) \\ \Phi(\phi) &= e^{im_s\phi}\end{aligned}\tag{4.6}$$

where P are the associated Legendre polynomials, and the product of these azimuthal and polar functions are spherical harmonics $Y_l^m(\theta, \phi) = P_l^m(\cos \theta)e^{im\phi}$. The radial wave functions cannot be found purely analytically though. They can be expressed in terms of spherical Bessel functions, but the boundary conditions require the wavenumbers to be computed numerically, in all but a few specific ratio of radii of the outer boundary to the inner. The solutions are of the form

$$U_{nl}(r) = J_{nl}^{sp}(r) + bN_{nl}^{sp}(r)\tag{4.7}$$

where J^{sp} and N^{sp} are spherical Bessel functions of the first and second kind respectively. These solutions are analytic if k and b are known, but b and k must be calculated numerically for most aspect ratios $\frac{R_o}{R_i}$.

The radial ordinary differential equation in spherical radial variable r is given by

$$\frac{d^2U}{dr^2} + \frac{2}{r} \frac{dU}{dr} - \frac{l(l+1)U}{r^2} = -k^2U\tag{4.8}$$

where l is the degree and k is the wavenumber, the ratio of the acoustic angular frequency to the soundspeed.

4.4.2 Computing the Solution to the Radial Wave Equation

Since the inner core is roughly 1/3 the diameter of the outer, no singularities or near singularities are present in spherical coordinates. For each value of l I solve for the wavenumber k using the boundary condition $\frac{dU}{dr} = 0$ at $r = R_i$ and $r = R_o$. The frequency of the mode then, is the product of the wavenumber and the soundspeed. Each frequency is implicitly a function of l but has no m_s dependence in this geometry. Several methods are employed to check the accuracy, so as to have a very accurate ground truth solution. Both a finite element formulation

and finite difference formulation in 1D are used, being highly accurate since the equations are defined over a 1D interval only. Both the FEM and FDM reduce to eigenvalue problems and are solved using sparse Arnoldi iteration. Visual inspection of the wavefunctions produced, as well as performing a grid search over a neighborhood of k and the inferred b value was performed to ensure high accuracy, by way of the analytic solutions; a simple means of ensuring the very high number of nodes used did not produce any numerical round-off concerns. Both the 1D FEM and 1D FDM were sufficiently accurate that the slight changes in k observed were likely due to numerics associated with the fitting of k and b simultaneously. Error in frequencies on the modes presented here, are estimated to be less than 0.01 Hz in error, much more accurate for most, especially low l values.

The finite element formulation uses the following equivalent form

$$\frac{d}{dr}\left(r^2 \frac{dU}{dr}\right) - l(l+1)U = -k^2 r^2 U \quad (4.9)$$

then proceeds with using piecewise linear splines and exact Gauss quadrature to formulate the stiffness matrices $K_l : l = 0, 1, \dots$ and the mass matrix M . FEM incorporates Neumann boundaries must more naturally, as the variational formulations works by performing integration by parts on the PDE and the normal derivative at the boundary being zero nullifies the contribution of the boundary term. With FDM ghost nodes must be used at least implicitly in how the boundary is handled, which means that to use a few nodes implies handling the length of the last node spacing in a way so as to not incur error. FDM presume the solution goes completely flat at the boundary over the last interval. The two methods produce the same answers at sufficient grid resolution though, and so FEM was adopted.

Finite difference operators were constructed using centered differences and ghost nodes at the boundaries to enforce the boundary conditions. This alleviates fitting the mode to the geometry with both k and b simultaneously. At these low frequencies the accuracy and speed of solving the ODE via iterative eigenvalues problems is exceptional, in either method.

4.5 Comparing Theory and FEM for Spherical Annulus Solution

In table 4.2 I compare the obtained frequencies with those from my finite element code with no axle or shaft; the shaft radius was set to 10^{-6} (m) in order to prevent singularity when evaluating $\frac{-m^2}{r}\psi$. Presented in table 4.2 are the 1D FEM coded values, the 2D FEM values, the relative error of the 2D from the 1D, along with the maximum absolute deviation in Hz that the $m_s \neq 0$ modes deviated from the $m_s = 0$ mode in the 2D finite element solutions. Each multiplet is labeled by the ${}_nS_l$ convention.

Multiplet	f_{1D} (Hz)	f_{2D} (Hz)	$\frac{ f_{2D}-f_{1D} }{f_{1D}}$	$\ f_{2D} - f_m\ _\infty$ (Hz)
${}_0S_1$	356.93	356.93	$1 \cdot 10^{-7}$	0.02
${}_0S_2$	593.70	593.71	$5 \cdot 10^{-6}$	0.05
${}_0S_3$	808.86	808.87	$1 \cdot 10^{-5}$	0.07
${}_1S_0$	931.01	931.02	$1 \cdot 10^{-5}$	NA
${}_0S_4$	1013.76	1013.77	$1 \cdot 10^{-5}$	0.12
${}_1S_1$	1055.18	1055.20	$2 \cdot 10^{-5}$	0.05
${}_0S_5$	1213.50	1213.51	$1 \cdot 10^{-5}$	0.15
${}_1S_2$	1264.20	1264.23	$3 \cdot 10^{-5}$	0.12
${}_0S_6$	1410.21	1410.23	$2 \cdot 10^{-5}$	0.21
${}_1S_3$	1507.12	1507.16	$3 \cdot 10^{-5}$	0.23
${}_0S_7$	1604.90	1604.94	$2 \cdot 10^{-5}$	0.20
${}_2S_0$	1733.86	1733.97	$6 \cdot 10^{-5}$	NA
${}_1S_4$	1749.74	1749.80	$3 \cdot 10^{-5}$	0.32
${}_2S_1$	1797.58	1797.70	$7 \cdot 10^{-5}$	0.79
${}_0S_8$	1798.10	1798.15	$3 \cdot 10^{-5}$	0.06
${}_2S_2$	1922.90	1923.02	$6 \cdot 10^{-5}$	0.10
${}_1S_5$	1981.15	1981.12	$3 \cdot 10^{-5}$	0.09
${}_0S_9$	1990.13	1990.21	$4 \cdot 10^{-5}$	0.08
${}_2S_3$	2104.57	2104.70	$6 \cdot 10^{-5}$	0.08
${}_0S_{10}$	2181.21	2181.32	$5 \cdot 10^{-5}$	0.10
${}_1S_6$	2203.02	2203.13	$5 \cdot 10^{-5}$	0.11
${}_2S_4$	2398.23	2329.96	$6 \cdot 10^{-5}$	0.10
${}_0S_{11}$	2371.50	2371.66	$6 \cdot 10^{-5}$	0.12
${}_1S_7$	2419.03	2419.17	$5 \cdot 10^{-5}$	0.13

Table 4.2: Normal Mode Frequencies computed by FEM in column 3 agrees quite well with the theoretical semi-numerical result in column 2, as seen in the relative errors in column 4. The differences between frequencies of the elements in the multiplets are quite small as well; column 5. The NA values are reflecting that only $m_s = 0$ is possible when $l = 0$. Note: the estimated relative errors are based on the unrounded values.

The errors shown in 4.2 are quite small. The fit with theory is quite good. The near divergent behavior of $\frac{1}{r}$ in the absence of the large shaft is likely to blame for the discrepancy as much as discretization error and other concerns. A finer mesh was not used to compensate for that behavior. The mesh was kept as similar to the one used in the computations with the shaft as possible, in order to make as accurate of a comparison as possible. The modeling uncertainty likely far outweighs error due to discretization. The mesh is denser than needs be for accurate frequency identification, but the same mesh is used for flow parametrization and Kernel calculation, which requires smoother parametrization and numerical differentiation when computing kernels and can introduce a small amount of error as well. If a mesh was used at the minimum resolution level needed to accurately predict the needed frequencies for the 60-cm setup, it would have been far coarser and more disagreement would have occurred within the multiplets. The mesh was also used for the flow parametrization though, and for numerical integration associated with computing the sensitivity kernels and forward operator discussed in the next chapter. A much finer mesh was used than the acoustics mandated, and so there was very high accuracy. The resolution level would perhaps be inadvisable in terms of efficiency for an analogous problem in 3D that could not be reduced via axisymmetry or to a scalar potential such as pressure perturbation.

Chapter 5: Linear Theory of Acoustic Splitting for Rotating Flows with Shear

5.1 Wave Equation inside a Vortex

The homogeneous medium wave equation in the presence of a material velocity field within the medium is given by

$$\ddot{\mathbf{u}} = \Delta \mathbf{u} + 2(\mathbf{v}_0 \cdot \nabla) \dot{\mathbf{u}}, \quad (5.1)$$

where again, units have been chosen so that the soundspeed is set to unity. This leads to the perturbed Helmholtz equation:

$$-\omega^2 \mathbf{u} = \Delta \mathbf{u} + 2i\omega(\mathbf{v}_0 \cdot \nabla) \mathbf{u}, \quad (5.2)$$

and the resulting first order correction in ω :

$$\delta\omega = \frac{-i \int_V \mathbf{u}^\dagger (\mathbf{v}_0 \cdot \nabla) \mathbf{u} dV}{\int_V |\mathbf{u}|^2 dV}. \quad (5.3)$$

These expressions do not have a density distribution or soundspeed term weighting the integrands, which would be required if the variations induced by the flow were significant relative to the resolution of the inversion being sought.

If v_0 is azimuthal, i.e. purely directed in the cylindrical coordinate $\hat{\phi}$, then

$$\mathbf{v}_0(\mathbf{r}, \mathbf{z}) = r \Omega(r, z) \hat{\phi} \quad (5.4)$$

and thus for a mode with spin m_s in an azimuthal flow

$$(\mathbf{v}_0 \cdot \nabla)\mathbf{u} = im_s\Omega \mathbf{u} + \Omega \mathbf{z} \times \mathbf{u} \quad (5.5)$$

The first term is associated with the affect of advection, and the second term is associated with the affect of Coriolis forces. In the case of uniform rotation, for instance, advection makes the fluid medium rotate such as to increase the frequency of the prograde mode spinning about the same axis, and decrease the frequency of the mode spinning retrograde to the fluid motion. In the this work I will use the convention of the $-|m_s|$ mode spinning prograde and the $+|m_s|$ spinning retrograde. This is because the frequencies of the modes are considered to be positive, the distinction between $\pm\omega$ not being made. And so, if the azimuthal envelope $e^{im_s\phi}$ is modulated by $e^{i\omega t}$, then the combined effect is a spinning envelope given by $e^{i(\omega t + m_s\phi)}$. The pattern of the mode can be seen to spin by tracking the phase value α by $\omega t + m_s\phi = \alpha$, i.e., $\phi(t) = \alpha - \omega t$. The pattern is spinning backwards at an angular rate of ω radians per second. Inserting Eq. 5.5 into Eq. 5.2 also produces a sum of two self adjoint operators like the Laplacian; proving that they do not destroy the discrete eigenstate structure necessitating a singular perturbation theory interpretation is beyond the scope of this work, though insofar as one assumes the problem can be discretized, i.e. written as a matrix formulation, it is a trivality and follows from the spectral theorem.

Next, I modify these canonical expressions to be expressed in the derived pressure mode cross sections that I have calculated via FEM.

Consider the auxillary function $\eta(r, z)$ given in terms of the auxillary wave function ψ representing the acoustic pressure perturbation at $\phi = 0$.

$$\eta(r, z) := r\left(\frac{\partial\psi}{\partial r}\right)^2 + \frac{m^2}{r}\psi^2 + r\left(\frac{\partial\psi}{\partial z}\right)^2 \quad (5.6)$$

η simplifies the expressions for the corrections. The calculation for the first order correction to angular velocity reduces to

$$\delta\omega = -m \frac{\int_A \Omega(r, z) \eta(r, z) dA}{\int_A \eta(r, z) dA} + m \frac{\int_A \Omega(r, z) \frac{\partial |\psi|^2}{\partial r} dA}{\int_A \eta(r, z) dA} \quad (5.7)$$

where A is the cross section at $\phi = 0$. I derived this from applying first order perturbation formula for the eigenvalue $-\omega^2$ for a normalized material displacement mode solving the Helmholtz equation, and then using the approximation

$$-\omega^2 \mathbf{u} = -\frac{1}{\rho_o} \nabla p \quad (5.8)$$

where the variable p is the acoustic pressure perturbation such that $P = P_o + p$. The expression is then fully linearized the by the Taylor approximation of

$$\omega = \sqrt{\omega_o^2 + \delta\omega^2} \quad (5.9)$$

which implies that

$$\delta\omega = \sqrt{\omega_o^2 + \delta\omega^2} - \omega_o \quad (5.10)$$

which yields

$$\delta\omega = \omega_o \left(\sqrt{1 + \frac{\delta\omega^2}{\omega_o^2}} - 1 \right) \quad (5.11)$$

expanding

$$\delta\omega \approx \omega_o \left(1 + \frac{1}{2} \frac{\delta\omega^2}{\omega_o^2} - 1 \right) \quad (5.12)$$

hence

$$\delta\omega \approx \frac{\delta\omega^2}{2\omega_o} \quad (5.13)$$

What is measured is $\delta\omega$, or δf . $\delta\omega^2 = (\omega + \delta)^2 - \omega^2$. Using the approximation of Eq. 5.13 introduces an error of approximately $\frac{(\delta\omega^2)^2}{8\omega_o^3}$. For the data used in this study with the highest rotation rates and highest splittings, the error is less than 1%, on average 0.25%, and for the modest rotation rates used in inversions in chapter 8 even lower. No significant improvement can be made by trying to incorporate the finer correction by adjusting based on center frequency,

especially with the uncertainty associated with measuring the center frequency or the temperature acoustically.

As can be seen from the frequency correction expressions, there is no soundspeed variable or material parameter such as density or bulk modulus. This implies that to first order the temperature drifts of the system that change the soundspeed inside the cavity, will only shift the center frequencies and not alter the magnitude of the splitting about the center frequency. In the first order regime, measuring the splitting between $+|m_s|$ and $-|m_s|$ will not require drift correction. For the regimes of flow being studied, and the magnitudes of splitting observed, the small fraction of a percent the perturbation formulation in terms of $-\omega^2$ would offer would be offset by the error incurred due to ω_o center frequencies requiring drift correction, and possibly higher order corrections. It can also be seen that $m_s = 0$ modes do not split due to azimuthal flow, to first order. The spin of the mode, is purely a spin of the pressure relative amplitudes, not a spin of the material medium, and so the axisymmetric $m_s = 0$ modes do not split by virtue of remaining invariant along any azimuth. This assumes a relatively uniform temperature and pressure inside the cavity.

The integrals in Eq. 5.7 can be viewed as linear operators on the rotational flow, with kernels defined by

$$\kappa(r, z) = -m_s \frac{\eta(r, z)}{\int_A \eta(r, z) dA} + m_s \frac{\frac{\partial |\psi|^2}{\partial r}}{\int_A \eta(r, z) dA} \quad (5.14)$$

The shift in angular frequency of a mode ψ with spin m_s in the presence of an azimuthal flow having rotational profile $\Omega(r, z)$ is given by

$$\delta\omega = \int_A \kappa(r, z) \Omega(r, z) dA \quad (5.15)$$

The kernels κ_{nlm_s} are computed numerically by evaluating the expressions at triangle centers, components of the gradient derived from the gradient of the tangent plane of the piecewise linear solution over each triangle in the mesh. Testing of theory was done in several stages using chirp based data. Uniform rotation, where the fluid is spun up to rotating like a rigid body was used.

Analysis for differential rotation and the presence of shear is carried out for the actual data used in inversions by way of the $m_s = 0$ modes in chapter 8.

5.2 Uniform Rotation

Uniform rotation of the fluid inside the cavity is often called "solid body rotation", since the material moves analogous to a rigid object under rotation. If the container is spun up slowly in the appropriate way, both inner and outer boundaries rotating in unison, approximately uniform fluid rotation results. Using data collected in Adams [2016] I test my software against the results. The data was collected in the rotating frame, meaning that it is nominally at rest in that frame. Relative to the rotating frame, the equations simplify to

$$-\omega^2 \mathbf{u} = \Delta \mathbf{u} - 2i\omega \Omega \hat{\mathbf{z}} \times \mathbf{u} \quad (5.16)$$

Only the Coriolis effect contributes since the fluid is not advecting relative to the reference frame.

Table 5.1 shows the results of theory versus observed shifts from the center frequencies.

n	l	m	f (Hz) FEM	f (Hz) observed	% error
0	1	1	346.0	346.0	Calibrated
0	2	1	570.2	569.5	0.12
0	2	2	593.0	594.5	0.25
0	3	2	806.7	807.5	0.10
0	3	3	808.8	810.5	0.21
0	4	2	1008.9	1010.0	0.11
0	4	3	1013.6	1015.0	0.14
0	4	4	1013.7	1015.5	0.18
1	1	1	1045.4	1048.0	0.25

Table 5.1: A comparison of my FEM predictions with observed frequencies in the stationary medium by targeted chirp, and errors are a small fraction of 1%. The error is likely even slightly lower, since the soundspeed was calibrated using the lowest frequency, rather than the highest, or some least squares fit to all. The measured acoustic data in the column for observed frequency were performed by Matthew Adams.

Δ_1 FEM	$\frac{\Delta_5}{5}$ observed	error %	$\frac{\Delta_{10}}{10}$ observed	error %	$\frac{\Delta_{15}}{15}$	error%
0.660	0.660	0.072	0.664	0.602	-	-
0.214	0.213	0.346	0.212	0.580	0.205	4.089
0.728	0.730	0.249	0.725	0.438	0.707	2.956
0.459	0.455	0.792	0.460	0.298	0.462	0.662
0.704	0.700	0.580	0.700	0.580	0.708	0.604
0.315	0.310	1.438	0.317	0.946	0.315	0.151
0.502	0.460	8.366	0.503	0.100	0.500	0.398
0.670	0.650	2.995	0.673	0.363	0.687	2.477
0.135	0.155	15.164	0.150	11.449	0.132	2.173

Table 5.2: Comparison of the same mode set from the table 5.1 , at various rotation rates where the inner and outer boundaries are spinning together, spun up to achieve uniform rotation of the fluid. The Δ values are the absolute shift of the modes from the center frequency in Hz. The denominators on the observation Δ values are the rate of medium's rotation in Hz. The leftmost column represents the expected shift from center frequency due to 1 Hz uniform fluid rotation. The percent errors do not take any account of the observational uncertainties or modeling uncertainties. The missing data in the first row is because measurement could not be reliably made due to that portion of the spectrum at the high rotation rate of the experiment being very noisy. Under the presumption that there should be no splitting at 0 Hz then, the linearity implies that the ratio of the splitting to rotation rate should remain invariant during experiments and equal to the finite element prediction. Note: This table does not give signs to the shifts, since signs were not measured for the data, only the magnitude of the splitting was measured. Acoustic data measurements made by Matthew Adams.

Table ?? shows a comparison of the linear theory of splitting with observed splittings from the center frequency. The majority of measurements are within 1% error. The last row of data corresponding to mode (1,1,1) is significantly higher in terms of percent error, though in terms of absolute deviation is still quite small. Frequency resolution in the acquired data is comparable to the amount of splitting being measured in those cases, and are not evidence of any theoretical issue. Mode (1,1,1) at $\Omega = 10$ Hz for instance has a shift of 1.50 Hz observed compared to FEM prediction of 1.35 Hz. This translates to an error 11.5%. The small absolute error though, can be explained by the observational uncertainty. Reading the splittings off the graph in such conditions carries an uncertainty of roughly 0.4 Hz, translating to 0.2 Hz shift from center frequency. Errors are also relatively high for the rotation rate of 15 Hz. Spinning the experiment at 15 Hz as opposed to 10 Hz or lower produces significantly more noise, contaminating the spectrum.

5.3 Soundspeed Uniformity

The previous section assumed the soundspeed was uniform. Thermal stratification due to the mechanics of the apparatus or in conjunction with velocity induced compression was not incorporated in this study. The velocities were sufficiently low, $|r\Omega|^2 \ll c_{air}^2$, so the kernels did not require weighting functions related to the soundspeed distribution.

Assuming incompressibility of liquid sodium, the deviations from unity weighting are at most a small fraction of one percent for the experimental conditions analyzed here, much less for the bulk of the cavity. The sodium experiment is 1.5 meters in radius and has a max outer rotation rate of 4Hz, and the soundspeed of sodium is roughly 2.5 km/s.

Higher compressibility of air compared to sodium somewhat complicates matters, but, to first order, the effects on soundspeed should be somewhat smaller for air, since the slight pressure increase would induce slight density increase thereby preventing the soundspeed increase partially. Corrections to the soundspeed distribution can be made using only the $m_s = 0$ modes and a traditional approach as used in seismology to infer the soundspeed profiles at long wavelengths: the soundspeed squared can be separated into a background model and a perturbation

quite accurately for small variations, and the Laplacian's linearity can be employed to produce a perturbation expression for use in a linear inversion. Given the uncertainties present in the data, it is not possible to do so without conflating the effect with the noise and observational and modelling uncertainties. As such, the matter has not been pursued herein.

Temperature variations were also considered. The uniform rotation of the air presumably produces less mixing than in the data later used for inversions which were collected during differential rotation. Supporting that there were no significant effects due to that were occurring, the $m_s = 0$ modes were monitored. For the data used in chapter 8, 10 $m=0$ modes were monitored across different rotation rates of the inner sphere, between -4 Hz and -40 Hz, and the $m=0$ mode changes in frequency could be explained by a uniform temperature increase in the cavity. One caveat is that slightly more elevated temperatures in regions with low acoustic sensitivity to flow would not affect acoustics appreciably. Discussed further in chapter 9.

Chapter 6: Relating Fluid Rotation to Acoustics

6.1 Flow Characteristics

In this work mean fluid flow has been approximated as being purely azimuthal in the laboratory frame of reference insofar as acoustic splittings are concerned, and flows where that approximation is valid are the interest herein. That is, centrifugal forces and poloidal flows are not strong enough to sufficiently distort the mode shapes thereby influencing the splitting between modes with equal and opposite azimuthal order m_s . Poloidal flows can shift the center frequencies though, and could be one of the explanations for the slight movements of spectral peaks seen in the data depicted and discussed in chapter 8.

Acoustical modes sample the medium continuously with time, and so time varying flows distort the idealized steady state oscillation of a mode. If the fluctuations are sufficiently small, spectra acquired from sufficient time integration produce spectra with minimal defocussing of mode peaks. The technique images the mean flow, where the duration over which the mean is taken is the time interval over which the acoustic spectra are estimated. This type of mean flow is a longer term average than simply averaging through the turbulence. The flow need not be steady in the traditional sense; even if there is transient oscillation between nearby states via hysteresis or inertial waves the acoustics record the mean over many seconds to as much as thirty seconds or more.

6.2 Parametrization Style for the Flow

In this section, I describe the approach to parametrize flow used in most methods in this work. Specific parametrization are addressed in chapters 8 and 9.

The flows are represented by vectors of coefficients with respect to a set of basis flows; a flow being the superposition of the basis flows weighted by the coefficients. The linearity of the frequency shifts due to flow then implies that the splitting can be calculated for the flow based on those coefficients and the amount of splitting attributable to each basis flow. These coefficients will be referred to as the model parameters, and the space in which they reside as the model space \mathbf{M} . If $\mathbf{m} \in \mathbf{M}$, then it is associated to the flow Ω by

$$\Omega = \sum_{j=1}^{dim\mathbf{M}} m_j \Omega_j \quad (6.1)$$

where $\{\Omega_j : j = 1, \dots, dim\mathbf{M}\}$ are the basis elements used for the flow parametrization. I adopt the practical approach of forcing the dimension to be finite. Even for high resolution inversions the expansion will be truncated at some index relative to the resolution needed or is reliable. Often there is a limit imposed by the discretization as well, though well beyond what is resolvable in this context.

Other styles of parametrization such as using model space parameters that are exponents of basis flows or spatial variation wavenumbers were not used, as such styles of parametrization do not as easily lend themselves to linear inversion. Since few modes are used in chapter 8 to perform inversions, those alternate styles of parametrization are quite feasible in those settings, but this work is intended for use beyond those demonstrative settings.

Parametrizing the flow well then means finding functions that can optimally capture large-scale features of the mean flow when the flow is averaged over such time scales. Basis functions are often remarked as being "complete", which means simply that for any member of a particular space of functions the basis is complete with respect to, that function can be represented as a convergent series expansion of those basis functions. When using an implicit regularization rather than a traditional Tikhonov style damping strategy though, the effects of truncation of the series can be more severe. For instance, even though products of zonal harmonics and spherical Bessel functions can represent cylindrically symmetric functions well, i.e. they form a complete basis, it is much harder to do so accurately when truncating to a dozen or so terms. For that reason, as discussed

here and in chapter 8, such basis functions were supplemented with vertically invariant cubic splines in cylindrical radius r . Producing largely vertically invariant flows using many spherical based basis functions for the meridional cross section requires far more basis functions than the flow requires or the data can support. Using more basis functions, furthermore, results in a system of equations far too underdetermined to be solved without imposing some form of explicit regularization, a regularization that in this framework would be difficult to justify if it were constructed in a way that allowed small length scale features not actually resolvable by the data.

To overcome this difficulty, a hybrid basis is primarily used in chapter 8, whereby a collection of column like splines that are a function of cylindrical radius r alone are used in addition to the products of spherical Bessel functions with zonal harmonics; specifically, the Neumann modes of the spherical annulus. The strategy is to allow the vertically invariant component to be largely represented by the splines, while the superimposed deviations from cylindrical symmetry are represented by the other zonal harmonic related components. In order to assess that the reconstructed flows were not simply mimicking the basis functions unrealistically, other basis functions such as polynomials in r and z as well as 2D Cubic splines were used to gauge the effects of the basis in biasing the results obtained in chapter 8 and discussed therein.

6.3 The Forward Operator

The forward operator C is a map from the set of admissible flows to the space of observations of resulting frequency shifts. Within the linear regime, using a finite set of basis flows, C is a matrix satisfying

$$C_{ij} = \frac{\partial f_i}{\partial m_j} \tag{6.2}$$

The range of C is the set of vectors of frequency shifts for the set of acoustic modes being imaged. Thus C_{ij} is the amount of frequency shift of the i^{th} mode due to basis flow j having coefficient 1. The frequency shift is half of the splitting between the $\pm|m_s|$ pair.

Computation of the forward operator allows for testing hypotheses about the flow without

explicit inversion. The forward operator can be calculated for even a very large basis for some inner product space, and any flow can be projected the basis functions for that space, and the coefficients can be formed into a model space vector that can have the related forward operator applied to it to see what the acoustic effects are of that flow. In that regard, the forward operator can reduce the computation time of applying the kernels to the flows directly, and utilize the coefficients of the flow to rapidly compute the acoustic effects by matrix multiplication.

Another way of thinking of the forward operator, is that it is the matrix product $K^T \mathcal{B}$, the set of inner products of the kernels with the flow basis functions; here the volume weighting by dV implicitly absorbed into K where each column of K is a kernel for a specific mode appropriately weighted at each element to allow the matrix product to carry out the volume integral.

6.4 Boundary Conditions of the Fluid Flow

No boundary conditions are imposed on the flow for inversions. Even if a no slip boundary condition is approximately true, i.e. one where the flow is following the boundary at each location of the boundary, the width of the boundary layer that decays to the boundary velocity at the wall is suitably thin so as to prevent accurate reconstruction without greater amounts of data. The viscous layer itself is so thin that possibly no amount of data is capable of accurately inferring that acoustically. That discourages the use of a set of basis functions that have imposed boundary values nor enforce a constraint that mandates their superpositions have prescribed boundary values; in the absence of a prior model or data supporting those boundary values at least. Fortunately though, this lack of resolution in that regard, is because such a thin boundary layer has little affect on acoustics. The only boundary that would possibly even need included in error analysis is the outer shell's; yet for SCF in the hydrodynamic case the vast majority of the fluid at the outer shell is following the outer shell rotation rate, in terms of azimuthal velocity component. So no such error analysis is carried out in that regard. Perhaps if the fluid was not brought to a relatively steady state before acoustics were acquired that would not be the case.

Chapter 7: Techniques of Inversion

7.1 Constrained Optimization

Relying only on the data and forward modeling of the splitting due to zonal flows as described in chapter 5, leads to non-unique results. With limited data, the non-uniqueness is accentuated.

Using Normal Equations, i.e. minimizing weighted least squares, often mandates fewer basis functions than data points. This is because the correlation and complementarity and coverage is dissimilar from observing the flow at 15 directly sampled points spaced out in the domain; many modes' sensitivity pattern makes them more analogous to very closely sampled points with large uncertainties on their functional value at those points. Introducing additional modes does not necessarily increase the resolution of the inversion, but simply reduces the uncertainty in the measurements the other modes that have similar sensitivity gauge.

Additional basis functions can only be added when using the Normal Equations if some type of damping, truncated singular value decomposition, or other regularization method is employed. Choosing the regularization parameters to do that can be difficult and highly subjective. Instead, more information can be extracted from the data if it is supplemented with physical constraints that lift the non-uniqueness of the inverse problem produced by a finer basis.

Consider the traditional weighted least squares problem

$$\begin{aligned}\Phi(m) &= \|W_d(Cm - d)\|^2 \\ m_{est} &= m^* \\ \Phi(m^*) &< \Phi(m) \quad \forall m \neq m^*\end{aligned}\tag{7.1}$$

where W_d is some form of weighting of the data based on the confidence, or inverse data covariance matrix. I solve the problem using techniques from nonlinear optimization theory. The model space is decomposed into regions, some considered physically realistic and others not; here the model space is simply the values that the coefficients of the basis functions reside in. Regions that are considered physically realistic from the feasible set, and those considered physically unrealistic have $\Phi(m) = \infty$. To minimize data misfit under this type of constraint multiple methods are employed. The most robust method employed is the Barrier Function Method (BFM). That is, penalty terms are added to the objective function that have negligible effect inside the feasible set develop large and steep gradients as the model vectors m approach the boundary of the feasible set. For a set of barrier functions $\{\beta_j : j = 1, 2, 3, \dots\}$ the weighted least squared problem is reformulated with the objective function

$$\Phi(m, t) = \frac{1}{2} \|W_d(Cm - d)\|^2 + \gamma_t \sum_{j=1}^{N_\beta} \beta_j(m) \quad (7.2)$$

The barrier functions used herein this work are antilogarithms, and physical constraints can be implemented in a variety of ways based on the prior model of the flow. The weights γ_t are means by which the boundary of the feasible region is buffered by a sharper and sharper buffer as the iterations proceed; in the limit the buffer retracts to the boundary and the gradient of the buffer is infinity at the boundary. Taking $\gamma_t = \frac{1}{t}$ is most common; as t goes to infinity the penalty goes to infinity at the boundary still, but the region in which the penalty is non trivial shrinks as $\frac{1}{t}$ tends to zero. See [Byrd et al. \[2000\]](#) for a discussion of the interior point method used that utilizes the log barrier technique. To use these methods with a non-local basis, as opposed to one that tiles the domain, requires some manipulation. When the basis does not tile the domain, one cannot just enforce the sign of the model parameters (i.e. the flow basis coefficients) to have the same sign, or employ some form of non-negative least squares or non-positive least squares method, to bound the solution. To bound the solution even by a single value of rotation rate requires an alternate formulation.

From a grid of points, sufficiently fine that the basis cannot produce local features sig-

nificantly finer than the interpolating surface through those points of minimal curvature, basis function values at those grid points for each basis function are stored in a matrix \mathbf{A} , where A_{ij} corresponds to the value of basis function indexed by j at grid point index by i . An upper bound vector is implemented as a column vector u_b , and thus

$$\mathbf{A}\mathbf{m} \leq \mathbf{u}_b. \quad (7.3)$$

where the inequality is component by component. The lower bound is similarly implemented by

$$-\mathbf{A}\mathbf{m} \leq -\mathbf{u}_l. \quad (7.4)$$

That the fluid cannot super-rotate the outer shell seems a fair approximation for these purely hydrodynamic scenarios during counter rotation, but a perhaps better bound would be obtained by bounding the average specific angular momentum. Derivatives and other functions can be expressed in this matrix form as well. Experimentation with many types of bounds was performed, such as enforcing monotonicity in rotation along profiles in r , and enforcing monotonicity in specific angular momentum along profiles in r . Such constraints only requires a suitable banded matrix to express the values at the grid points as a function of the model parameters. These matrix formulations allow many complicated flow constraints, but for this study bounding the extreme values seemed the more easily justifiable, and were used extensively in chapter 8.

Each row of this matrix inequality form is used to form a log barrier function, implicitly, e.g. $\beta_j = [\mathbf{A}\mathbf{m}]_j - [u_b]_j$ for the first set of equations, and $\beta_j = -[\mathbf{A}\mathbf{m}]_j + [u_l]_j$ for the other. In the log formalism the Jacobian and Hessian can be formed analytically using matrix expressions or evaluated using finite differences, and prevented from penetrating the boundary by backtracking line search; if the boundaries are violated, the step in the search direction can be lessened until it is within or on the boundary of the feasible set.

The system is solved iteratively using the Matlab optimization toolbox's interior point convex method first by way of the Matlab function `lsqmin`, then checked with alternate methods such as

the `fmincon` sequential quadratic programming algorithm, and `fmincon` interior point method just described that utilizes log barrier functions; no noticeable differences were observed between the two algorithms' results though for applications in chapter 8. The interior point convex algorithm is much faster, and allows ensembles of inversions to be performed efficiently to assess the sensitivity of the inversion to data uncertainties. However, it is non-obvious formulated problem is convex, or whether local minima ensures global optimization. Therefore, the slower interior point method with log barrier functions that allows an ensemble of starting points for the iterations to be chosen was used as well, to assess whether the solution is relatively unique.

Interior point convex algorithm uses a combination of Newton steps and conjugate gradient steps to perform the iterative optimization. The Newton steps attempt to solve the system first by finding a solution satisfying the Kuhn-Tucker conditions; very few iterations are typically needed in these inversions. The solution is directed along what is called the central path toward the solution. Ensembles of solutions are formed by taking random samplings of the error intervals around the data as well.

Finally, to support that the iterative solution is converging to a global minima, comparison is made with solutions from an ensemble of initial conditions by using `fmincon` in Matlab, implementing the log barrier method. They were only checked for the presented solutions though, and similar behavior was assumed for the ensemble that samples the data in the error intervals around the measurements. The only evidence for multimodal distributions resulting from that form of ensemble creation based on differing initial conditions came when significantly more basis functions were used than could be accommodated by the resolving power of the data.

The initial conditions used in chapter 8 are approximately 100 random starting points formed by the spline components of the basis. Each starting point satisfies the constraints, and also visually identical results were obtained by using the alternate algorithm sequential quadratic programming algorithm. See [Gill et al. \[1991\]](#) for a discussion of the active set method employed by the sequential quadratic programming method. Only including nonzero coefficients for the splines only in the initial conditions, is sufficient at the resolutions in chapter 8 since the mean velocity

field is expected to be largely vertically invariant.

7.2 Minimizing Spread Functions

7.2.1 Basic Principle

An alternative means of supplementing the data to obtain well-posed inverse problems is to place restrictions on regularizations by way of how the resolution matrix diffuses basis functions for the flow. In this section, it is beneficial to provide some elementary abstraction of the linear algebra involved in inverse problems, for more easily understanding what is meant by the control of diffusion. For a given set of basis flows $\mathcal{B} = [\mathcal{B}_1 \dots \mathcal{B}_N]$ define the model space \mathcal{M} associated with it as the set of coefficient vectors $\{\mathbf{m}\}$ such that any rotation profile Ω in the span of \mathcal{B} can be written in the form $\mathcal{B}m$ for some m in model space. Let \mathcal{R} be the range of the forward operator C such that

$$C : \mathcal{M} \mapsto \mathcal{R} \tag{7.5}$$

Inverting C can be done many ways, but for exposition consider regularization by a damping matrix D weighted by the damping coefficient ϵ . Define an inverse operator Q by the following formula

$$Q(\epsilon) = (C^T W C + \epsilon D^T D)^{-1} C^T W \tag{7.6}$$

where W is some form of weighting matrix such as an inverse data covariance matrix, or simply a diagonal matrix with the reciprocals of the squares of the error weights for each data observation. The inverse in the first factor need not be a traditional inverse, but could also include a pseudo inverse obtained by truncated singular value decomposition or another method. Also, ϵ has been left as a scalar for simplicity of exposition, it could be more complicated, e.g. a collection of parameters and the damping terms. The model resolution matrix is obtained by forming an endomorphism on model space by the map

$$R_m : \mathcal{M} \mapsto \mathcal{M} \tag{7.7}$$

R_m , for each choice of ϵ , is formed by the product

$$R_m(\epsilon) = Q(\epsilon)C \tag{7.8}$$

Due to both data uncertainty implicit in $Q(\epsilon)$ and also resolving power of the kernels used in forming $Q(\epsilon)$, R_m is typically not the identity matrix. For a basis \mathcal{B} such as a grid of points, tiling of the domain by disjoint convex polyhedra, or some other localized basis, each basis function may not be mapped purely to itself by the inversion process. It is said that Q diffuses \mathbf{e}_j when R_m maps $m \cdot \mathbf{e}_j$ to a vector in \mathcal{M} that is not \mathbf{e}_j . Ideally, R_m would be the trivial isomorphism, the identify map on \mathcal{M} . However, even in that case, if the actual flow producing the data does not reside in \mathcal{B} , the accuracy of the inverse generated by Q can be highly inaccurate. To reduce the ambiguity of selecting ϵ and reduce the subjectivity of the choice of epsilon, various functions can be defined on $R_m(\epsilon)$.

Finally, it should be noted that many of these techniques, at least in publicly available literature, seem to be used somewhat exclusively by disciplines that cannot readily verify their solutions, such as helioseismic inversion for rotation in the sun’s interior, gravity inversions for planetary bodies, and seismology of the deep earth and inversions for other geophysical variables. This is due partly to the fact that empirically validated results give rise to the ability to establish prior models of the expected data of higher accuracy and also heuristically base choices of regularization parameters. Since there are still so many parameters implicit in the formulation that can be said to be subjective though, it is not even true minimization of spread functions do not suffer from confirmation bias when inverting data; they lift non-uniqueness by placing the subjectivity in other choices. At best, they lift non-uniqueness for one specific regularization approach. They do not eliminate the non-uniqueness across different inversions from differing regularization methods.

7.2.2 Dirichlet Spread Function Minimization

A simple functional to define on R_m to for the purposes described in the previous material, is the Dirichlet spread function (DSF).

$$J_D(\epsilon) = \|R_m(\epsilon) - I\|_F, \quad (7.9)$$

where the norm is usual Frobenius matrix norm, the standard vector norm formed by unwrapping the matrix into a vector, and I is the identity matrix with the same dimensions as the resolution matrix. Frobenius matrix norms can also be formulated more abstractly as the square root of the trace of the product of the operator argument with its transpose/dual. Minimizing the DSF means making the resolution matrix as close to the identity as possible subject to a least squares constraint on the element wise difference. As can be seen, minimizing DSF penalizes equally any off-diagonal terms. In terms of a basis that tiles the domain by small disjoint basis functions, that amounts to penalizing any diffusion, but once diffusion occurs it does not penalize diffusion into distant tiles any more than diffusion into adjacent neighbors. This approach often better preserves finer scale features at the expense of creating overshoot and oscillation in the reconstruction.

7.2.3 Backus and Gilbert Spread Function Minimization

Weighting the matrix elements in the argument to the DSF's norm differently depending on distance between the basis functions is by far more popular than the DSF minimization approach. That is, relaxing the penalty function when the diffusion is from nearby neighboring regions of the domain. The Backus and Gilbert spread function is given by

$$J_{BG}(\epsilon) = \|w \odot (R_m(\epsilon) - I)\|_F \quad (7.10)$$

where w is some weighting of the distance between basis functions, often the squared Euclidean norm between their centroids or some other interior point, and \odot is the Hadamard product. The

Hadamard product is the element-wise matrix multiplication. When the distance between two basis functions is greater, diffusion between them during inversion is penalized more. Because any basis function is zero distance from itself, diagonal have no effect in this formulation. When the inversion produces pathological behavior such as zeros or very large or negative numbers on the diagonal of the norm's argument, additional constraints can be imposed to prevent that behavior, such as enforcing conservation of the rows of the resolution matrix, i.e. making the averaging kernels be a partition of unity or have length 1 or some other constraint.

Since the inversions in this work is on a meridional cross section, the spread matrix can have its terms weighted by the actual volume, i.e. by weighting by $(2\pi r_i dA_i)(2\pi r_j dA_j)$. Including the r_i factors, however, can degrade focus in the smaller values of r though. An argument can be made for using a weighting by the specific angular momentum as well, as it may be more desirable to conserve that quantity. With high amounts of data that has suitable coverage, it is often the case that the spread is localized and the coefficients, such as r , are approximately equal within the neighborhood of diffusion and it makes less difference what choice is made.

The parameters that optimize the spread functions can be solved using constrained optimization. In the case of a vertically invariant basis such as vertical strips, a single regularization parameter can be used and interval searches work as well. Additionally, other imposed constraints such as forcing the solution to be non-positive, the rows of the resolution matrix to sum to one or some other function, can be added as nonlinear constraints, solved either using the Matlab optimization toolbox or with Lagrange multiplier methods. It should be noted though, that the constraints related to enforcing conservation in the resolution matrix are not a constraint that was satisfied when using iterative procedures as discussed in the previous chapter. It is also questionable what the best conservation conditions for the rows should be, since unlike in helioseismology and other fields there will be non-localization to a greater degree and perhaps the angular momentum should be taken into account in different basis functions for rotation.

Since a large portion of the cavity is at rest, conservation in terms of a sum along the rows is troublesome anyway. For instance, if a row has many nonzero but small elements, typically

one would be inclined to interpret that as indicating only small diffusion into a basis function coefficient. However, some large regions are typically at rest whereas others are more locally varying. An averaging kernel though, only tells the relative weighting of the flow throughout the domain that diffuses into a basis function, not what the flow is across the domain. Such matters are somewhat ignorable when the resolution matrix simply performs a slight Gaussian blur on point sources, but for limited data such as used in chapter 8, the resolution matrix often transform point sources into objects that are exceptionally non-convex, delocalized, not positive definite, and have many other unfortunate properties.

For these reasons, these approaches were not used extensively, and not used as one of the methods in chapter 8; though one example is given. The noble goals of the methods were difficult to meet with limited data. Spread function methods had too many subjective choices that allowed tuning the formulation of the inverse problem to allow the inferred flows to take on characteristics that though plausible, were largely sculpted by the subjective choices, while still being afflicted by artifacts. However, they did serve as an excellent source for creating flows that fit the acoustic data, which facilitated understanding what features were actually required by the data.

7.3 Adaptive Parametrizations

The methods discussed in this section were only briefly examined, since they are sluggish computationally. They were later realized to be somewhat feasible since only 15 modes were usable from the provided acoustic data. Since it is still not clear how many modes are realistic to expect from liquid sodium data, it seems relevant to mention these findings.

7.3.1 Adaptive Interpolation

One way to overcome the issues with regularization that allows the parametrization to take full advantage of the data without fitting noise or the downsides of the coverage problems, is to use an adaptive parametrization. In this section, I introduce the idea of fitting the flow without using the forward operator, but only the kernels and the adapted flow reconstruction. The basic idea is

to interpolate a solution from control points in the domain and on the boundary of the domain, and instead of just performing constrained optimization on the values of rotational frequency at the control points, also allow the control points to move in terms of location. This is a much more computationally costly method. The objective function used is the same measure of misfit as weighted least squares, but the model parameters are no longer simply coefficients of a basis.

To increase the speed, the fit is done in several stages. The initial state is a combination of 15 grid points just outside the boundary of the top half of the meridional cross section, roughly equally spaced along the boundary, creating a set of points whose convex hull contains all of the domain when they are replicated to the bottom half of the cross section; that is because the function is being presumed to be even about $z=0$. These points do not move. An additional 8 points roughly equally spaced out inside the top half of the cross section are used as free moving points. The model parameters are the 23 values of rotation at each grid point, and the 8 x coordinates of the moving points and the 8 y coordinates of the moving points. They are further constrained by preventing positive rotation values, and the moving points are confined to being inside the box $[0, R_o] \times [0, R_o]$, strictly inside the domain. Everything is replicated to its mirror image so as to enforce even solution about $z=0$. The interior point method described earlier in this chapter is used to enforce the constraints. The number of moving points on the interior of the domain was chosen to be the maximum value that could be used without very small clusters of points being created. Using more can often allow the moving points to form clusters so that the solution can produced very high flow in a very small region that few modes are sensitive to, thereby fixing any misfit their have with the bulk flow, while producing highly unrealistic features, especially at the resolution expected form the data.

The first stage of adaptation produces a solution via nearest neighbor interpolation of the values at the grid points, by a Voronoi tessellation of the domain. What is noteworthy, is that it is much easier to fit the data using Voronoi tessellations than smooth interpolants, and many of the tiled flows over the meridional cross sections, seem to recover plausible placements of the high shear zone, as well as recovery of the jet instability where the inversions recovered it as well. It

suggests that perhaps high shear is more consistent with the data than smooth diffuse gradients in angular velocity.

The computational speeds on a relatively fast desktop computer, can amount to an hour or longer for an inversion if no prior is used and Hessians are computed numerically to find the search directions; using Broyden-Fletcher-Shannon-Goldfarb algorithm or similar means. It can be sped up by performing a preliminary inversion using one of the earlier described methods, then writing with respect to the interpolant formulation as accurately as possible; for instance, selecting points in the domain manually, perhaps where there is little posterior predictions in variance based on data uncertainty. Otherwise part of the sluggishness comes from flow values changing as grid positions change. Once the grid points stop moving as fast, the effects of changing the flow values at each grid point, less backtracking is needed, and hence less function evaluations.

7.3.2 Non-coefficient Model Parameters

Often it more convenient to parametrize using means other than basis functions. For instance, the more defining feature of a flow might be a region of shear and the gradient of that shear. Consider a sigmoid function

$$S(r; A, r_c, k) = A - \frac{A}{1 + e^{-k(r-r_c)}} \quad (7.11)$$

rearranging

$$S(r; A, r_c, k) = A \frac{e^{-k(r-r_c)}}{1 + e^{-k(r-r_c)}} \quad (7.12)$$

In this context, A is the amplitude of the lower rotation rate near the inner sphere and shaft, r_c is the cylindrically radial location of the shear zone, and k controls the gradient of the shear.

It is difficult to assign an uncertainty to this quantity, since the majority of the error stems more so from the idealization of the flow rather than variations in inversions due to data uncertainty.

In chapter 8 this formulation is used by fixing k to be very large and estimating the location of the shear zone. What has been found by experimentation with synthetics, is the the inversion

that is two essentially piecewise constant and disjoint basis functions who share a boundary at some value r , will place the border where the shear zone is, since the data misfit incurred by not fitting the larger volume piece by zero where it is relatively moving with the outer sphere is much larger than averaging over the portion of the cavity at values of r less than the border value of r . The data misfits are also quite small, having larger misfits where 2D features become prominent, such as a jet-like coming off the inner sphere equator at roughly $Ro=4.67$.

Such 2D features tend to defocus the shear when the value of k is allowed to vary, even though the 2D inversion profile for rotation shows a relatively vertically invariant flow excluding the jet-like feature and is no more diffuse in shear than other rotation rates; see chapter 8. This is consistent with the adaptive parametrization approach using moving grid points. The grid points do not actually spread out in the domain, but rather cluster along a the shear zone so that they can create shear when interpolation is carried out on their adapted fluid rotation values. A cylindrically symmetric basis was also used that constrained the specific angular momentum to being monotonically increasing found similar results, consistent with the high shear zone. It was not forced to taper to a constant rotation rate on values of r less than that at the shear zone, yet recovered that feature as well.

Chapter 8: Applications to Ambient Noise Data

With only 15 usable modes, and not 15 specifically chosen modes, extracting useful robust information about the flows is challenging; especially using ambient noise as the acoustic source. In this chapter, inversions are performed, and discussion of quality of fit to data, and reliability of the reconstructed flow are presented.

8.1 Data Processing

8.1.1 Array Configuration

The modes used for inversions had stationary frequencies up to approximately 2.1 kHz; see table 8.1.1. The microphone configuration did not allow $|m_s|$ to be identified using array techniques, since they were all separated by π with respect to the azimuthal angle. The configuration could not be easily changed, I was informed. Another microphone was offset in the polar direction to be able to perhaps distinguish via $l - |m_s|$, however only two microphones could be used at one time. An additional microphone had been placed at an offset from another by roughly seven degrees in the azimuthal direction, in the hope of being able to distinguish between values of $|m_s|$ and increase the data set size. The small angle would have allowed many more modes to be identified, but was perhaps overly ambitious in the small spacing; the small separation and combination of the effects seen in the signals made difficulties in using the same cross correlation technique used in [Triana et al. \[2014\]](#).

The microphones separated by 180 degrees in azimuth were used in the data. The microphones were at 45 degrees in terms of colatitude. The explanation given, being that sum and difference techniques were able to remove a great deal of the noise; specifically, odd valued $|m_s|$

modes would be greatly amplified by taking the difference between the two microphone signals, and since presumably digital noise and mechanical noise would be the same on each channel, would be virtually removed in the result. Odd valued $|m_s|$ modes have equal magnitude but opposite sign at locations separated by 180 degrees in azimuth; hence taking the difference doubles their signal level while removing any features that are the same in both signals. The microphones were only calibrated insofar as the same level was recorded at each location; the frequency response was not calibrated. Calibration of the frequency response would likely have been of little help with ambient noise data, since the strength of the source term distribution is unknown. That is, knowing the loudness of each mode at the microphone position is of limited value if the source terms are not equal as well. Relative amplitudes should be equal at equal azimuthal angle for the mode as well. These limitations of the array geometry made the FEM predictions all the more important, since the array techniques available could only distinguish between evenness and oddness of $|m_s|$, placing additional emphasis on knowing the correct frequency range to expect modes to appear in. The mode identifications were thus done by evenness and oddness and frequency location. In all but one instance, the modes could be unambiguously identified based on that criteria. Mode (1,3,2) was slightly ambiguous, but was distinguished based on its splitting behavior and consistency with the flow suggested by the other modes observed. Although, the identification analysis revealed the inversions were robust to removing this mode from the set, and hence the mode was not providing any qualitative difference or visible addition of information. This would likely not be the case if the residual frequency shifts were larger relative to the error bars associated with the measurements of the spectra. It was tempting to try and identify other modes based on the inversions and then increase resolution by including them. However, it seemed too likely to create a gross error though, with no benefit. If a splitting was very accurately predicted by the inversion with fewer modes used, then including the other modes that matched that inversion's prediction did not really have any added benefit. When the spectral location did not match the inversion with fewer modes sufficiently for that to occur, and possibly presented new information, there was still too much ambiguity to have any comfort in the accuracy of the identification. The benefits

index	n	l	m	f (Hz)	δf_6 (Hz)
1	0	1	1	346	4.0
2	0	2	1	570	1.3
3	0	3	1	774	0.4
4	0	3	2	807	2.8
5	0	4	1	970	-0.0
6	0	4	3	1014	3.0
7	1	1	1	1045	-0.8
8	0	5	1	1165	-0.2
9	0	6	1	1361	-0.2
10	1	3	2	1500	-0.2
11	1	4	1	1702	-0.7
12	2	2	1	1898	-0.6
13	1	5	1	1938	-0.5
14	2	3	1	2060	-0.8
15	2	3	2	2099	-0.5

Table 8.1: Mode wavenumbers and stationary frequency prediction at $c=344$ m/s. These are the modes used to perform the inversions. Additionally, the frequency shift from center frequency due to uniform rotation with the outer shell at 6Hz has been provided, rounded to 1 decimal place, since it does not appear in the presented splitting data, it has been subtracted off. The negative sign indicated that $-|m_s|$ has a higher frequency than $+|m_s|$. Values rounded to nearest tenth of a Hz. The splitting is thus approximately twice these listed values. The first column provides the index used in plots of data fits in this chapter, for reference. They are always presented in this order herein.

were too little to risk corrupting the solution with incorrectly identified modes.

Unfortunately, the majority of the data for 60cm setup is ambient noise based. That is, the resonances are either excited by mechanical vibration or the flow of the air. The amplitude of the signal in each frequency band was not constant across within every frequency band. This means the spectrum in each band is convolved with the spectrum of the amplitude envelope of the band. For instance, for a simple sinusoidal amplitude envelope in the time domain that amounts to convolving with two delta spikes about the origin in the frequency domain, as discussed in chapter 1.

Signals were decimated by a factor of 6, and spectra were computed using prolate spheroidal slepians with a time bandwidth product of 2.5; a window was chosen to smooth the clusters in typical peaks that would be obtained by a steady resonance. The widths of the spectral peaks is not due purely to defocussing of a single peak though, but also the smearing together of the cluster presumably. Given the noise, the affects of the flowing air, turbulence, computing the splitting was not as simple as locating two peaks and measuring the frequency separation, typically. For

each peak, I chose two points on both sides of the localization of frequency content contributing to a mode. The mean location of the mode resonance inside that band was often within 1/2 radius around the center of those measurements, but it could not be said that there were not fluctuations beyond that interval for short instants. See figure 8.1. The shift from center frequency being half of the splitting inferred from the measurements at corresponding $|m_s|$ pair. There is good reason to suspect that to a significant extent, the pair moved in an either correlated or anti-correlated fashion. As such, resolving power was not removed from a basis if the basis could fit the data by 1/4 of the average error radius associated with the data. It does not mean the inversion is over-fitting the mean angular velocity field, only possibly misfitting any one particular flow state during the signal acquisition.

There is not a universal rule for calculating the splittings employed though, as all were not as simple to measure as figure 8.1. The guiding principle was accurately gauging the mean splitting to within as small an error radius as possible. If a splitting could be reliably constrained, it was measured. For instance, often digital noise overlapped the spectra forcing the estimate of the flanks of the spectra locations to be expanded, being conservative. In some instances, the mode peaks were sufficiently clear, but the splitting was so small that not only was the overlap of the modes taken under consideration in judging their mean spectral peak locations, but also the fact that it was not completely obvious which mode in the mode pair $|m_s|$ was on the left and which was on the right; that effectively doubled the error radius. That meant that often the average data misfit was not a good indicator by itself, and the fitting across the mode set was very informative to analyze.

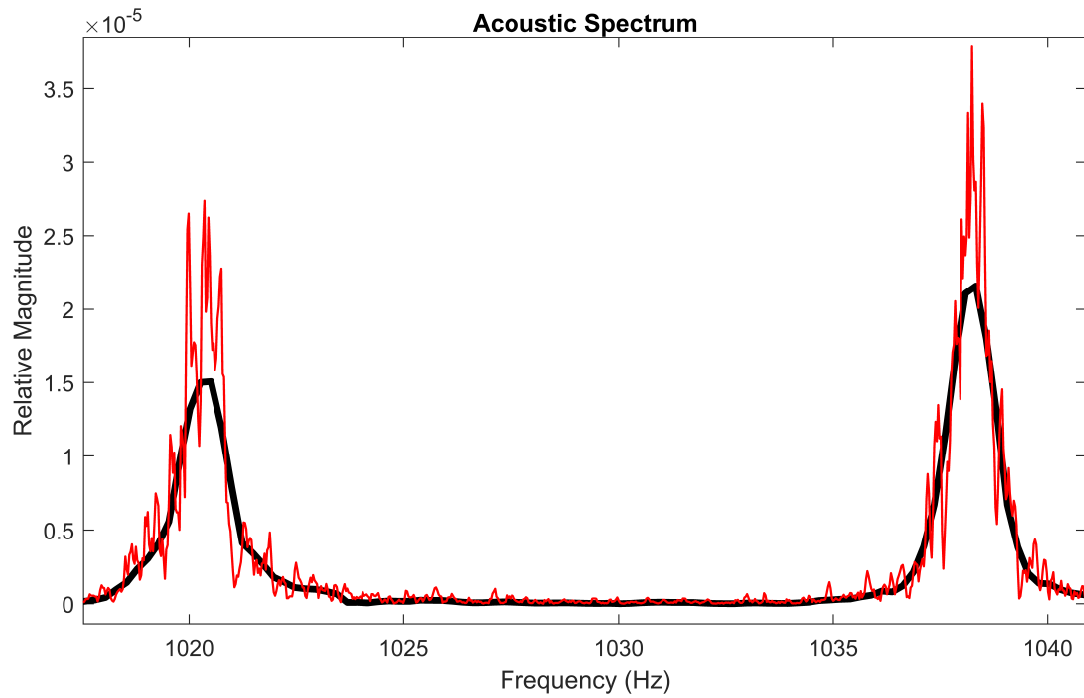


Figure 8.1: Comparison of acoustic spectrum with different frequency resolutions. The black curve has been created with a frequency resolution of 0.3 Hz whereas the red curve has a frequency resolution of 0.05 Hz. Note: magnitudes are linear, not in decibels. The clusters of peaks could be due to poloidal flow, noise envelopes, mechanical noise, changing mean flow state during time integration, or some combination thereof.

As can be seen from the red curve in figure 8.1, it is useful to have error bars that encompass values of splitting due to changes in flow as well. Though it could be the affects of noise envelopes or transient poloidal flow changes, there could be changes in zonal flow state as well. The actual estimate on the error of the mean is smaller than the error that encompasses possible changes in the flow state. For the inversions this makes no significant different. Since a uniform scaling only has effects on inversions when the data strongly dislike the constraints and trade-offs in data misfit tolerances with constraint violation tolerances cause it to violate the constraints slightly. A future improvement could include a hierarchical approach to different types of errors, but a conservative approach was taken in this work since it is not completely clear what is affecting the distribution inherent in those peaks, in terms of noise, different levels of excitation, different microphone response, changing flow, quality factors of the modes, and turbulence.

To facilitate identifying the modes amidst the noise and other aspects of the signal, the spectra were formed into an intensity plot with acoustic frequency as horizontal axis and inner sphere rotation rate as vertical axis; see figure 8.2 for an example. In these spectrograms, the dynamics of the peak locations could then be tracked over the range of rotation rates. Even with the drifts due to thermal fluctuation as the experiments proceeded, there is a relatively continuous trend in each peak. Thus alleviating any uncertainties about which peak is acoustic and which is digital noise or another mode. The strategy of measuring the splitting was then performed with the signal plotted below these spectrograms, so that the signal could be analyzed in concert with these spectrograms; see figure 8.5.

The first stage of processing the splitting data is assign a polarity to the splitting. The measured splittings do not give the polarity of the splitting, whether the $+|m_s|$ or the $-|m_s|$ mode is the higher or lower frequency. Sum and difference techniques were used to infer the even and odd parity of the value of $|m_s|$, but the polarity had to be inferred based on physical assumptions of the flow.

For inner only rotating and the microphone in the outer shell rotation rates of the fluid with the same sign as the inner sphere's rotation rate can be presumed. Once the outer shell is moving

though, the effect of advection on the spectra in the majority of the cavity is greatly diminished, and the majority of the volume of fluid is nearly at rest in the rotating frame for many Rossby numbers; the splitting measured there is more so dominated by the Coriolis induced splitting. For instance, if a splitting is measured to be 2 Hz in the rotating frame, and the prediction of uniform rotation is a Coriolis induced splitting of -1.4 Hz, there is ambiguity if the splitting due to flow relative to the rotating frame is an additional 3.4 Hz, or if it is only an additional 0.6 Hz, since the original measurement could have actually corresponded to -2 Hz. Since data was acquired at a broad range of rotation rates, for instance the outer spinning at 6 Hz while the inner was spinning at -4, -6,...,-40 Hz, it is possible to track the splitting from a regime where the sign can be safely presumed back to a regime where it would be more ambiguous. This places more emphasis on the physical constraints used in the inversion, since the ill-posedness of the problem in their absence would allow any polarity to be fit, at the expense of producing a physically unrealistic reconstructed flow. The next stage of processing of the splitting data is to remove the effect of the rotating frame.

The Coriolis induced splitting due to uniform rotation is subtracted from the data, and then the inversion is done in the rotating frame as if it were at rest. This does not presume the nominal value of the rotation rate is correct, but the flow rotation reconstructed is relative to that assumption; the inversion is relative to a constant rotation frame at the nominal value of rotation. For inversions that place upper bounds on the rotation rate, the expected average deviation from the nominal rotation rate is not sufficiently large to warrant discussion of how a tiny fraction of a Hz error in the bound affects the inversions, since they are not at an accuracy level it would be relevant. There is a tolerance of a several hundredths of a Hz allowed also, and testing was done to show that small fluctuations in the upper bound did produce a visually dissimilar answer; often that bound could be substantially raised by several Hz while often only incurring small oscillations above the upper rotation rate limit in the profiles. If the flow was sub-rotating relative to the outer shell slightly, this work does address whether that is due to the fluid rotation rate being slower, or if the nominal value of rotation is slightly inaccurate; a precision motor was used, and

the deviation is claimed to be negligible for these purposes [Lathrop, personal communication].

Figure 8.2 shows an intensity plot for power at each frequency with axis representing acoustic frequency and inner rotation rate frequency for the mode (0,1,1), as recorded in the rotating frame. Microphones at $\phi = 0$ and $\phi = 180$ degrees and both at $\theta = 45$ degrees were used, and their difference taken so as to avoid noise and modes with even m . The mode (0,1,0) is absent in the plot as a result of the difference being taken of the two microphones. The sum of the two microphones is plotted in figure 8.3.

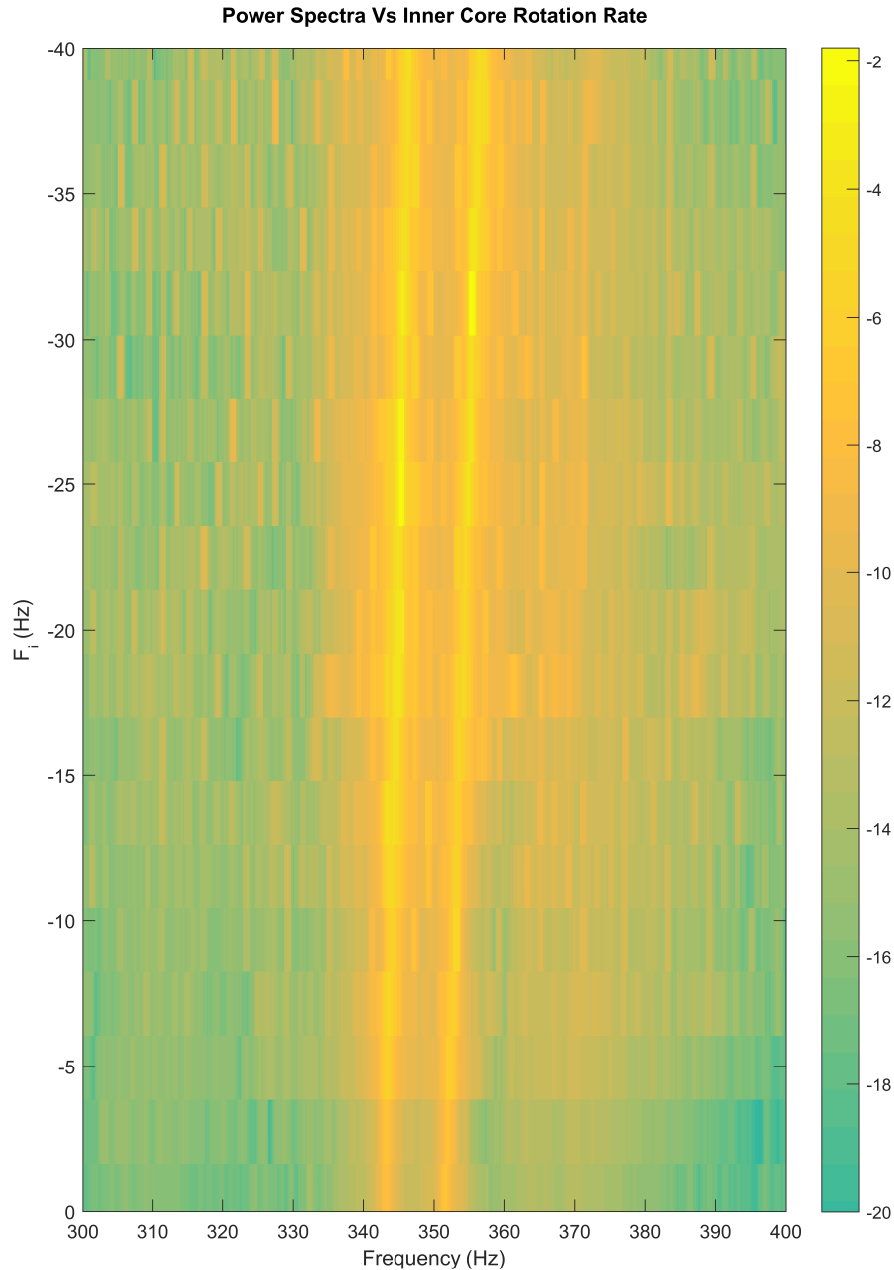


Figure 8.2: Power spectra plot of acoustic frequency(horizontal axis) vs. inner core rotation rate (vertical axis) near the modes $(0,1,1)$ and $(0,1,-1)$. Color is relative amplitude in log scale. The spectra is computed by taking the difference at two microphones at equal latitude spaced apart by 180 degrees in terms of azimuth. This shows drift as the temperature increases inducing center frequency shift, and shows that the dominant effect on splitting is the outer spinning at 6 Hz rather than the greater splitting that occurs due to additional rotation of the inner core. There could also be some effect of poloidal flow. In this regime centrifugal force is not expected to have any significant effects.

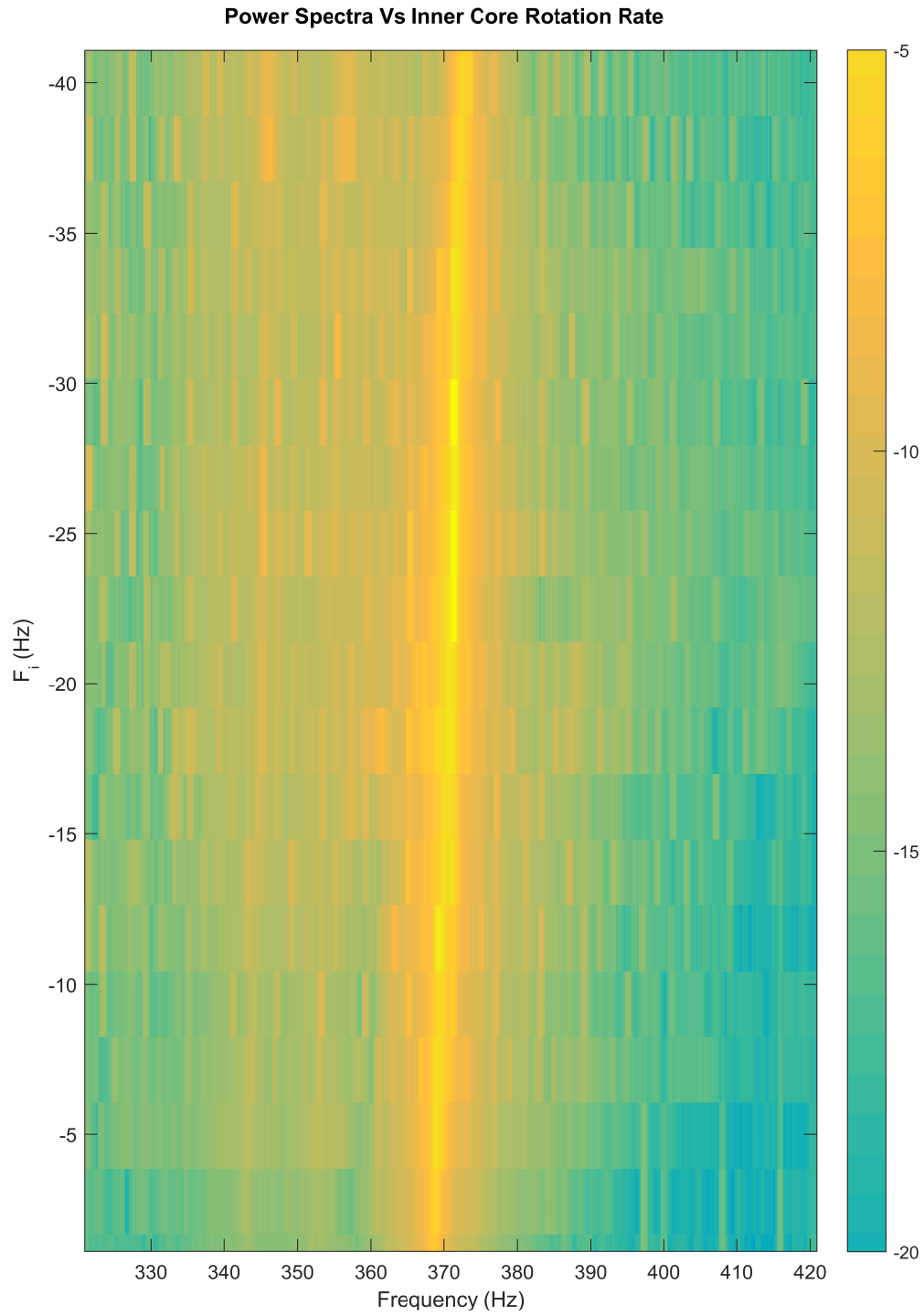


Figure 8.3: Similar figure and axes as in figure 8.2. Power spectra plot of power spectral density vs. inner core rotation rate near the mode(0,1,0). This shows drift as the temperature increases inducing center frequency shift. Color is relative amplitude in log scale. The spectra is computed by taking the sum of two microphones at equal latitude spaced apart by 180 degrees in terms of azimuth.

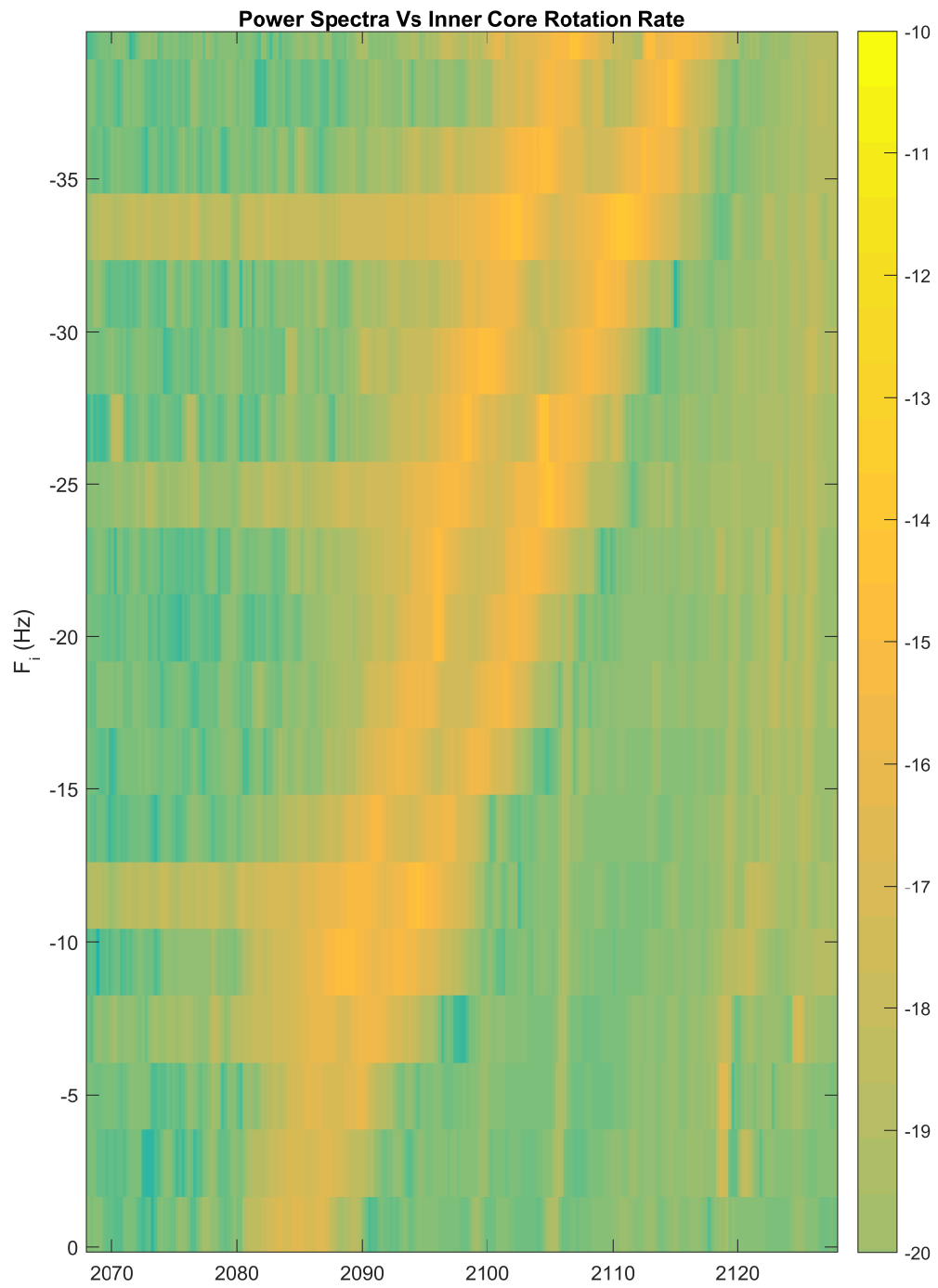


Figure 8.4: Power spectra plot of frequency vs. inner core rotation rate near the mode (2,3,1). Intensity of the plot is power spectral density, relative amplitude in log-scale. Note splitting changes with rotation rate, and also the drift of the center frequency.

$(0,1,1)$ and $(0,1,-1)$ are the lowest frequency acoustic modes of the resonant cavity, and their splitting is dominated by the Coriolis effect due to being in the rotating frame in the regimes of these experiments. The additional shifts due to the shear flows are apparent, but much less pronounced; the drift due to increasing temperature associated with spinning the inner core faster and the fact that the experiment had been running longer is more obvious. Plots such figure 8.5 allow the trend of the mode peaks to be seen in the spectra, since when looking at a single inner core rotation rate, ambiguity can arise as to what the actual acoustic peak is and what is a mechanical noise or resonance.

For instance in figure 8.4, which shows the difference power spectra between two microphones, centered near $(2,3,-1-)$ in the spectrum, the signal to noise ratio is not as high and noise is more apparent.

Figure 8.4 also shows that the effect of the inner core is more significant for $(2,3,1)$. The splitting is nearly 0 when the Rossby number is low; it is offsetting the effect induced by the Coriolis force to split the pair negatively. The error bars are large for this mode when the Rossby number is nearly zero, since the peaks cannot be separated well. The splitting can be tracked in figure 8.4 back to where that splitting of zero occurs. For a inner core rotation rate of +6 Hz, the expected splitting is that of uniform rotation, but between inner core rotation rates of +6 Hz and 0 Hz, without making assumptions about the flow pattern, it is impossible to judge the sign of the splitting. This sign ambiguity was tested by assuming a geostrophic profile and a monotonic profile between the axle and where the expected region that is executing solid body rotation occurs, and found the sign was too variable in regard to profile input.

The plotting of the profiles for each rotation rate was very useful in more ambiguous cases such as the one illustrated in figure 8.5, which shows power spectra in close vicinity to digital noise peaks in the spectrum.

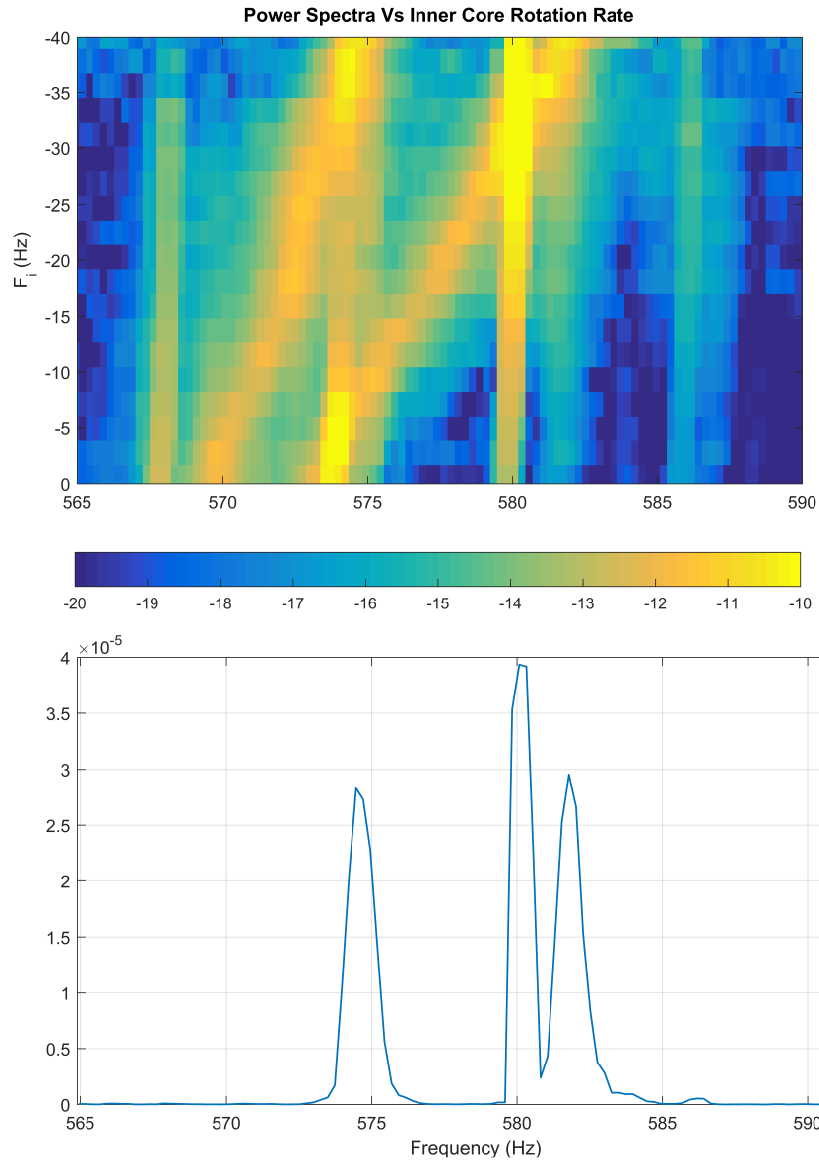


Figure 8.5: Power spectra plot (difference between microphones) of power spectral density vs. inner core rotation rate near the modes (0,2,1) and (0,2,-1). This shows drift as the temperature increases inducing center frequency shift, and shows that the dominant effect on splitting is the outer spinning at 6 Hz rather than the greater splitting that occurs due to additional rotation of the inner core. The lower plot is a power spectral density estimate placed on a linear scale, for inner core rotation rate of -40 Hz. It is a relative amplitude, not calibrated to any particular loudness level.

Figure 8.5 shows a double peak around the second mode of the pair. The spectral plot shows a periodic noise feature in the range of the spectra that overlaps the two modes' spectra; 4 columns can be seen in the plot evenly spaced, due to noise. The acoustic peaks have a different characteristic shape, but the plots make it much more obvious what is the acoustic signal and what is the electronic noise. It also shows how in the left peak, there is overlap, which causes a slightly increased amount of uncertainty placed on the peak location. It is not clear that the peak is the best estimate of the mean location of the acoustic spectral energy.

To ensure that visible drift of the center frequency is explainable entirely by thermal induced uniform soundspeed increases associated with the experiment running, the frequencies of the $m_s = 0$ modes were calibrated to the highest observed $m_s = 0$ mode (1,6,0) to test their relative invariance; each observed $m_s = 0$ mode's observed frequency was multiplied by the ratio of the original starting center frequency associated with (1,6,0) to the observed (1,6,0) frequency at the time of measurement. This follows from assuming the wavenumber k such that $\omega = kc$ is invariant then the calibrated frequency

$$f_{calibrated} = f_t \cdot \frac{f_o^{(1,6,0)}}{f_t^{(1,6,0)}} \quad (8.1)$$

should remain invariant as well, where f_o is the frequency at some reference state soundspeed, and f_t is the frequency at the current observation. This is equivalent to

$$f_t = f_o \frac{c_t}{c_o} \quad (8.2)$$

where c is the sound-speed defined with the same subscript notation as for frequency.

Once normalized this way, the drift of the $m_s = 0$ modes all had a standard deviation of 0.33 Hz or less, with only a few outliers that were easily explained by the data uncertainty.

8.2 Parametrization

8.2.1 Approach to Parametrizing Fluid Rotation

The rotational profile is parametrized two different ways and inversions are performed. One method utilizes a basis that caters to expected flows, the other being more generic and more localized.

Also, the constrained optimization approach bounds the solution, which can strain the side lobes of modal type basis functions that prefer to oscillate around the answer rather than be bounded by it; in regions of the cavity near uniform rotation with the outer shell, the ripple being bounded below that rotation rate could distort the answer slightly more than necessary. The bound related to the inner sphere did not seem to have significant effect so long as a reasonable rate was chosen, between one half and the rate of the inner sphere. The locations that seem to be more affected by the specific bound, are inside the missing pieces of the shaft; a region that little significance should be attached to with respect to the reliability of the inversions already.

Additionally, the inclusion of cubic splines that are only a function of cylindrical radius strongly supports flows that have rotation profiles that are strongly cylindrically symmetric; i.e. vertically invariant to a marked degree. However, when the vertical heterogeneity of the profile is highly localized, smearing into the splines occurs as a result of them being able to fit the data better than the modal basis components; many of the regions of the cavity have little sensitivity. Comparison with a more localized basis offers the chance to see if the inversion produced that way has contiguous vertically invariant components or if they are possibly an illusion due to smearing inherent with the lossy inversion.

The most difficult aspect of using such a small data set, is that it is quite easy to fit the data with any number of profiles usually; more advanced techniques to regularize the problem are difficult without introducing subjective parameters and ad hoc justifications. The approach adopted with the limited data, is to provide a tool for laboratory experiments which generate inversions that robust features can be assessed from, and combined with other observations provide

a tool for improving methods to explore dynamo theory; not necessarily provide rigorous evidence for the recovered profiles' accuracy. With So few spectra and difficult to interpret error bars incurred by being relegated to ambient noise data, providing quantification to the recovered profiles for very localized regions of flow is not recommended.

The resolution chosen, i.e. the basis chosen, was also to prevent over-fitting the data. The goal of having misfits between 1/4 and 1 as the average misfit was chosen for two reasons: 1) it prevents outliers with respect to the error intervals assigned, and 2) the actual mean flow splitting is likely to be as low as approximately one half or less of the estimate, since the majority of the error comes from clustering of peaks around each spectra; the $+|m|$ versus $-|m|$ pair are highly correlated in their relative motion in the spectrum. An error of 1 would correspond to completely uncorrelated errors in $+|m_s|$ and $-|m_s|$ modes, 1/2 would correspond to assuming correlation of their mean location, and 1/4 would correspond to further assuming that their mean is more accurate than the actual measurements. What is meant by the last statement, is that the way the way the splittings were originally measured attempted to capture the variation about the mean, but the mean is much more accurate. As a demonstrative example, suppose there was a 2-peak cluster at 1001 Hz and 1003 Hz and it's mode pair of the same $(n,l,-m-)$ had a corresponding 2-peak cluster at 1011 Hz and 1013 Hz. The measurement would grab the the point on the left of 1001 Hz at FWHM of the 1001 Hz peak, and at FWHM to the right of the peak at 1003 Hz. The location of the average is then $1002 \pm \text{FWHM}$, and similarly for the right 2-peak cluster. The shift due to azimuthal flow is half the splitting.

Even if changing flow state anticorrelates which peaks correspond to each other from cluster to cluster, their mean splitting over the time acquisition is still approximated by the mean separation of the cluster centers; though it could be a splitting value the actual flow does not produce for any significant amount of time, but the mean flow over a large time interval might not ever be realized by the fluid as a mean flow over shorter time interval either. Most often, as was the case for the example in figure 8.5, the mean of the peak cluster was more accurate than the actual distribution could be approximated by it's mean. The error on the mean was due to them not

being delta spikes, not because the mean was not known more accurately. Since there were so many different types of errors though, it seemed more prudent to present them using this scaling, rather than rescale to this interpretation. For instance, at some of the low rotation rates, the splitting was so small that it is difficult to judge the polarity of the modes, i.e. which member of $(n, l, |m_s|)$ is on the left and which is on the right in the spectrum. The error bar had to be larger not because it was difficult to measure the small splitting δf , but because the actual splitting could be $-\delta f$.

8.2.2 Cylindrically Radial Cubic B-Splines and Neumann Modes

The flow is parametrized by a combination of cubic splines in the cylindrical radius parameter and Neumann modes of the spherical annulus, the total number of basis functions numbering 15, the total number of splittings used; the modes had stationary frequencies up to approximately 2.1 kHz.

Six equally spaced cubic splines with two on the endpoints of the range of cylindrical radius values having their peaks at the outer boundary and at the shaft radius were used. The cubic splines help to parametrize the cylindrically symmetric component of the flow. They are essential for slow flows relative to the outer sphere's rotation rate, which are approximately geostrophic in much of the cavity, and for the capturing the cylindrically symmetric component of the flow at higher flow rates. The splines in cylindrical radius r cannot create a very sharp shear at the tangent cylinder, it must be somewhat defocused. Using more splines so that such an effect is achievable, runs the risk of over fitting the data and decreasing robustness in favor of higher resolution. It is however possible, to simply add a vertical rectangle function there to accommodate shear at the single region, but in this study care has been taken to prevent as much as possible the creation of features in the inversion that are idiosyncrasies of the particular basis chosen, and so that has not been done herein; the way it is done here, may not be ideal for inverting when there is very strong shear at the tangent cylinder, but when the inversion stratifies the flow into obvious regimes inside and out of the tangent cylinder, it is less likely an artifact of the parametrization; and the interpretation of defocussing of the shear at the tangent cylinder by the inversion requires user

interpretation and judgment when making decisions.

Deviations from vertical invariance were parametrized by the products of zonal harmonics with the radial wave functions of the acoustic spherical annulus; the spherical Neumann modes of the spherical annulus. These Neumann modes were all the combinations of the first 3 values of n for even values of $l=0,2,4$. They were computed using the same method as described in the Numeric Methods section. The radial functions were computed by FEM and the polar component by using zonal harmonics. The actual modes of the cavity were not used since those are not strictly even about $\theta = 0$ due to the asymmetry of the missing pieces; though I did use that approach in earlier work. Even in absence of the asymmetry, though, vanishing Neumann conditions are not ideal along the shaft anyway, and any flatness along the shaft of the 2D profile is well compensated by the cylindrical spline overlapping it. For much higher resolution inversions, using the modes of a modified cavity whereby the missing pieces on the bottom and top are made equal to ensure symmetry could be preferable. Odd values of degree l were not included, since they yield components that are approximately in the nullspace, and slight deviations due to the asymmetries due to the missing pieces seemed unlikely to be captured accurately with low-resolution inversions such as these. This means that the reconstructed flow around the missing piece in the bottom hemisphere may not be very reliable at all, since it is a composite effect of assuming the flow is even about $z = 0$ when the missing pieces are slightly different size in the top vs. bottom hemispheres. All inversions except where otherwise stated, use this parametrization. Other bases consisting of splines or polynomials or indicator functions have been used to assess bias introduced by the basis, and are noted directly throughout. The bias introduced by a basis does not only stem from its span, but also how that span relates to the sensitivity kernels of the modes used to perform the inversions.

It is important to note that using low-resolution basis increases the robustness of the inversion to data uncertainty, but it does not actually increase the confidence in the inversion unless one presumes that the flow is virtually devoid of variations at length scales that cannot be resolved by the flow basis. Using a low-resolution basis actually magnifies the errors with respect to small-scale

variations in favor of capturing broad averages more reliably, presumably. To prevent bias caused by the parametrization, alternate parametrization are presented as well, to show the manner in which low-resolution reconstructions can defocus flow differently, as a means of gauging what are the actually robust and persistent features across inversions.

8.2.3 Choice of Reference Frame

The inversion was performed in the rotating frame by removing the effect of uniform rotation Coriolis induced splitting from the data using first order perturbation theory prediction, then performing the inversion as if at rest. The outer sphere is rotating at 6 Hz; the inner sphere is rotating at -4 Hz for the low rotation rate inversion and at -22 Hz for the next rotation rate focused on, and -40 Hz for the highest magnitude inner rotation rate inversion; intermediate values are also used for inversions and analysis. The solution was solved by constraining the values of rotation at any location to be between the inner and outer rotation rates. Regularization is implicit due to the low-resolution basis used to accommodate the low amount of usable data and resolving power of the spectra observed in terms of sensitivity. Part of this work is developing means of implementing such types of constraints and assessing their influence on solutions, more so than the specific applications in this chapter.

8.3 Processed Data

In this section I present the data used throughout the rest of the chapter. Three tables, 8.2 8.3 and 8.4 give rounded values for the data used in this chapter.

(n, l, m_s)	-4	-6	-8	-10	-12	-14	-16	-18	20	-22	-24	-26	-28	-30	-32	-34	-36	-38	-40
(0,1,1)	0.3	0.4	0.4	0.5	0.6	0.6	0.6	0.5	0.5	0.7	0.6	0.8	1.0	1.1	1.0	1.1	0.7	1.2	1.3
(0,2,1)	0.5	0.7	0.6	0.6	0.7	0.7	0.7	1.0	1.2	1.2	1.5	1.6	1.6	1.7	1.8	1.7	2.1	2.4	2.3
(0,3,1)	0.7	0.5	1.1	1.1	0.8	1.3	1.5	1.7	1.6	1.4	2.0	2.4	2.5	2.6	2.7	2.6	2.8	2.6	2.7
(0,3,2)	0.3	0.6	0.7	0.9	1.1	1.3	1.4	1.8	1.7	2.0	2.2	2.5	2.8	2.9	3.1	3.4	3.7	3.9	4.4
(0,4,1)	1.0	1.2	1.1	1.4	1.6	1.7	1.9	2.2	2.1	2.5	2.7	2.8	3.0	3.2	3.4	3.5	3.4	3.4	3.6
(0,4,3)	0.2	0.3	0.5	0.7	1.0	1.2	1.4	1.6	1.8	2.3	2.7	3.1	3.5	3.9	4.2	4.6	5.1	5.5	5.9
(1,1,1)	0.8	0.8	0.8	0.9	1.3	1.5	1.8	2.0	2.4	2.6	2.9	3.3	3.5	3.7	4.0	4.2	4.3	4.5	4.7
(0,5,1)	0.5	0.6	1.2	1.2	1.6	2.0	1.8	2.1	2.0	2.1	2.8	2.6	2.6	2.8	3.0	3.2	3.5	3.6	3.5
(0,6,1)	0.8	1.1	1.6	1.2	1.4	1.8	1.8	2.0	2.4	2.5	2.6	2.7	2.9	2.9	3.0	3.1	2.9	3.2	3.3
(1,3,2)	1.2	1.9	2.4	2.5	2.9	3.5	4.0	4.8	5.2	5.7	6.0	6.5	7.0	7.4	7.4	7.9	8.1	8.3	8.5
(1,4,1)	0.8	2.5	2.8	2.6	3.0	3.1	3.6	3.6	3.8	3.8	4.3	4.2	4.8	4.7	4.6	4.3	4.9	5.3	5.1
(2,2,1)	1.2	1.5	1.7	2.2	2.5	2.6	2.9	3.4	3.6	3.6	4.3	3.9	4.9	4.5	4.6	4.5	4.9	4.3	4.4
(1,5,1)	1.5	2.2	1.8	1.9	2.0	2.0	3.0	3.5	3.4	4.1	3.8	3.9	4.3	4.2	4.6	4.8	4.4	4.1	3.7
(2,3,1)	2.2	2.1	2.5	2.7	2.9	3.2	3.6	3.8	4.1	4.3	4.5	4.5	4.5	5.0	5.2	5.2	5.1	5.1	5.1
(2,3,2)	1.4	1.9	2.6	3.2	3.5	4.2	5.5	5.2	6.1	6.7	6.9	7.3	7.7	8.3	8.2	8.4	8.6	9.2	9.6

Table 8.2: Frequency shift from center frequency in Hz. Top row is F_i in Hz, and each row is a mode pair given by the first column. Measurements are in Hz. Outer Sphere is rotating at 6 Hz and the inner sphere rotation in Hz is given at the top of each column. Each row is for one particular mode. The data has had the correction due to being in a rotating frame removed from it. For instance, the first row shows (0,1,1) has relatively small shifts, but its shift due to the Coriolis effect of being in a rotating frame is almost 4 Hz. The value stated is the residual after that amount was subtracted off. Refer to table 8.1 for the approximate Coriolis correction of the rotating frame that has been removed.

(n,l, m)	-4	-6	-8	-10	-12	-14	-16	-18	20	-22	-24	-26	-28	-30	-32	-34	-36	-38	-40
(0,1,1)	0.3	0.2	0.3	0.3	0.2	0.4	0.4	0.2	0.2	0.2	0.3	0.2	0.2	0.3	0.2	0.2	0.3	0.3	0.2
(0,2,1)	0.2	0.2	0.2	0.2	0.2	0.2	0.2	0.2	0.2	0.2	0.2	0.3	0.4	0.3	0.2	0.2	0.1	0.1	0.2
(0,3,1)	0.2	0.2	0.2	0.2	0.2	0.2	0.3	0.2	0.2	0.2	0.2	0.3	0.4	0.3	0.2	0.2	0.2	0.2	0.2
(0,3,2)	0.3	0.5	0.4	0.3	0.3	0.4	0.4	0.4	0.3	0.3	0.3	0.3	0.3	0.5	0.4	0.4	0.3	0.4	0.2
(0,4,1)	0.3	0.3	0.2	0.3	0.4	0.3	0.3	0.3	0.3	0.4	0.4	0.4	0.4	0.4	0.4	0.4	0.4	0.4	0.4
(0,4,3)	0.3	0.3	0.3	0.3	0.3	0.2	0.2	0.3	0.3	0.3	0.3	0.4	0.4	0.4	0.4	0.4	0.4	0.4	0.4
(1,1,1)	0.3	0.2	0.2	0.2	0.2	0.1	0.1	0.2	0.2	0.3	0.2	0.2	0.2	0.2	0.2	0.3	0.3	0.3	0.4
(0,5,1)	0.6	0.4	0.4	0.4	0.4	0.4	0.4	0.4	0.3	0.3	0.5	0.5	0.5	0.6	0.5	0.5	0.4	0.5	0.4
(0,6,1)	0.5	0.4	0.5	0.4	0.5	0.5	0.5	0.6	0.5	0.5	0.5	0.6	0.6	0.6	0.7	0.6	0.6	0.6	0.5
(1,3,2)	0.3	0.3	0.3	0.3	0.3	0.2	0.3	0.3	0.3	0.3	0.3	0.5	0.4	0.4	0.5	0.5	0.5	0.5	0.4
(1,4,1)	0.7	0.4	0.4	0.4	0.5	0.5	0.5	0.5	0.6	0.7	0.6	0.8	0.9	0.8	0.9	0.7	0.6	0.7	0.6
(2,2,1)	0.4	0.3	0.3	0.4	0.3	0.6	0.3	0.3	0.3	0.4	0.5	0.3	0.3	0.2	0.3	0.2	0.3	0.4	0.4
(1,5,1)	0.5	0.8	0.7	0.8	0.6	0.7	0.6	0.6	0.5	0.7	0.7	0.5	0.4	0.7	0.8	0.6	0.6	0.5	0.3
(2,3,1)	0.5	0.5	0.5	0.5	0.6	0.5	0.5	0.6	0.5	0.5	0.4	0.5	0.5	0.5	0.6	0.5	0.8	0.5	0.6
(2,3,2)	0.4	0.4	0.4	0.3	0.7	0.5	0.7	0.6	0.5	0.4	0.4	0.5	0.4	0.5	0.4	0.6	0.6	0.7	0.6

Table 8.3: Errors (Hz) relative to the mean that are used for performing inversions. Table layout presented in the same form as table 8.2. Values are rounded off to nearest tenth in the table.

(n,l, m)	-4	-6	-8	-10	-12	-14	-16	-18	20	-22	-24	-26	-28	-30	-32	-34	-36	-38	-40
(0,1,1)	111	56	60	62	38	64	57	44	44	29	49	20	17	23	18	22	44	22	18
(0,2,1)	33	25	27	37	23	23	27	19	18	17	15	16	23	16	12	10	5	5	7
(0,3,1)	32	35	22	22	26	17	18	12	14	14	11	11	15	10	9	8	7	8	8
(0,3,2)	98	81	52	29	27	32	25	20	16	16	12	12	11	16	11	10	9	10	5
(0,4,1)	28	21	21	19	23	21	16	15	13	16	17	15	13	13	11	12	13	12	12
(0,4,3)	202	111	56	45	25	21	18	19	17	12	12	12	12	10	9	9	9	7	6
(1,1,1)	35	28	24	26	12	8	8	11	8	11	8	7	7	6	6	7	7	7	7
(0,5,1)	115	67	31	32	25	19	20	17	14	16	18	18	18	21	18	15	12	14	13
(0,6,1)	61	39	30	36	33	27	27	33	20	21	21	23	22	20	23	18	22	20	17
(1,3,2)	26	17	14	13	11	7	7	7	6	6	5	7	6	5	7	6	6	6	5
(1,4,1)	83	16	16	15	16	17	14	15	16	17	15	19	19	16	20	15	13	14	12
(2,2,1)	31	23	16	16	12	21	12	8	9	11	12	9	7	5	7	5	6	9	8
(1,5,1)	34	36	40	39	30	32	18	18	15	18	18	13	10	15	18	12	14	13	7
(2,3,1)	21	22	21	17	22	15	13	16	12	11	10	12	10	11	12	9	15	9	13
(2,3,2)	26	23	15	10	19	11	13	11	8	6	6	7	5	6	5	7	7	7	6

Table 8.4: Fraction of measurement that the error radius represents, as a percent. Often the uncertainty is small relative to the absolute shift that includes the shift induced by the rotating frame, but much larger relative to the residual shift. Table layout same as in table 8.2.

8.4 Inversions for Rotation

8.4.1 Constrained Optimization Inversions

The ability to predict the acoustic data with the previously described basis, cylindrically radial cubic B-Splines and Neumann modes, is shown in figure 8.6, where average misfit is the average misfit is defined as the difference between the prediction from the inversion and observed value, denominated in the error radius. The error radius reflects both possible variability due to flow, as well as decreased confidence associated with measurements described earlier throughout this chapter.

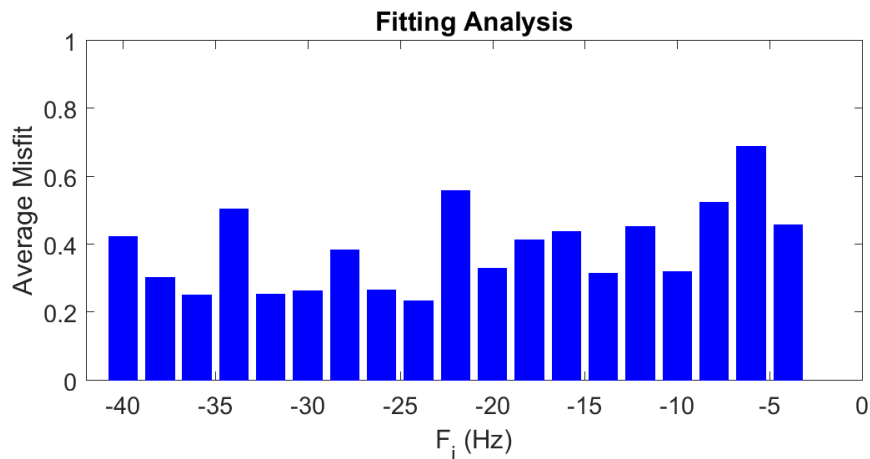


Figure 8.6: RMS misfit of the ratio of the discrepancy between predicted frequencies from inversions and the measured values of frequencies to the error weights. The rotation rate of the outer sphere was 6 Hz, and the inner sphere's rotation rates were -4,-6,...,-40 Hz and shown in the horizontal axis. For the purposes of assessing overfitting vs. underfitting the data, the vertical axis values should be scaled by a factor of between 2 and 4 for converting to uncertainty on the mean. Any choice of a particular value for scaling would be somewhat arbitrary.

One particularly useful idea, is that often velocimetry is a means to an end. It is not actually the velocity at any one particular point that is of critical importance, it is that the velocity field can be used to compute quantities that inform one about related phenomena. In that regard, many issues of finer scale features in inversions do not contribute substantially to variation in those quantities. So, to first motivate discussion of the reconstructed profiles for different Rossby numbers, first I will discuss many functionals that can be defined on the recovered profiles, since they are highly informative and partially motivate interpretations of the inversions.

Functionals defined on the inversions were most revealing, such as total azimuthal angular momentum, average azimuthal velocity, average angular velocity, and for ω_{effect} . Finer details of the reconstructions can often be difficult to interpret the veracity of, especially for high Rossby numbers, but they typically occur in regions that do not produce pronounced affects on the global characteristic features evaluated by functionals defined on the profiles.

Consider the notation

$$\%X_6 := 100 \cdot \frac{\int_V X dV}{\int_V X_6^{sbr} dV} \quad (8.3)$$

where X_6^{sbr} means the quantity evaluated when the fluid is rotating uniformly at 6 Hz with the outer shell, in “solid body rotation”.

The inferred azimuthal angular momentum decreases with the square of the Rossby number, as the fluid is slowed down relative to the outer shell by the inner sphere, eventually rotating in the opposite direction. The fit is depicted in figure ?? along with the data and variation in the values found by using an ensemble of 500 inversions for each Rossby number. Each inversion is performed by choosing values in the uncertainty radius of the measured data, and then inverting with uniform and small error radii to create the weights in the optimization data misfit functions. The ensemble produced can yield a posterior estimate of a functional $\Phi(m)$ defined on the model space, by computing statistics on $\{\Phi(m) : m = Inverse(d_j), j = 1, \dots, N\}$. This is necessary since iterative methods with penalty functions cannot have their posterior error distributions formed by convolution of distribution functions, as is the case for a linear inverse operators. Using the ensemble approach, variations due to data uncertainty were thus able to be incorporate to weighting the

data.

To determine how large of an ensemble was required, several tests were performed using 5000 inversions sampling the error distributions. See figure 8.7 for an example. Though 500 samples did not produce as smooth a distribution, the mean and standard deviation converged sufficiently by 500 samples, and to the same values as the larger sample size, that more samples were not warranted given the accuracy being employed. Profiles using 30,000 or more were also visually inspected in earlier work and found to behave similarly.

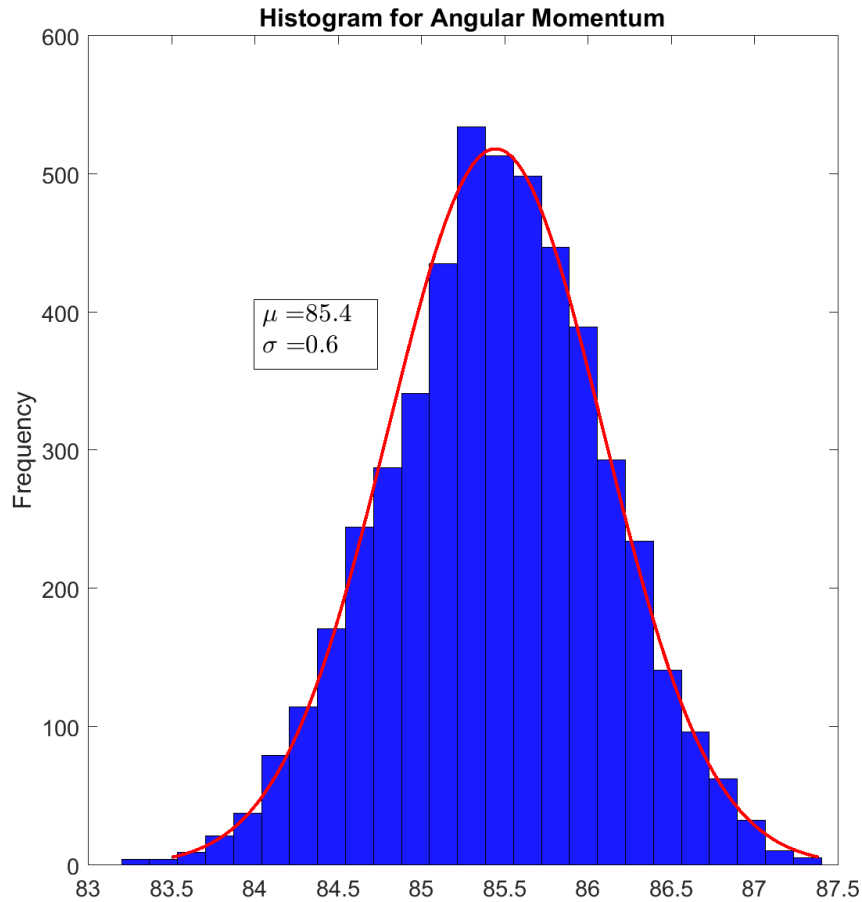


Figure 8.7: Histogram with Gaussian fit for an ensemble of 5000 inversions for $Ro=-4.67$, for the angular momentum quantity described in figure 8.8. The distribution was sufficiently Gaussian and similar in standard deviation and mean for smaller ensembles that it allowed for sufficient accuracy in the weighting of the data when performing fits.

For net azimuthal angular expressed by $\%L_6$ the relationship is

$$\%L_6 \approx 100 - \frac{\pi}{5}Ro^2 \quad (8.4)$$

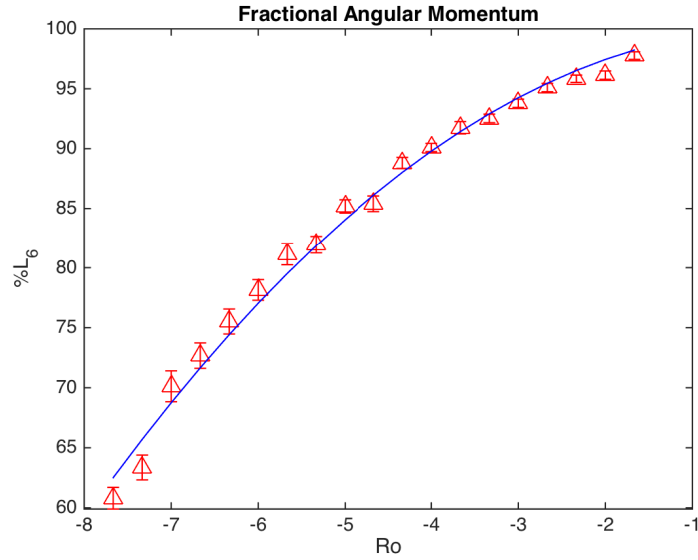


Figure 8.8: The azimuthal angular momentum as a percent of the uniform rotation case at 6Hz, depicted by triangles. The variation with respect to sampling the data within the uncertainty interval around presented as error bars, and the curve depicting a purely quadratic relationship with Rossby number after offsetting by 100% at uniform rotation, i.e. $Ro=0$. The coefficient in the quadratic term is ≈ -0.62

The most interesting aspect of the recovered parameter trends in this section, such as that shown in figure 8.8, is how well they can be fit by simple functions such as a pure quadratic, a square root, or a line. In most cases, they intercept intuitive values of the parameter at $Ro=0$. Also, in the majority of cases, the simple functional forms fit well enough that the values can be used to invert for the Rossby number if the Rossby number is unknown. This is really significant, since even if the predicted flows turned out to be inaccurate, or the functionals were not gauging the quantity they were designed for, the simple relationship between acoustics and the Rossby number contained in these functions gives the ability to infer the Rossby number directly from the acoustics. Preliminary analysis has revealed that even smaller basis function sets with less resolving power and fewer modes in the data set, also fit these profiles. Though those less accurate inversions imply values of the functionals that scatter around the fitting curves more, the fitting parameters are still inferred to within a few percent. However, the analysis has also revealed that the primary contribution to many of these profiles comes from outside the tangent cylinder. That is, the relationships may not be representative of flows inside the tangent cylinder.

The average velocity can be expressed similarly:

$$\%V_6 = 100 + 1.77 \cdot Ro - 0.54 \cdot Ro^2 \quad (8.5)$$

The fit is depicted in figure 8.9. A line could also be used for a portion of the data, but it wouldn't predict the value of 100% at $Ro=0$, nor fit the data as tightly over a broad region as in figure 8.9. The quadratic term in Ro was essential for fitting the profile globally and assuming the value of 100% at $Ro=0$.

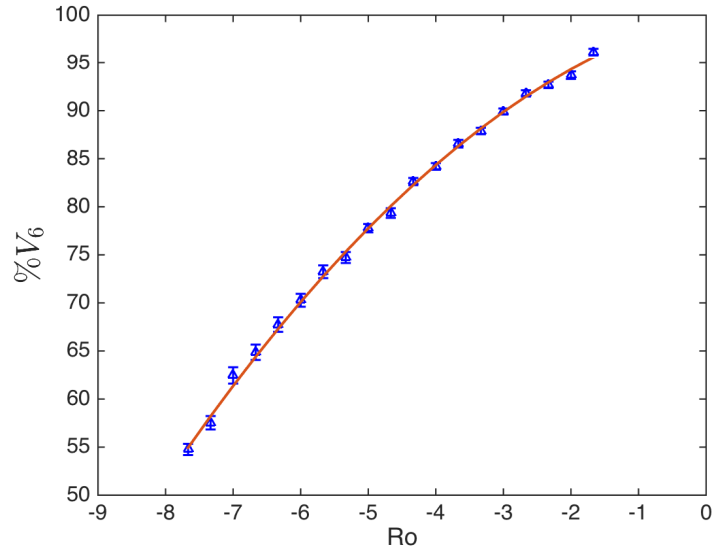


Figure 8.9: The fit of $\%V_6$ is a second order polynomial in Ro with an intercept of 100% at $Ro=0$.

The average rotation rate as a percent of the rotation rate associated with uniform rotation, is somewhat interesting as well. It yielded the following relation quite tightly fit by the equation

$$\% \Omega_6 = 105.4 + 7.66 \cdot Ro \quad (8.6)$$

and the fit is depicted in figure 8.10.

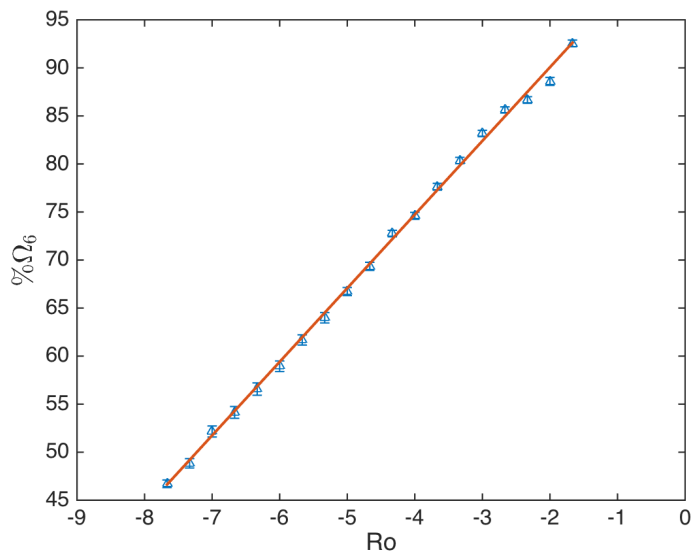


Figure 8.10: The fit of $\%\Omega_6$ is linear but does not go through the 100% at $Ro=0$.

These fits are tight as can be seen in figure 8.8, figure 8.9, and figure 8.10. They are perhaps far more accurate than than any specific location in the cavity reconstructed from an inversion. Especially since one of the most difficult places to resolve the flow well from inversions is inside the tangent cylinder, but a volume integral is biased toward values of r that are larger than they are inside the tangent cylinder. With the exception of the last two data points, it could be possible that the majority of the variation about the fitting curves is due to variations inside the tangent cylinder, or the affects on the flow of the shaft and other non-ideal aspects of the cavity geometry; it also possible though that since the flows are not purely azimuthal and there is turbulence, there is conversion occurring that is causing slight deviations. Since these are not high resolution inversions though, it could also be a case of lack of well resolved features in the azimuthal component. Decomposing into an inside and outside of the tangent cylinder, the outside was still linear whereas the inside did not have a simple trend, when evaluating the same quantity

in the figure 8.10.

The most interesting functional is perhaps the $\% \Omega_6$ profile. It does not go through 100% at $Ro=0$. Trying to force the fit to do so, drastically reduces the accuracy of it's prediction of the data. The deviations from linearity in the $\%L_6$ and $\%V_6$ profiles already imply that the flow is not scaling with Rossby number, after removing the offset due to the rotating frame of reference.

For net ω_{effect} increases as the inner sphere spins faster in the opposite direction of the outer sphere. The non-squared average can also be fit by a simple linear model in Rossby that goes through $Ro=0$, but the fit is not as tight for higher magnitude rossby numbers. This is because as the flow became substantial at higher values of r , the inversions produced what looks like artifacts of the low resolution basis within the tangent cylinder, and even slightly beyond (see figure 8.14). This is because to fit the rotational profile accurately where it affects the acoustics more so, does so at the expense of creating artifacts where the acoustic modes are less sensitive. The side lobes and non local effects in the smaller values of r regions affects the ω more so since it contains gradients in r of the rotation profile. In figure 8.11 what can be seen is a somewhat linear trend through 0 at $Ro=0$, yet by $Ro=5$ there starts to become not only deviations from the trend, but also larger variations seen across the ensembles of solutions.

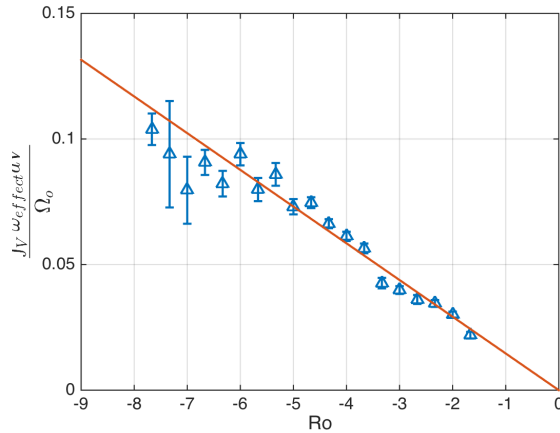


Figure 8.11: Inferred ω_{effect} , described in chapter 1, as a function of Ro .

Figure 8.11 shows the ω_{effect} as having slope ≈ -0.7 trend with Rossby, once normalized by the outer rotation rate; the actual value of the trend is likely slightly higher, since the higher Rossby value data should perhaps not be included in the fit. The normalization could also include a volume factor, to help nondimensionalize the quantity. The volume is just over 0.1 cubic meters, and so the slope is between -6 and -7 once nondimensionalized. Since there is presumably zero ω effect for uniform rotation, the normalization cannot be performed as in previous quantities.

Other complications are that if the shaft is actually slowing down the rotation rate near it, it would cause gradients that actually decreased the net ω effect. For that reason and others, of all the quantities examined, the ω effect is probably the least accurate, since it is corrupted more so by the tangent cylinder interior's fluid rotation and the gradients of that rotation with respect to r ; the inversions are likely to be less accurate there than average over the volume of the cavity.

By using a steep sigmoid function, approximating an infinite shearing of the fluid at a particular value of r , parametrized so that it was negative near the shaft and zero on the other side of the shear zone at higher values of r , constrained optimization over A and r_c was performed to fit the most likely location for the shear zone.

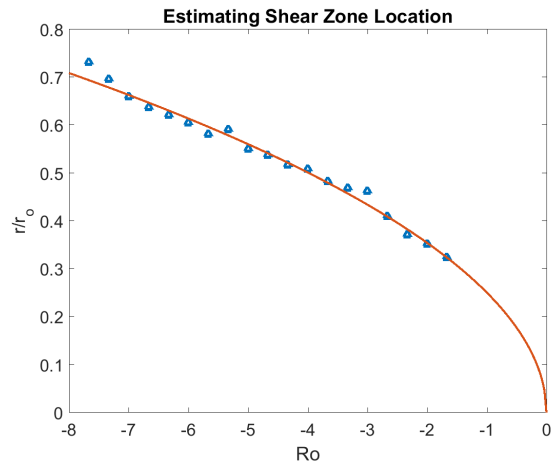


Figure 8.12: Estimating the location of high shear. The horizontal axis represents the location of the vertical line separating the two piecewise constant basis functions, as inferred by minimizing the misfit to the acoustic data; described in text. Though a line is also possible to fit the data nearly as well, the square root function looked like a better fit and also goes through zero, which is consistent with solid body rotation of the fluid. The vertical axis has been non-dimensionalized by dividing by the radius of the outer sphere.

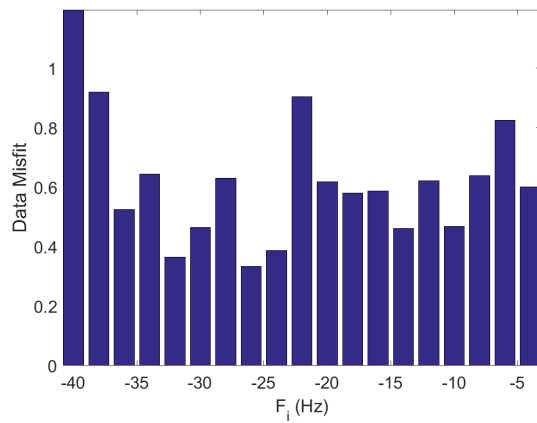


Figure 8.13: Data misfit for the shear zone parametrization by a sigmoid, using similar layout as figure 8.6. This corresponds to the data plotted in figure 8.13.

The profile suggested by figure 8.13 was chosen to be a square root function of the magnitude of Ro . The fit for a line is also convincing, but not only does the square root fit better, but it also goes through 0 at $Ro=0$. Perhaps it should go through the axle radius or shaft radius at $Ro=0$ but 0 was an approximately valid location for the origin, where the fluid is rotating uniformly and has no shear.

This is also in agreement with the previous figures in this section that used the higher resolution basis, since it is showing the affect on the flow profile in the rotating frame is not a simple scaling with the inner sphere rotation rate or Rossby number. Unlike the case of the inner sphere spinning only, the Coriolis force seems to be preventing the shear zone from diffusing out and the angular momentum from mixing as much.

Other features present, include the rotation of fluid following the shaft somewhat near it, rather than the inner sphere. This could be to some extent due to the lack of resolution near the shaft, which was investigated with synthetics and found that there is occasionally drops in the rotation rate near the shaft not due to actual reduction in the input profile. On occasion the drop is more considerable though, and it is possible that the large surface area of the shaft spinning with the outer sphere is reducing the rotation rate as well.

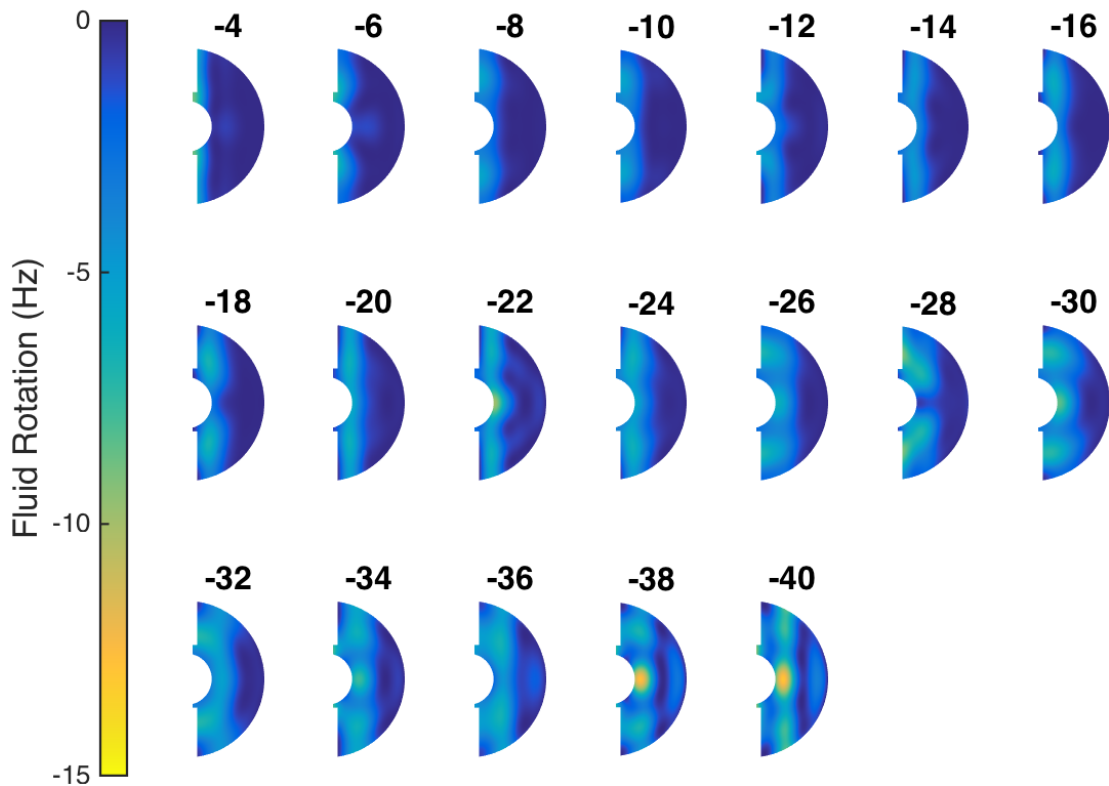


Figure 8.14: Reconstructed inversions at each rotation rate. The rotation rate of the inner sphere has been placed on top of each profile, but all other labelling has been omitted to reduce clutter. The outer sphere is spinning at 6 Hz.

Broadly speaking, what the inversions reveal is that as the Rossby number increases as a shear zone moves out from the tangent cylinder towards the outer sphere's equator.

In figure 8.15 there appears to be a jet instability forming on the inner sphere's equator. The rotation rate appears to be less negative in the regions of the column immediately above and below it than at higher $|z|$ values. It was thought that perhaps this was an affect of the sidelobes of the feature forming at more distant portions of the cavity, but the variation in the column was also recovered, and more pronounced using 2D cubic splines. It seems that the undulations in the profile at higher values of r may actually be the artifact, related to the jet feature.

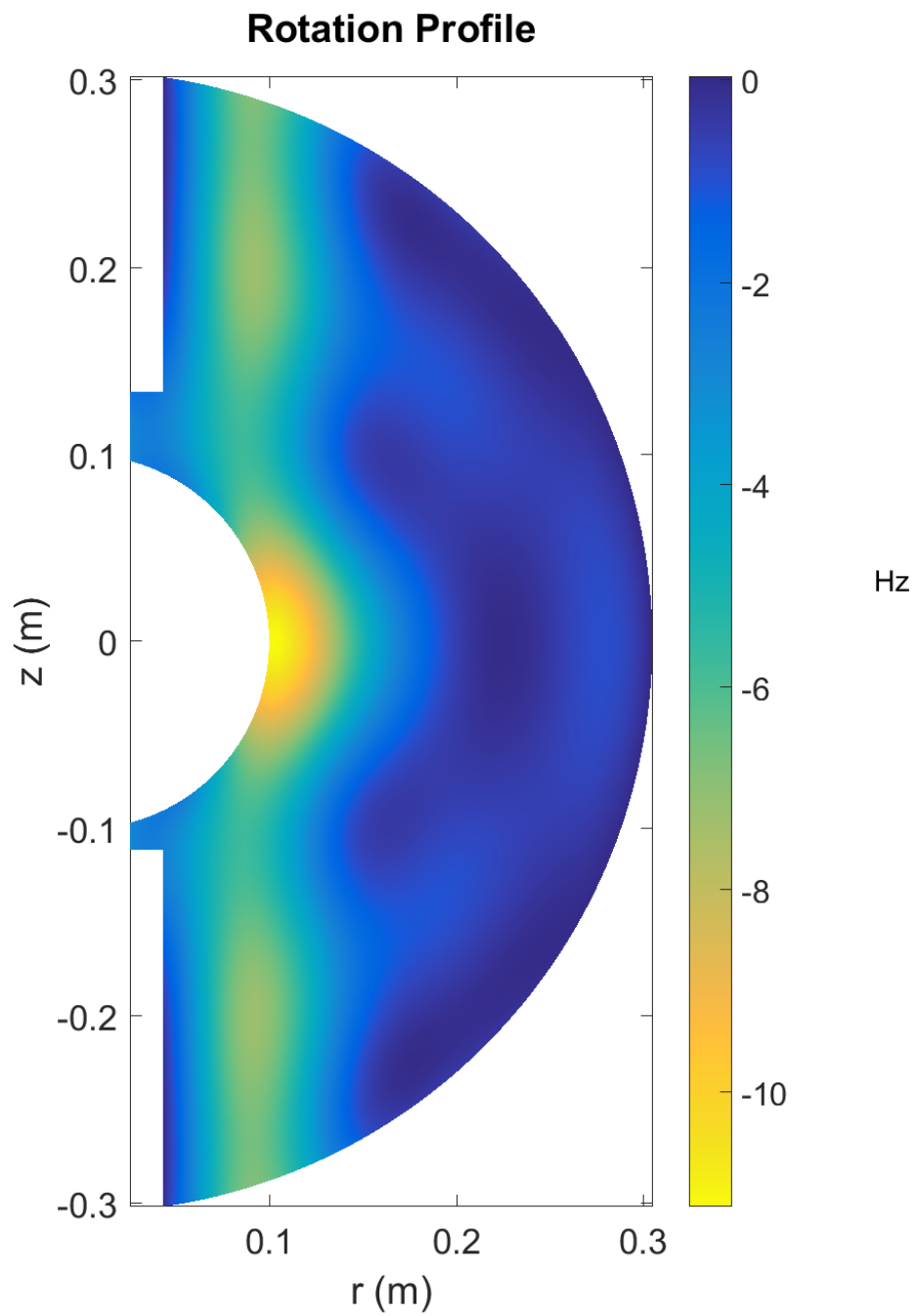


Figure 8.15: Reconstructed flow profile for $Ro = -4.67$, i.e. $F_i = -22$ Hz and $F_o = 6$ Hz. There appears to be a jet forming on the equator of the inner sphere.

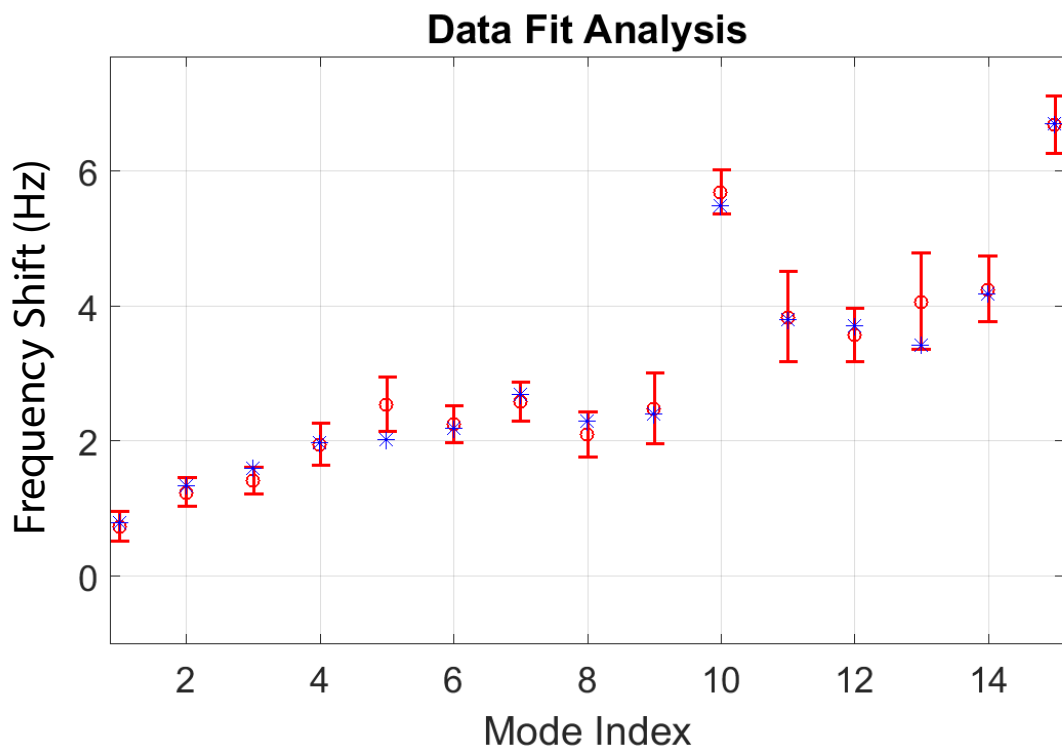


Figure 8.16: Data prediction from reconstructed flow profile for $Ro = -4.67$, i.e. $F_i = -22$ Hz and $F_o = 6$ Hz. The data is plotted in red with the error weights used in the inversion.

Tools of assessment for these types of inversion included assessing variability across ensembles, as done for the functions. In figure 8.17 the relative variation

The jet is likely always present, but perhaps less substantial at other rotation rates. It is difficult to judge the actual size with a low resolution basis. One possible reason for it's emergence, is that as can be seen, a large portion of the fluid is coming to be approximately at rest in the lab frame. The jet is likely much faster in the negative direction, yet the defocussing smears that velocity feature over a larger volume of fluid in the Reconstruction.

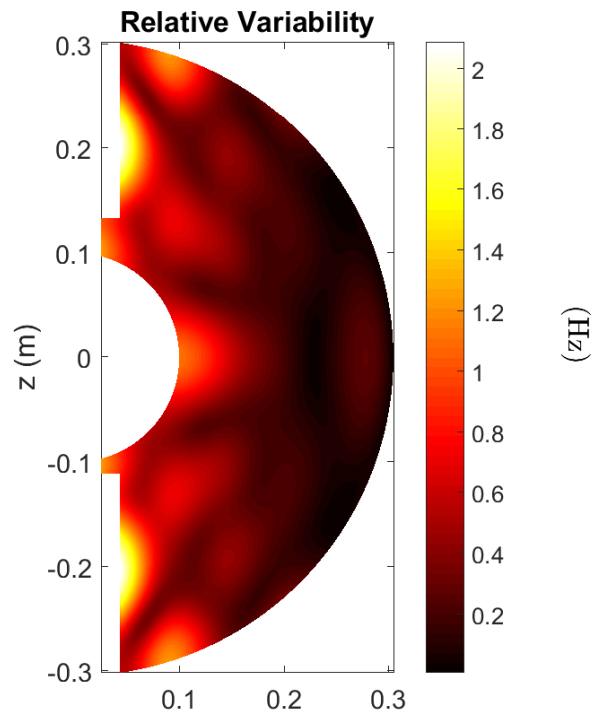


Figure 8.17: Relative variability profile for $Ro=-4.67$, i.e. $F_i = -22$ Hz and $F_o = 6$ Hz. The units of Hz is consistent with the mean flow error radius. This is only variation across an ensemble though, not necessarily reflective of the uncertainties related to how well the basis can match the flow in very localized regions.

Figure 8.18 shows the profile prior to the formation of that feature, when the outer was spinning only -20 Hz. The data misfit is nearly identical, except mode index 5 was slightly better fit than for $F_i = -20$ Hz, but investigation found that not be what is causing the jet like appearance in figure 8.15.

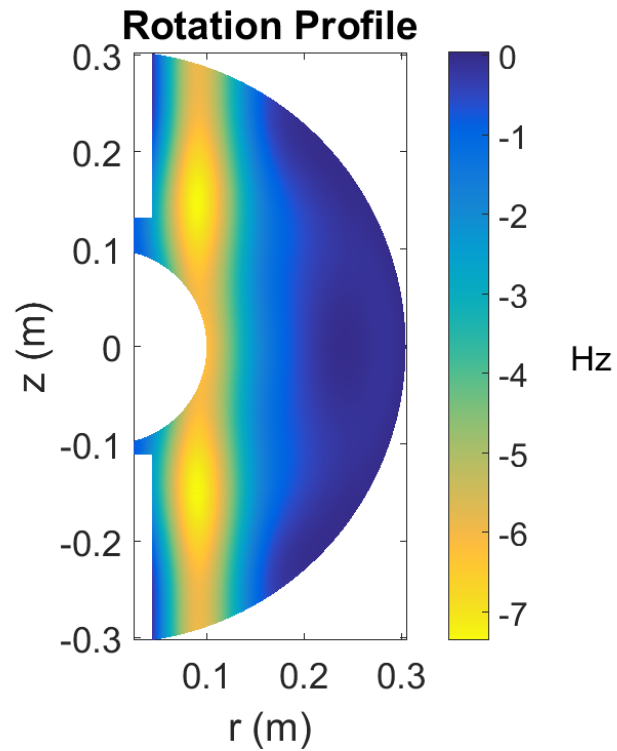


Figure 8.18: Reconstructed flow profile for $Ro=-4.33$, i.e. $F_i = -20$ Hz and $F_o = 6$ Hz. Any jet is less pronounced in this inversion than in the one for $F_i = -22$ Hz.

Beyond these regimes, i.e. beyond $Ro=5$, the profiles start developing vertical variations that are difficult to explain, at least at lower values of r . It could be related to fluid coming to rest in the lab frame, the shaft, other factors left out of the formulation, or simply that fitting the profiles well where the acoustic modes are sensitive trades-off errors at smaller r values in a very disproportionate way.

The last two rotation rates, $F_i = -38$ Hz and $F_i = -40$ Hz seem to be outliers in many analyses such as total azimuthal angular momentum. Several possibilities seem likely. First of all, there are electronics at 45 degrees θ and 135 degrees θ colatitude at several azimuths, and the fluid appears to be following the outer shell; the electronics seem too small in volume for a column to cause that though. It seems to always be present possibly, yet it is not until the fluid begins sub rotating the outer sphere beyond the column that it is noticeable.

Another strong possibility, is that the bound of not super-rotating the outer has a different affect on the inversion once the most of the fluid inside is no longer following the outer shell. Also,, using fewer basis functions so that a traditional weighted least squares inversion could be performed, recovered a rotation rate there that was super-rotating the outer shell. It could actually be the constraint causing the issue. It could be possible that simply the specific angular momentum is non decreasing with r and not velocity necessarily, similar to a conical pendulum speeding up as the level length is decreased; analogous to fluid falling to a shorter r radius.

8.4.2 Consistency with Alternate Basis Functions

To gauge that features observed in the inversions are not artifacts of the basis chosen, alternate basis functions were used, as discussed in the previous section. For instance, the jet-like feature that appears when the inner sphere is rotating at -22 Hz is also recovered by 2D cubic splines, and also by a coarse tiling by Voronoi cells. Since such basis functions are less prone to nonlocal effects that does not stem from the data itself, there is confidence that these features are not artifacts of the parametrization. The concentration of negative rotation in the top and bottom hemispheres also appears in those alternate parametrizations.

Fitting the Voronoi cells iteratively using Quasi-newton methods, and monitoring the inversion, was informative. The jet appears early on, even by the time that the misfit RMS is roughly 1 error weight. That indicates that it is a feature robust across the variations of flow occurring. By roughly an RMS misfit of 0.6 the stationary region is apparent, and only by the time the misfit reaches 0.5 or 0.4 does the stationary region begin to become more varying and lobes present in the hemispheres. Likewise, the rotation rate matching the shaft near the shaft also only occurs as the misfit decreases similarly.

Polynomials in (r,z) also recover similar features as the basis used in the last section, but also produce many artifacts analogous to Runge phenomena, and also oscillate wildly where there is poor coverage of the domain with the sensitivity kernels of the acoustic modes.

A very minimal basis was used, approximating the flow as being vertically invariant and only using 4 splines from the primary basis used in the previous section. Leaving out the 2 splines concentrated at the highest values of r . So, the basis tapers to zero at r_o . The profiles are shown in figure 8.20 and the fitting analysis is shown in figure 8.19. The poor fit of the data for the 2 highest Rossby numbers is due to the constraints possibly. Weighted least squares formulations with smaller basis functions that made no requirements on flow rotation bounds, fit those profiles well but using values of rotation that super rotated the outer sphere. Another large misfit occurs at $F_i = -22$ Hz, which is to be expected since the 2D basis revealed a jet like feature that cannot be expressed in a vertically invariant basis well. The large misfit at $F_i = -6$ could be due the fact that the splittings are small there; such is the case for $F_i = -4$ Hz as well, but it is perhaps compensated by the error bars being much larger as well, since there was at times issues of polarity of the splitting being difficult to determine.

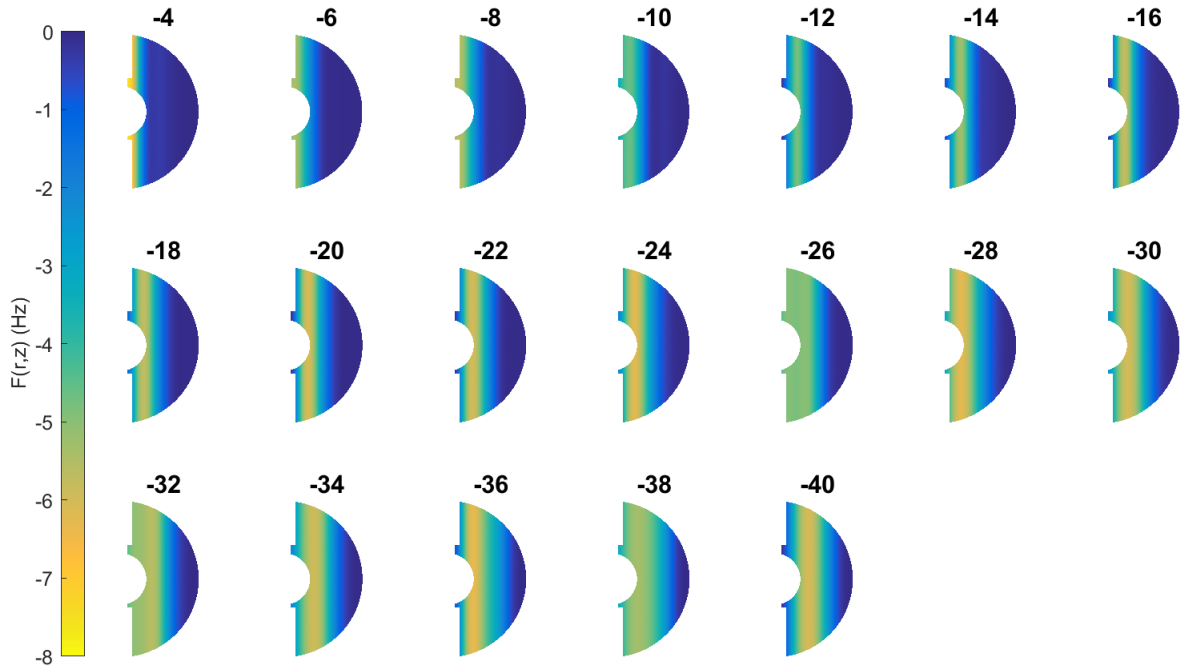


Figure 8.19: Reconstructed Profiles using only 4 cubic splines, as discussed in text. Recovered profiles look similar to how the profiles in figure 8.14 would look if they were averaged vertically and homogenized in the z variable based on that average. Figure similar labelling convention as figure 8.14.

That figure 8.19 suggests that the vertically invariant basis produces inversions similar to vertically averaging 2D reconstructions is reassuring. Often in inversions, projection operators and averaging operators do not commute well with the resolution matrix, meaning that basis that is a subset of larger basis that can express the flow well, will not necessarily recover the projection of the flow onto that subset of the basis vectors. Again, the absence of relative rotation along the shaft that begins to appear at $F_i = -12$ Hz, may be tempting to attribute to the fact that the shaft spins with the outer sphere, but resolution tests have shown it is also at least spatially due to how defocussing of shear zones trades off with the error in flow along the shaft.

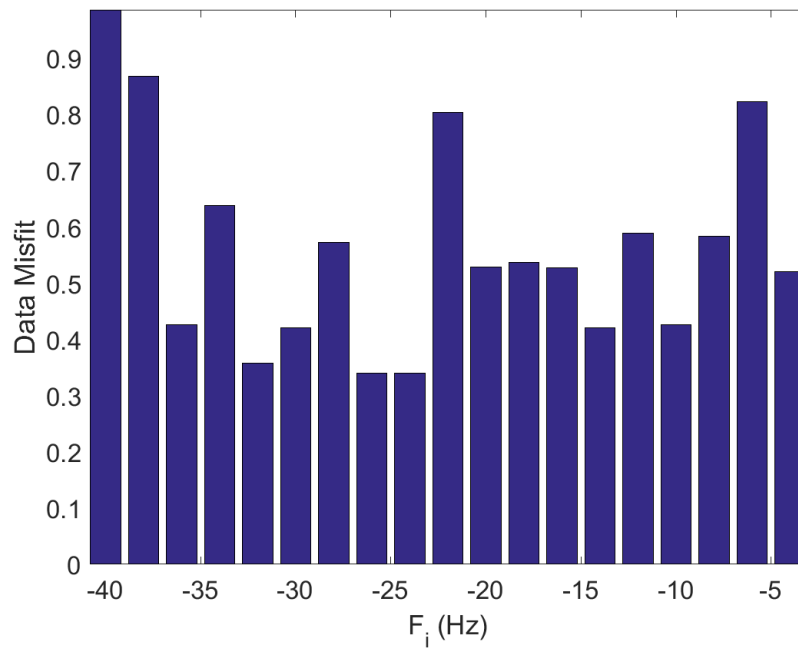


Figure 8.20: Data misfit analysis for basis consisting of 4 cubic splines, discussed in text. Figure similar to figure 8.6.

Figure 8.20 suggests, is that the shear location selected by the sigmoid basis, is not necessarily the region of highest shear, but the region of shear nearest the portion of the cavity following the outer sphere.

8.5 Alternate Methods of Inversions

8.5.1 Minimization of Spread Functions

Using 192 2D cubic splines in (r,z) the minimization of Dirichlet spread function approach was performed. Splines, though overlapping their neighbors, were found to produce less artifacts than using disjoint tilings. Curvature damping in 2 variables, in this case r and z , was used to model the problem, and the Dirichlet spread function was minimized to choose the damping coefficient parameters.

Dirichlet Spread Function Minimization
Inner Rotation Rate of - 22 Hz

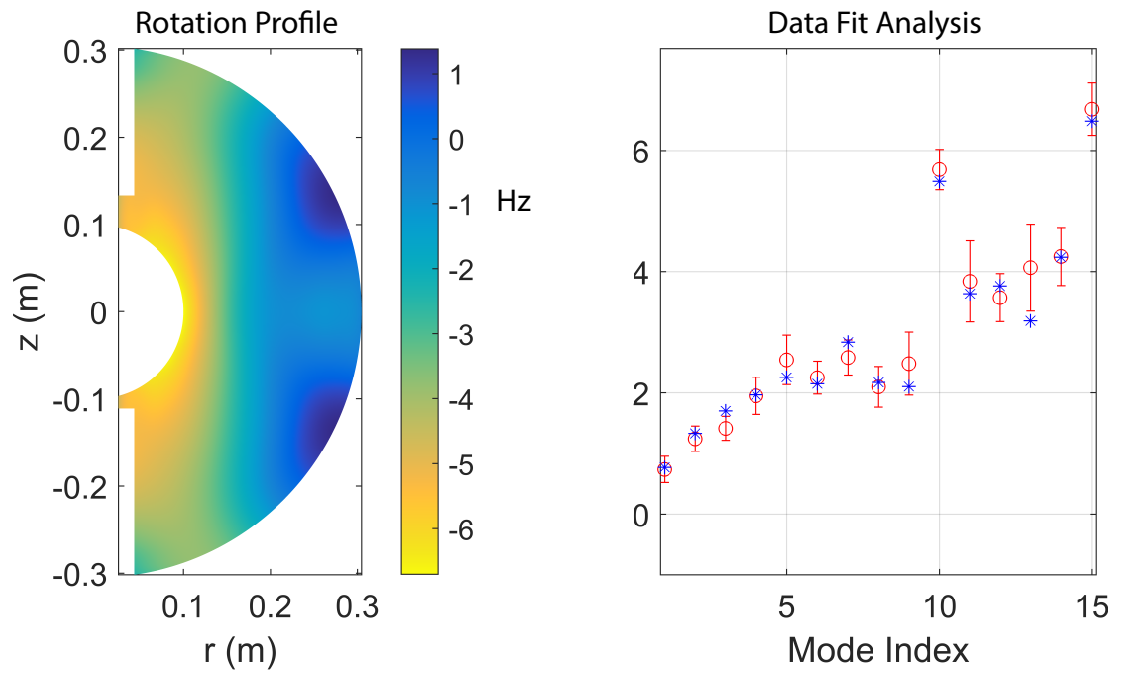


Figure 8.21: Result of minimizing Dirichlet spread function for 2D cubic spline basis. It has many realistic features, but also has some overshoot in the sense that it super-rotates the outer shell in a way that does not seem plausible.

Figure 8.21 has many plausible features and likely is capturing true aspect of the flow. The overshoot artifacts are unfortunate, since they do not appear of a form that physically plausible. Their location looks similar to early iterations of iterative methods that used Quasi-newton methods, suggesting they may a mutual region of sensitivity for two or several modes. It was not investigated further though, since these results proved difficult replicate with different weighting functions, bounds set on the damping parameters, and weighting of the spread function. The trade-offs were also apparent. For instance, at an inner rotation rate of 20 Hz it did show there was less flow at the inner sphere equator, which is consistent with the other inversions, but also showed elevated rotation on the top and bottom of the inner sphere, yet less overshoot in the regions super-rotating the outer shell. It would seem that the variation in the figures could be as easily attributed to how much it is trading off with other parts of the cavity. It would be hard to draw anything conclusive from the inversions. Even though a jet is not only possible but likely, if there are nonphysical artifacts in the inversion, it is not wise to selectively choose which features to lend credence to and which to ignore without good reason.

All issues of parameter choices aside, even profiles such as in figure 8.21 did a remarkably good job at recovering that the flow is closely following the outer sphere, and the spread minimization formulation did not even impose an upper bound on the rotation rate of the fluid in the inversion.

Combining the constraint that the solution must be non-positive did not improve the plausibility, or lift the subjectivity; either by imposing condition for the inverse operator when choosing damping parameters, or by choosing damping parameters and then imposing the restriction by solving the inverse problem constrained.

The Backus and Gilbert approach had even more issues of subjectivity. Unlike the Dirichlet spread function, the weighting of the spread function was much more important. Constraining the rows to sum to 1 of the resolution matrix was not ever close to being obtained, and weighting differently whether by volume or angular momentum did not seem to make much difference. Also, using disjoint tiles instead of splines, in the (R, θ) plane or the (r, z) plane always had issues at

the boundary, since neither could match the boundary everywhere. The splines could have their second derivatives evaluated by interpolating their gradients at the triangle centers back to the nodes and then differentiating at the triangle centers again. Dealing with the fractional areas at the border of the domain did not seem to have any issues with the splines, yet for tiles it would often produce zero as the solution near the boundary even when weighted in many different ways to make up for the fact that the area or volume contribution was different. The same issues were found for both curvature damping in r and z , as for R and θ , using tilings. The use of these methods was a constant search for parameter combinations that yielded plausible results, and so at best seem like confirmation bias. At least theoretically, these methods are very appealing, and would no doubt perform quite well with sufficient data. They also allow for the rapid propagation of uncertainties via convolution of the distribution functions associated with the uncertainties on the measurements; though given the types of errors, it is not completely clear if a standard probability interpretation of the posterior distribution for the rotational profile is fully logical.

Lastly, judging a minimizer by a convergence of the optimization method, here again using interior point method, often produced multiple minimizers depending on the initial conditions, i.e. the damping parameters the iterates started at, though typically only one solution was plausible, or not at the boundary of the constraints. The other would have many localized lobes or be almost completely flat and not fit the data at all when used for inversions.

8.5.2 Interpolating on a Fixed Grid

The domain can be decomposed via constrained Delaunay triangulation, and the flow can be reconstructed by interpolating on the nodal values. Instead of using a forward operator, the kernels are used directly to predict the acoustic effects, and values at the nodes can be determined by traditional optimization methods, such as Broyden-Fletcher-Shannon-Goldfarb algorithm. Different methods of interpolation are possible. The simplest is the nearest neighbor, which tessellates the meridional cross section into Voronoi cells each cell having uniform rotation value. Another simple method is simply linearly interpolates between the nodal values. Finally, natural neighbor

interpolation produces a smooth interpolant except at nodes.

One downside to the slowness of these methods, is it makes propagating uncertainty associated with the data more cumbersome computationally expensive. Furthermore, these inversions were not checked with a plethora of initial conditions to ensure the solution is not a local minimizer of the objective function. However, since alternate means have been presented already that do perform these checks of the answer, when these means produce inversions that are consistent with those alternate means, it increases reliability. When the inversions differ in some feature from method to method, what it can be quite telling. If the data misfit they predict are equally plausible, it says that a feature is not in any way required by the data and it's reliability is low. That may not even be apparent by propagating the data uncertainty, since a single parametrization could have biases not stemming from the data, but from the span of the basis functions possible. When the inversions disagree on some feature, yet have significant differences in how they predict the data accurately, analysis can be very informative. If a single mode's splitting is not predicted well by one, it could allow reassessment of the nature of that data uncertainty or upon examination of the sensitivity kernel determine that the feature in the inversions in question is related to that specific mode splitting that the flows predict differently.

Another aspect of variability is the choice of points to use to define the grid. When using many dozen of points somewhat uniformly sample the domain this type of variation is less pronounced, but small amounts of data discourage using too fine a mesh for the node locations.

8.6 Mean Flow Approximation Issues

Since the flow is varying about the mean flow, even when the mean flow is steady, it means that there are accelerations occurring. The Euler forces associated with $\dot{\Omega}$ is ignored, approximating them as zero in terms of their effect on the low frequency modes used. It is expected that those effects are quite small, and the linear manner in which they add to the force implies they will average out, since the average value must be zero; or at least very small if the flow is close to being steady.

The mean flow is assumed to be steady, which may not always be warranted, especially near a bifurcation value for inner rotation rate. Hysteresis can occur and other forms of oscillations between states, as well as instabilities that obscure what the mean flow represents. Such phenomena are easy to conflate with peak clusters created by the noise envelopes though. The multiple peaks clusters occur around the $m = 0$ modes as well, which strongly suggests noise envelope effects, though it is also possible to some extent the phenomena is due to other forms of coupling such as described in [Roth and Stix \[1999\]](#).

8.7 Alternate Basis Discussion

Polynomials produced nearly identical results, using r and z up to order 5 or greater, but keeping only even orders of z , except would produce far more artifacts such as oscillating at the boundary or regions where sensitivity was low; greater maximum order producing more artifacts. The same features were produced using polynomials by synthetic flows that did not have those oscillations in the flow pattern, which supported the contention that it was just an artifact. Polynomials tend to produce Runge phenomenon that behaves far worse in conjunction with constraints than the basis I used herein. That is, polynomials of low order will prefer to oscillate around the solution, and a large portion of the solution likes to be right on the boundary of the constraint. Relaxing the constraints can remove the problem, but also allows a different type of artifact. The Neumann Modes that have zonal harmonic based factors do not seem to suffer the analogous Gibbs like effect to as marked a degree, though it is because they are supplemented by cubic splines in r . There is one inversion where a pronounced feature forms around where the jet instability is located, which does appear to produce what is likely sidelobe artifacts due to the modal basis components, since it is difficult for the cubic splines to adequately support that high vertical gradient at the equator of the inner sphere.

2D Cubic splines, coupled with their mirror image about $z=0$ to produce a basis functions even about $z=0$, also produced markedly similar effects. That was especially important in the case of the jet like instability that appeared in the rotation rate of $F_i = -22$ Hz with $F_o = 6$ Hz. Since

only even l zonal harmonics were used, all the modal components of the flow basis had lobes in that region. Using least squares projections with synthetics showed that artifacts were never that pronounced as in that inversion, and the fact that the splines recovered it as well showed that it was not an artifact of the basis chosen; it could only be a basis given by the acoustic modes used for data. The cubic splines do not have direct nonlocal effects except at neighboring regions, and so it also lent weight to the idea that there was some artificial sidelobes created by the low order basis having to represent that feature, since they are absent in the spline version. The spline basis did not have the vertically invariant basis components included in their basis, and tended to have slightly more variance in the z direction. While it is possible there is more variation in z direction, since the forward operator was horribly conditioned if the inversion was tried in the traditional manner rather than using constrained optimization, even with as many basis functions as data points, and also the error analysis revealed the regions of higher variation in the z direction were also regions of higher uncertainty, the basis was not preferable. As a diagnostic device for laboratory experiments and assessing if flow changes are occurring concomitantly with magnetic phenomena, I recommend using multiple bases in order to become more fully aware of these aspects. The reason for this commentary, is to convey that a great deal of effort was put into verifying that any feature in the flows was relatively robust to the basis chosen; any bias was due to the limited number of modes available as data. Gauging the effects of coverage issues, synthetics were used to understand what kinds of defocusing were possible. The basis used here was found to perform best and produce the least amount of artifacts across the different differential rotation rates. This is because it has less resolving power perhaps, but the data has little resolving power relative data sets such as those used in helioseismology.

Chapter 9: Concluding Discussion

9.1 Conclusions

9.1.1 Application of the Finite Element Methods

Flow and Acoustics cannot easily be jointly parametrized with a basis that would allow an analytic construction of the forward operator matrix. Even when the modes and frequencies can be well approximated by the spherical annulus approximation, discretization typically must occur in order to calculate the forward operator. An earlier incarnation of my software used the acoustic modes of the actual geometry to parametrize the flow, but found to be suboptimal since the flows of interest tend to exhibit more cylindrical symmetry and variation with r than spherical symmetry or variation easily characterized by variations in θ . A numeric approach must be employed then to perform the inversions, and little is gained by using analytic expressions for the acoustic modes in these contexts. Many methods in helioseismology benefit from those expressions since they allow for asymptotic formulations and more advanced forms of inversions for high frequency modes and amplitude analysis. For these types of laboratory experiments, the finite element method is optimal.

9.1.2 Bulk Fluid Rotation Recovery

The greatest success of the inversions, has perhaps been ignored due to the context of the study: across many different methods and parametrization, the recovery of the bulk fluid rotation was quite robust. This was perhaps less impressive in these experiments, since the fact that the majority of the fluid would follow the outer shell rotation rate was something that could have been

surmised without the inversions.

Optimizing the resolution matrix often produced super rotation artifacts or implausible rotation rates inside the tangent cylinder. However, these undesirable features were only large relative to the flow in the rotating reference frame. They were quite small errors relative to the bulk of the fluid rotating at approximately 6 Hz, and the methods all recovered that the fluid was largely following the outer sphere reasonably well throughout a substantial portion of the cavity. Even the constrained inversions using the primary method used in chapter 8, when the constraints were greatly relaxed, also recovered the overall following of the outer sphere.

The functional that produced simple formulas for their values as a function of Rossby number, allow the Rossby number of the flow to be inferred quite accurately, if that number was not known. It is of little use in an experiment where the fluid has been brought to a relatively steady state and the Rossby number given by the spheres' rotation rate characterizes the flow, but in many other contexts that is a very useful ability to have. It provides a direct way to measure bulk fluid properties from the acoustics, and will work whether the functionals accurately describe the variables they are formulated as or not.

9.2 Looking Forward

9.2.1 Liquid Sodium Experiments

The three meter setup at University of Maryland has pressure probe ports at equally spaced azimuths, and should in theory facilitate identification of modes by azimuthal order m_s by traditional array techniques. There have been multiple difficulties identifying the modes in pressure probe data in the sodium experiments. This engineering aspect of the acoustic velocimetry system will hopefully be resolved in the not too distant future.

9.2.2 Poloidal Flow

If poloidal flow were inducing more shifts than the small ones discussed in chapter 8, it would have corrupted the inference that temperature was causing a uniform shift. The $m_s = 0$ modes

have different sensitivities to poloidal flow, so if the mode frequencies drifted as if by a uniform temperature shift, it seems to suggest that the poloidal flow effects were only causing small drifts, possibly the cause of the clusters of peaks around the mode spectra discussed in chapter 8.

It seems unlikely that temperature and poloidal flow could trade-off in concert so as to create this illusion of the overall drifts being explainable as a uniform temperature shift. More accurate temperature readings could possibly support this better. All evidence indicates an approximately uniform soundspeed to the degree of accuracy needed in this study though.

9.3 Recommendations for Future Improvements

9.3.1 Inversion Formulation

This work developed many of the methods under the assumption of a larger data set. That is still the hope for the data sets once liquid sodium acoustics are functioning properly. However, if only such a meager data set is to be used, there is perhaps greater utility in actually computing the predictions of acoustic splittings without using perturbation theory.

As a test of idea, I coded the acoustic wave equation in the material displacement domain for an infinitely tall Taylor-Couette flow using a FDM. It can also be solved using quadratic eigenvalue problems, but it was simple enough to use an iterative method. I begin by assuming the stationary cavity frequencies, insert them into the convective component of the wave equation in the presence of rotation, solve for the perturbed frequencies, then update the equation and repeat until convergence is attained. This method of successive approximations allows the shifted frequencies to be found without using perturbation theory; though it requires them to be found one at a time since the updated forcing terms are only valid for a single acoustic frequency. Furthermore, the flow can be parametrized in ways other than coefficients of basis functions. The model parameters can be exponents or other parameters, and the inversion can be carried by Quasi-Newton methods or other techniques in nonlinear optimization. It is somewhat more computationally costly though, especially if error propagation is sophisticated.

9.3.2 Poloidal Flow

Using a very targeted chirp with high amplitude, it should be possible to assume frequency fluctuations in the acoustics come primarily from flow or thermal effects. If the thermal effects can be inferred to be uniform from, then the movements of center frequencies can be attributed to Non-azimuthal flow. In the case of liquid sodium, there could be corresponding magnetic phenomena associated with poloidal type flows. The kernels associated with them can be easily computed from the convective operator applied to the acoustic perturbation.

9.3.3 Modeling Geometry

The missing pieces of the shaft seemed to be of less importance, and actually a source of nuisance. They affected the frequencies predicted negligibly, and instead of preventing corruption to the flow, possibly increased it.

There was also an apparent artifact that appeared near the corner of the shaft inside the missing piece in the upper hemisphere in a few of the sensitivity kernels. This could be possibly due to Neumann condition being somewhat poorly defined at a corner, since at a corner the normal derivative is singular technically. This artifact did not appear in the modes, and seemed to be due to computing gradients on the triangular mesh. Different methods were used to compute the gradients to remove the artifact to no avail, and it was present when computing the kernels from modes I computed using the Matlab PDE toolbox as well. It only occurred over a very small portion of area, and was not significantly large in amplitude, so after concluding that zeroing out the sensitivity there and also smoothing the mode or kernel did not produce visible differences in inversions, it was ignored. It is likely due to the fact that despite many modes being nearly zero there, the high stiffness encountered at the corner caused some lack of smoothness. Ultimately though, the region's geometry was highly idealized, and the model's deviation from reality was likely far greater than any numerical aspects such as this, but if I had to do it again I would smooth out all corners, for cosmetic reasons and to prevent having to test the effects of the possible artifact. The issue did not occur in my models of the 30-cm setup or the 3-m setup since they had only an

axle though; it only seemed to occur on corners that protruded into the cavity.

9.3.4 Meshing Geometry

A great deal of exploration with meshing techniques was performed. The methods set forth in [Persson and Strang \[2004\]](#) were by far the best approach. The technique is improved mesh quality and the regularity of the triangles in the mesh outperformed anything I was able to do easily with other available software. The method was also easy to understand, so coding it with the specifications of the particular application did not require much time investment.

Adaptive meshing and nonuniform meshes were also explored, but for solving for modes, the linear algebra was simpler to assess the numerics of when a very regular mesh was used and the matrix entries of the FEM operators had relatively equal magnitudes.

9.3.5 Test Functions and Shape Functions

Using a much finer basis during experimentation with minimizing spread functions and with more complicated constraint equations often involved computing second derivatives. One natural improvement would be to abandon the piecewise linear formulation so that the second derivatives could be computed inside each element, and the shape functions could be used as the basis functions. Gradients can be computed naturally for piecewise linear elements, but second derivative calculations often resembled finite difference computed derivatives as a result of not having curvature in the test functions locally; I used interpolating functions and computed the answer via difference methods. When spline functions or polynomials were used, since the derivatives could be computed analytically then evaluated on the mesh, but the freedom to compute the second derivatives as straightforwardly as the gradients would be helpful when using the shape functions as basis functions.

9.3.6 Inclusion of Magnetic Data in Constraints

Possibly by including magnetic data based inferences the constraints can be improved. The more information about the flow that can supplement the data the better. It is possible electromagnetically to determine the fluid velocity near the outer shell. In the case of liquid sodium, it is also possible to tell how much torque is being required to maintain the rotation of the inner sphere. All such information can be incorporated to augment limited acoustic data, thereby increasing the amount of information the acoustic data can convey. It has also been suggested in [Adams, 2016] that selection rules could be used to suggest the possible flows inside, though not unambiguously. In which case it would only require simply testing the different possibilities using the forward operator for the acoustics. If the different flow states have sufficiently different acoustic signatures, the flow could be inferred without carrying out an explicit inversion.

9.3.7 Adaptive Interpolation

Allowing the grid points to move as well, introduces more flexibility into the inversion. I ran some preliminary tests, and found that the grid points tend to cluster so as to be able to form regions of high shear. Perhaps the method would be ideal to capturing high shear without having to use a very fine set of basis functions.

Bibliography

- Santiago Andrés Triana, Daniel S Zimmerman, Henri-Claude Nataf, Aurélien Thorette, Vedran Lekic, and Daniel P Lathrop. Helioseismology in a bottle: modal acoustic velocimetry. *New Journal of Physics*, 16(11):113005, 2014.
- Daniel P Lathrop and Cary B Forest. Magnetic dynamos in the lab. *Physics Today*, 64(7):40–45, 2011.
- Emmanuel Dormy, Jean-Pierre Valet, and Vincent Courtillot. Numerical models of the geodynamo and observational constraints. *Geochemistry, geophysics, geosystems*, 1(10), 2000.
- Gary A Glatzmaier and Paul H Roberts. A three-dimensional convective dynamo solution with rotating and finitely conducting inner core and mantle. *Physics of the Earth and Planetary Interiors*, 91(1):63–75, 1995.
- Gary A Glatzmaier, Darcy E Ogden, and Thomas L Clune. Modeling the earth’s dynamo. *The State of the Planet: Frontiers and Challenges in Geophysics*, pages 13–24, 2004.
- Ulrich R Christensen, Julien Aubert, and Gauthier Hulot. Conditions for earth-like geodynamo models. *Earth and Planetary Science Letters*, 296(3):487–496, 2010.
- RA Secco. Viscosity of the outer core. *Mineral Physics and Crystallography, A Handbook of Physical Constants*, pages 218–226, 1995.
- Eugene N Parker. Hydromagnetic dynamo models. *The Astrophysical Journal*, 122:293, 1955.
- JB Taylor. The magneto-hydrodynamics of a rotating fluid and the earth’s dynamo problem. In *Proceedings of the Royal Society of London A: Mathematical, Physical and Engineering Sciences*, volume 274, pages 274–283. The Royal Society, 1963.
- Matthew M Adams, Douglas R Stone, Daniel S Zimmerman, and Daniel P Lathrop. Liquid sodium models of the earths core. *Progress in Earth and Planetary Science*, 2(1):1–18, 2015.
- Peter Olson. Laboratory experiments on the dynamics of the core. *Physics of the Earth and Planetary Interiors*, 187(1):1–18, 2011.
- Y Takeda. Development of an ultrasound velocity profile monitor. *Nuclear Engineering and Design*, 126(2):277–284, 1991.
- H-C Nataf, Thierry Alboussiere, Daniel Brito, Philippe Cardin, Nadege Gagniere, Dominique Jault, and Denys Schmitt. Rapidly rotating spherical couette flow in a dipolar magnetic field: an experimental study of the mean axisymmetric flow. *Physics of the Earth and Planetary Interiors*, 170(1):60–72, 2008.
- Daniel R Sisan, Nicolás Mujica, W Andrew Tillotson, Yi-Min Huang, William Dorland, Adil B Hassam, Thomas M Antonsen, and Daniel P Lathrop. Experimental observation and characterization of the magnetorotational instability. *Physical Review Letters*, 93(11):114502, 2004.

- Michael J Thompson, Jørgen Christensen-Dalsgaard, Mark S Miesch, and Juri Toomre. The internal rotation of the sun. *Annual Review of Astronomy and Astrophysics*, 41(1):599–643, 2003.
- Matthew Adams. Magnetic and acoustic investigations of turbulent spherical couette flows. *Dissertation*, 2016.
- Per-Olof Persson and Gilbert Strang. A simple mesh generator in matlab. *SIAM review*, 46(2): 329–345, 2004.
- Yousef Saad. Variations on arnoldi’s method for computing eigenelements of large unsymmetric matrices. *Linear algebra and its applications*, 34:269–295, 1980.
- Richard B Lehoucq, Danny C Sorensen, and Chao Yang. *ARPACK users’ guide: solution of large-scale eigenvalue problems with implicitly restarted Arnoldi methods*, volume 6. Siam, 1998.
- Richard H Byrd, Jean Charles Gilbert, and Jorge Nocedal. A trust region method based on interior point techniques for nonlinear programming. *Mathematical Programming*, 89(1):149–185, 2000.
- Philip E Gill, Walter Murray, Margaret H Wright, et al. *Numerical linear algebra and optimization*, volume 1. Addison-Wesley Redwood City, CA, 1991.
- M Roth and M Stix. Coupling of solar p modes: quasi-degenerate perturbation theory. *Astronomy and Astrophysics*, 351:1133–1138, 1999.